

## INFORMATION TO USERS

This manuscript has been reproduced from the microfilm master. UMI films the text directly from the original or copy submitted. Thus, some thesis and dissertation copies are in typewriter face, while others may be from any type of computer printer.

**The quality of this reproduction is dependent upon the quality of the copy submitted.** Broken or indistinct print, colored or poor quality illustrations and photographs, print bleedthrough, substandard margins, and improper alignment can adversely affect reproduction.

In the unlikely event that the author did not send UMI a complete manuscript and there are missing pages, these will be noted. Also, if unauthorized copyright material had to be removed, a note will indicate the deletion.

Oversize materials (e.g., maps, drawings, charts) are reproduced by sectioning the original, beginning at the upper left-hand corner and continuing from left to right in equal sections with small overlaps. Each original is also photographed in one exposure and is included in reduced form at the back of the book.

Photographs included in the original manuscript have been reproduced xerographically in this copy. Higher quality 6" x 9" black and white photographic prints are available for any photographs or illustrations appearing in this copy for an additional charge. Contact UMI directly to order.

# UMI

A Bell & Howell Information Company  
300 North Zeeb Road, Ann Arbor MI 48106-1346 USA  
313/761-4700 800/521-0600



DEFECT AND DIFFUSION STUDY IN BORON IMPLANTED SILICON

By

JINNING LIU

A THESIS PRESENTED TO THE GRADUATE SCHOOL  
OF THE UNIVERSITY OF FLORIDA IN PARTIAL FULFILLMENT  
OF THE REQUIREMENTS FOR THE DEGREE OF  
DOCTOR OF PHILOSOPHY

UNIVERSITY OF FLORIDA

1996

**UMI Number: 9800152**

---

**UMI Microform 9800152**  
**Copyright 1997, by UMI Company. All rights reserved.**

**This microform edition is protected against unauthorized  
copying under Title 17, United States Code.**

---

**UMI**  
**300 North Zeeb Road**  
**Ann Arbor, MI 48103**

dedicated to my parents

## ACKNOWLEDGMENTS

This dissertation would not have been possible without the guidance and support of my advisor, Dr. Kevin Jones, who not only provides us illuminating advice but also creates a stress-free environment for us to work in and do our best. I would like to thank Drs. Steve Pearton, Cammy Albernathy, Rajiv Singh and Mark Law for serving on my committee, and Dr. Robert Park for sitting in my defense. Special gratitude is due to Dr. Jian Chen, who patiently helped me get into the door when I first joined the group four years ago and gave me many valuable suggestions in the years following. Special gratitude is also due to Dr. Wish Krishnamoorthy for many stimulating discussions and a thorough correction on my dissertation draft. I would like to thank all my colleagues, especially members of our silicon group, Brad Herner and Sushil Bharatan, for many helpful discussions, and my officemate as well as good friend, Ranju Datta, for keeping me company and making my time at school enjoyable.

It would have been impossible to finish this work without the assistance of many other people. Dr. Lenny Rubin at Eaton Corporation and Craig Jasper at Motorola helped me with the implantations. Dr. Jinghong Shi and Joe Bennett from SEMATECH helped me with the SIMS analysis. Dr. Hans

Gossmann kindly provided me with the boron doping superlattices as well as his PROPHET simulation results. Dr. Heemyong Park, Dr. Samir Chaudhry and Omer Dokumaci showed me how to run the simulation program FLOOPS. I thank all of them.

I am especially grateful to Joe and Alisa Zhu, John and Sherry Ding for their long-lasting friendship, which has driven away much of my lonely time and made my stay in Gainesville full of joy.

I am unable to express my gratitude to my parents Zezhan and Yafan and my sister Jinqi for the sacrifice they have made for me to make it so far.

Finally, I would like to thank my husband Jun Zhou for his love and understanding.

## TABLE OF CONTENTS

ACKNOWLEDGMENTS .....	iii
ABSTRACT .....	vii
CHAPTERS	
1 INTRODUCTION .....	1
1.1 Motivation and Objective.....	1
1.2 Background.....	3
1.2.1 Shallow Junctions .....	3
1.2.2 Implant Damage and Types of Extended Defects .....	7
1.2.3 {311} Rod-like Defects .....	10
1.2.4 Dopant Diffusion in Silicon .....	18
1.3 Implantation, Characterization and Simulation Techniques .....	25
1.3.1 Ion Implantation .....	25
1.3.2 Transmission Electron Microscopy .....	27
1.3.3 Secondary Ion Spectroscopy .....	29
1.3.4 Florida Object Oriented Process Simulator .....	30
1.4 Thesis Statement.....	31
2 THE FORMATION THRESHOLD OF {311} DEFECTS AND SUB-AMORPHIZATION DISLOCATION LOOPS.....	33
2.1 Overview.....	33
2.2 Experimental Procedures.....	34
2.3 Defect Microstructure.....	35
2.4 Criteria for the Formation of {311} Defects and Sub-amorphization Loops .....	37
3 EFFECT OF ANNEALING ON DEFECT EVOLUTION AND TRANSIENT ENHANCED DIFFUSION.....	48
3.1 Overview.....	48
3.2 Effect of Annealing on Defect Behavior.....	49
3.2.1 Experimental Procedures .....	49
3.2.2 Defect Evolution: Microstructure, Interstitial Density and the Activation Energy of Interstitial Decay .....	50
3.2.3 Defect Evolution: Density, Size and Size Distribution .....	53
3.3 Effect of Annealing on Transient Enhanced Diffusion .....	58
3.3.1 Experimental Procedures .....	58



3.3.2 Dopant Diffusion during Annealing .....	59
3.3.2.1 Static Peak at High Concentration .....	59
3.3.2.2 Broadened Tail at Low Concentration .....	63
3.3.3 The Activation Energy for the Diffusion Saturation Process .....	65
4 THE INFLUENCE OF IMPLANT ENERGY ON DEFECT BEHAVIOR AND TRANSIENT ENHANCED DIFFUSION.....	86
4.1 Overview.....	86
4.2 Implant Energy Effect on Defect Behavior.....	87
4.2.1 Experimental Procedures .....	87
4.2.2 Defect Microstructure and Dissolution Process .....	87
4.2.3 Defect Density, Size and Size Distribution during Annealing .....	90
4.3 Implant Energy Effect on Transient Enhanced Diffusion .....	93
4.3.1 Experimental Procedures .....	93
4.3.2 Dopant Diffusion Behavior .....	94
4.3.3 Correlation Between Defects and TED .....	96
5 THE INFLUENCE OF IMPLANT DOSE ON DEFECT BEHAVIOR AND TRANSIENT ENHANCED DIFFUSION.....	120
5.1 Overview.....	120
5.2 Implant Dose Effect on Defect Behavior.....	122
5.2.1 Experimental Procedures .....	122
5.2.2 Defect Microstructure and Dissolution Process .....	122
5.2.3 Defect Density, Size and Size Distribution during Annealing .....	126
5.3 Implant Dose Effect on Transient Enhanced Diffusion .....	129
5.3.1 Experimental Procedures .....	129
5.3.2 Dopant Diffusion Behavior .....	130
5.3.3 TED Saturation at Higher Dose .....	132
6 SUMMARY AND FUTURE WORK .....	151
6.1 Summary.....	151
6.2 Future Work.....	158
LIST OF REFERENCES .....	163
BIOGRAPHICAL SKETCH .....	171

Abstract of Dissertation Presented to the Graduate School  
of the University of Florida in Partial Fulfillment of the  
Requirements for the Degree of Doctor of Philosophy

DEFECT AND DIFFUSION STUDY IN BORON IMPLANTED SILICON

By

Jinning Liu

December, 1996

Chairman: Dr. Kevin S. Jones

Major Department: Materials Science and Engineering

The aim of this work is to better understand the nature of transient enhanced diffusion (TED) of boron in silicon.

A matrix of sub-amorphization boron implants was used in this work with energies ranged from 5 to 40 keV and the doses ranged from  $5 \times 10^{13}$  to  $1 \times 10^{15}$  cm<sup>-2</sup>. The formation threshold of {311} rod-like defects and sub-amorphization dislocation loops are higher for lower implant energies. For the same energy, the threshold dose for {311} defect formation is lower than that for loop formation.

The study of annealing condition effect on {311} defect behavior and boron TED shows that {311} defects dissolve more rapidly at higher temperatures. The concentration of interstitials trapped in {311} defects was below the value predicted from previous studies of Si<sup>+</sup> implants, indicating

the presence of submicroscopic boron interstitial complexes. The interstitial emission from {311} defects during anneals shows an exponential time dependence with an activation energy of 3.8 eV. The time constant for TED saturation process is smaller at higher temperatures and the dependence shows an activation energy of 1.6 eV. Both {311} defects and boron interstitial pairs are believed to be the source of interstitials driving TED.

The implant energy effect on {311} defects and TED was also studied. The dissolution of {311} defects is slower for higher energy implants. This may be due to either an increase in the surface recombination or an increase in the ratio of boron interstitial clusters to {311} defects with decreasing energy. Lower diffusion enhancement and shorter duration of TED were observed for the 5 keV implant than for all the higher energies at a dose of  $2 \times 10^{14} \text{ cm}^{-2}$ . The {311} defects might anneal slower than mobile boron interstitial pairs so that the increase in {311} defect concentration may account for the increase in TED duration. Surface recombination is believed to play an important role for the 5 keV implant so that the amount of TED is reduced.

The study of dose effect on defect and TED shows that {311} defects dissolve slower at higher doses. Diffusion increases with increasing dose initially. Boron interstitial clusters and dislocation loops formed at high doses suppress any further increase in TED with increasing dose above  $2 \times 10^{14} \text{ cm}^{-2}$  at 20 keV by acting as interstitial sink.

## CHAPTER 1 INTRODUCTION

### 1.1 Motivation and Objective

Since the development of the first integrated circuits, the minimum feature sizes of devices have been reduced dramatically. This miniaturization is expected to continue and by the year 2000, the number of transistors per chip is expected to reach one billion. The scaling of devices to smaller dimensions both vertically and horizontally implies lower voltages, thinner dielectrics and more abrupt and shallower dopant profiles.<sup>1-3</sup> The new devices will possess the properties of higher packing density, higher speed and lower power consumption.<sup>4,5</sup> However, before the realization of this goal, many challenges remain in processing and packaging. One of them, for example, is to scale the source/drain junction depth and the lateral penetration under the gate in order to maintain a threshold voltage for the MOSFET independent of the channel length.

Among the various methods available for forming shallow junctions,<sup>6-11</sup> ion implantation is currently the most widely used one, due to its precise controllability, uniformity and reproducibility. However, future devices require shallow p<sup>+</sup>/n junctions with depths less than 1000Å to minimize short

channel effects and to maintain low contact resistance.<sup>12</sup> These shallow junctions will be difficult to form by ion implantation. One of the reasons is that the implantation process induces a supersaturation of silicon interstitials, which will eventually lead to anomalous dopant diffusion, known as transient enhanced diffusion (TED).<sup>13-20</sup> TED is caused by the pairing of excess silicon interstitials with dopant atoms which reduces the energy barrier for the migration of dopant atoms through the bulk. As a result, the dopant penetration depth from diffusion is greatly increased. TED lasts for only a limited time at typical annealing temperatures so it is transient in nature.

TED will affect the source/drain dopant profiles both vertically and laterally. The vertical diffusion results in deeper profiles, which will weaken the control of the gate voltage. The lateral diffusion reduces the effective channel length which may result in punch-through phenomenon. Besides these two effects, the enhanced diffusion of channel dopant near the gate edge from excess interstitials created during the lightly doped drain (LDD) or source/drain implant causes an increase in the threshold voltage for shorter gate length devices.<sup>21</sup> This is the so-called reverse short channel effect, i.e., an anomalous increase in the threshold voltage with a decrease in device dimension. As device dimension shrinks further, these effects will become more pronounced.

Thus the objective of this work is to study the effect of implantation induced defects on transient enhanced

diffusion, and to provide an experimental basis for the improvements of process development, process simulators and ion implanters. These improvements would be of paramount importance to optimizing the device structure.

## 1.2 Background

### 1.2.1 Shallow Junctions

A cross section of a complementary metal oxide semiconductor (CMOS) structure is shown in Fig. 1.1. The performance of this device is controlled by the gate electrode, the gate dielectric, the channel and well region and the source/drain junctions.

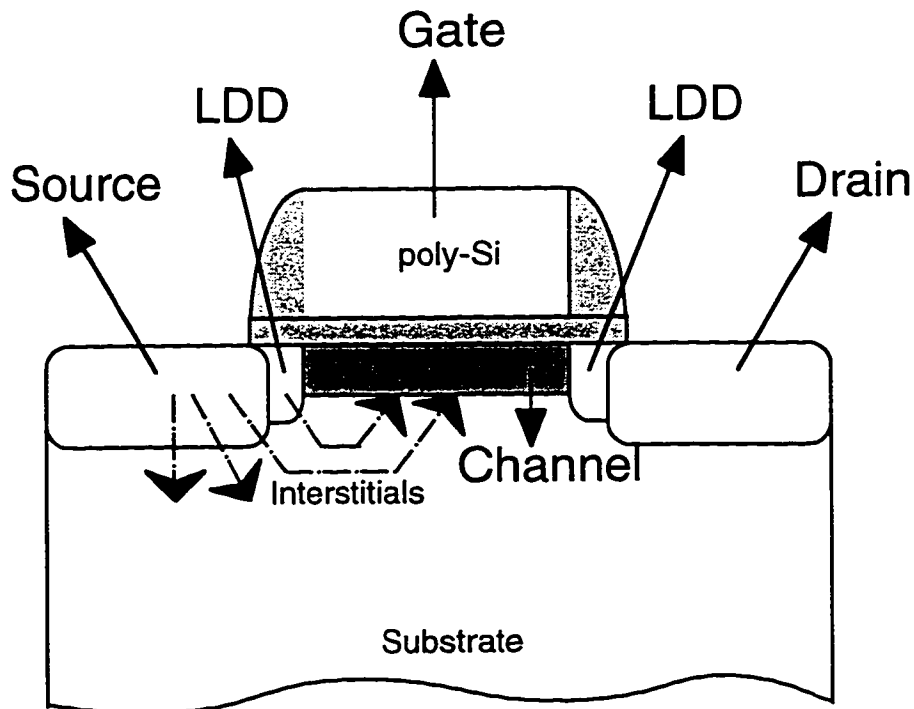


Figure 1.1. Schematic of MOS transistor showing how interstitials are released from source/drain and LDD implants and affect channel voltage.

As mentioned in the previous section, the common trend in the development of solid state devices, either memory or microprocessor, is the decrease in device dimensions. MOS devices with sub-micron dimensions require junction depths of  $0.1\sim0.2\mu\text{m}$ . The most commonly used technique in forming shallow junctions is to implant dopant species at low energies into the silicon substrate.

To form shallow  $p^+/n$  junctions, direct ion implantation typically requires a very low energy boron implant preceded by silicon or germanium amorphization to reduce channeling, or a low energy  $\text{BF}_2^+$  implant which uses the F to amorphize the surface.<sup>22-24</sup> The use of pre-amorphization by  $\text{Si}^+$  or  $\text{Ge}^+$  introduces another implant step. In addition, the amorphization of the surface will introduce end-of-range damage, which may not be annealed out even at high temperatures. This end-of-range damage is a source of interstitials and, if located across the junctions, will result in unacceptably high leakage currents. For the use of  $\text{BF}_2^+$  implants, the fluorine ions can affect the permeability of the gate oxide to boron diffusion. This can cause a penetration problem of boron atoms from the gate region through the gate oxide to the channel region, therefore undesirably affecting the threshold voltage of the device. Thus one would like to avoid  $\text{BF}_2^+$  implantation. One alternative is to simply use low energy  $\text{B}^+$  implants. However, there are several problems associated with  $\text{B}^+$  implants alone.

In addition to the channeling effect of  $B^+$  implantation without pre-amorphization which can significantly increase the junction depth, the post-implantation annealing results in deeper profiles greater than that allowed by intrinsic diffusion due to TED. TED is associated with the interaction of mobile silicon interstitials with boron atoms.<sup>18,25,26</sup> Implants into a pre-amorphized substrate can eliminate channeling tails, but TED is still present. For  $B^+$  implant the amount of TED is determined by both the number of excess interstitials in the damage region and the partitioning of these excess interstitials into different forms such as mobile boron interstitial pairs, boron interstitial clusters, {311} defects and dislocation loops and the role of the surface.<sup>27-29</sup> This implantation induced TED will be discussed in greater detail in section 1.2.4.

Shallow junctions are also formed in combination with silicidation of source and drain. In general the implant and anneal are done before metal deposition and silicide formation. However, the implants could also be performed through a deposited metal layer (Co or Ti mainly) before silicide formation,<sup>30-34</sup> or into an already formed silicide layer that then acts as a diffusion source (SADS) upon subsequent annealing.<sup>35-37</sup> In the first two cases, a silicide layer is formed after annealing with a steep implant profile and a shallow junction. During the silicide formation, a portion of the heavily doped silicon region is consumed and the silicide interface moves into silicon, while dopants



segregate into the silicide.<sup>30</sup> This causes serious contact resistance problems.<sup>31-34</sup> Moreover, silicidation perturbs the point defect concentration in the substrate by injecting vacancies and depleting interstitials,<sup>38,39</sup> which should also be taken into consideration during the process design. In the case of SADS process, the dopant species is implanted entirely into the silicide and then driven into silicon at low temperature. This avoids both dopant channeling and damaging of the silicon. SADS is a very attractive method to form 300~400Å junctions. However, extension implants are still necessary to define the channel length etc. The disadvantages of SADS include uneven doping due to rough interface and dopant precipitates in the silicide.

Thermal diffusion is also used for junction formation. While conventional diffusion does not create damage, it suffers from poor controllability and requires a high thermal budget. An alternative diffusion method is gas-immersion laser doping (GILD).<sup>40</sup> An excimer laser is used to rapidly heat and melt the silicon surface.  $\text{BF}_3$  is then adsorbed, pyrolyzed and diffused into the melt. The junction depth is determined by the melt. A 100Å junction depth has been achieved with this method, which would be attractive if technical, uniformity and cost issues can be resolved.

In summary, there are various ways to form a shallow junction, and each has its own advantages and drawbacks. This study is focused on the use of implantation of  $\text{B}^+$  into

crystalline silicon to investigate the effect of implant damage on dopant redistribution.

### 1.2.2 Implant Damage and Types of Extended Defects

Ion implantation is a well-known technique for controllably introducing dopants into the substrate during IC fabrication. The major disadvantage of ion implantation is the damage introduced by the energetic ions and the need for post-implantation annealing to activate the dopant.

Different types of extended defects form after annealing, depending on both the implant and the annealing conditions. It is important to understand the defect formation kinetics in order to study the effect of defects on dopant diffusion.

As an incident ion penetrates into the substrate, it loses kinetic energy through elastic collisions with the nuclei and inelastic collisions with electrons of the target material until it stops. Elastic collisions are primarily responsible for the lattice displacements through the production of Frenkel pairs. If the kinetic energy transferred to the host atom is higher than the displacement threshold energy ( $\sim 15\text{eV}$  for Si)<sup>41</sup>, the host atom leaves its lattice site (primary collision) and collides with other atoms (secondary collision), which in turn gives rise to more collisions. This sequence results in a collision cascade. For a sufficiently high concentration of damage, it is possible to amorphize the crystalline silicon near the surface. If the damage density is not high enough, some

isolated amorphous pockets may form without overlapping into a fully amorphized layer. Different damage levels will result in different types of extended defects after post-implantation annealing.

Residual implantation damage can be visible in the TEM or submicroscopic such as dopant clusters. Extended defects visible in a TEM are categorized according to two formation mechanisms: point defect condensation and solid phase regrowth.<sup>42,43</sup> There are three types of extended defects that arise from the first mechanism and two types from the second mechanism, as will be discussed below.

## I. Extended defects from point defect condensation

### 1. Sub-amorphization defects

When the implant damage is not sufficient to turn the silicon surface into a continuous amorphous layer, sub-amorphization defects form during subsequent annealing. These defects arise from a supersaturation of point defects due to the non-conservative nature of the implantation process. They form around the projected range of the implanted ions, where the supersaturation level is the highest. These defects have two common forms: rod-like {311} defects and dislocation loops. Sub-amorphization {311} defects are one of the main interests of the present study and they will be discussed in detail in the next section.

### 2. End-of-range defects

When the silicon surface has been amorphized during implantation, end-of-range defects form just below the

amorphous/crystalline interface upon annealing. End-of-range defects may consist of both dislocation loops and {311} defects if the annealing temperature is low. These defects are important in IC processing since amorphous layers are always present for P, As and BF<sub>2</sub> implants under the implant conditions that are usually used. For more information about the formation and evolution of these defects, please refer to references 42-46.

### 3. Precipitation related defects

If the concentration of the implanted impurity is above its solid solubility in silicon, precipitation related defects may form around the projected range. The precipitation process may generate such a high concentration of intrinsic point defects that extended defects can form as a result. The most common example of this is after high dose arsenic implantation.<sup>43,47,48</sup> Two layers of dislocation loops have been observed upon annealing, one at the projected range which is associated with As clustering, the other at the end of range which is associated with excess interstitials beyond the amorphous/crystalline interface.

## II. Extended defects from solid phase regrowth

### 1. Regrowth defects

When the solid phase epitaxial regrowth process is imperfect, defects nucleate at the advancing amorphous/crystalline interface and propagate into the regrowing silicon. They do not appear to dramatically affect the diffusivity of dopants, but they can getter impurities

and provide leakage paths if they span across a junction.<sup>42,49,50</sup>

## 2. Clamshell defects

If the implant energy is sufficient but the dose is not too high, it is possible to produce a buried amorphous layer. Upon annealing two amorphous/crystalline interfaces meet and extended defects may result. These defects consist of larger dislocation loops compared to end-of-range defects.<sup>49,51</sup>

We have discussed briefly each type of extended defects due to ion implantation. Visible damage from boron implants employed in this study consisted predominantly of {311} defects in the annealing temperature range that we used. In the next section, we will review some previous studies on {311} defects in detail.

### 1.2.3 {311} Rod-like Defects

As we discussed in the last section, {311} defects can form under both sub-amorphization and amorphization conditions, providing the annealing temperature is low and/or the annealing time is short. This is summarized in Fig. 1.2.

Because of the low mass of the boron ions, the silicon substrate surface is not amorphized if the dose is below  $5 \times 10^{15} \text{ cm}^{-2}$ . Under such sub-amorphization conditions, {311} defects form at lower doses than dislocation loops. They are relatively unstable. Upon annealing, they either evolve into dislocation dipoles through an unfauling reaction or dissolve. The dissolution provides interstitials to the

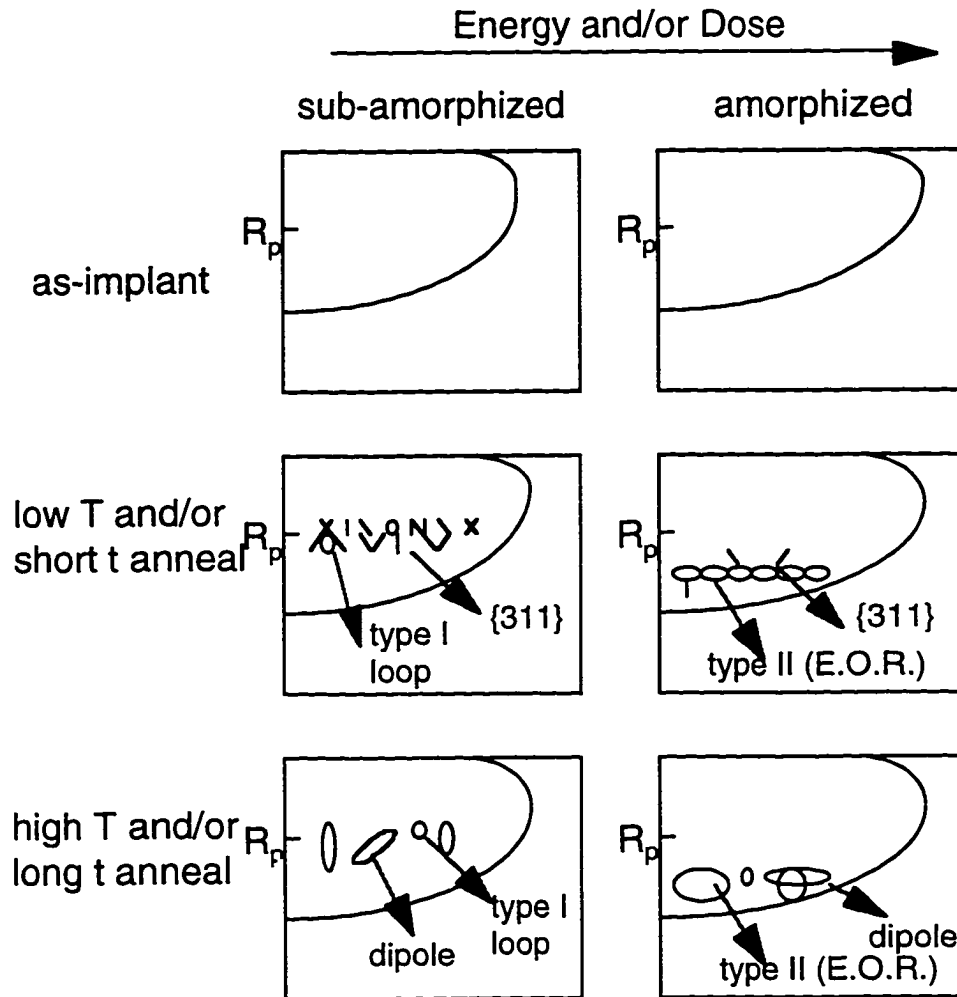


Figure 1.2. Schematic of the conditions under which  $\{311\}$  defects can form and how they evolve with time.

background environment (which can result in TED) and the growth of dislocation loops if they are present. Since  $\{311\}$  defects form after a short time and/or low temperature anneal with or without the presence of dislocation loops, and they dissolve fairly fast, they have been termed intermediate defect configurations (IDCs). As an example, Fig. 1.3 shows a plan-view transmission electron microscope picture of  $\{311\}$  defects in boron implanted silicon after an anneal at  $750^{\circ}\text{C}$  for 5 min. Under the imaging conditions used, there are

three directions of  $\{311\}$  defects. Two of them are orthogonal to each other while the third one forms a  $45^\circ$  angle to the first two sets. This morphology will be explained in the following paragraphs.

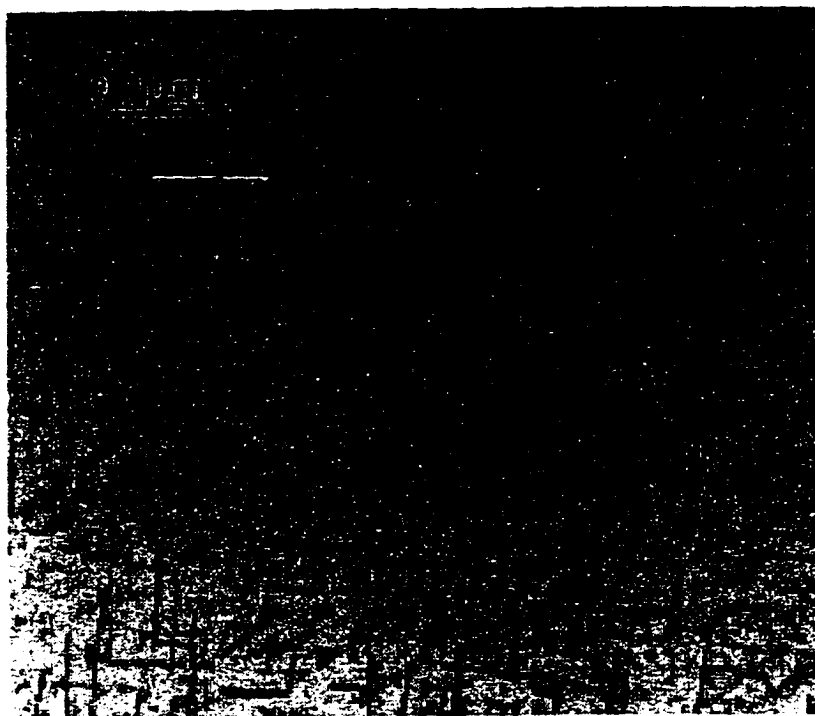


Figure 1.3. Example of  $\{311\}$  defects in  $30\text{keV } 1 \times 10^{15}\text{cm}^{-2} \text{ B}^+$  implanted Si under weak-beam dark field imaging condition with  $g_{220}$  reflection, annealed at  $750^\circ\text{C}$  for 5min in nitrogen.

$\{311\}$  defects are elongated in  $[110]$  directions and consist of interstitials precipitating on  $\{311\}$  habit planes. A unit cell of silicon lattice with  $\{311\}$  defects lying in six  $[110]$  directions is schematically shown in Fig. 1.4. The reflection vector  $g$  was chosen to be 220 when plan-view transmission electron microscopy pictures were taken in this

study. Since  $\{311\}$  defects are out of contrast for  $g$  parallel to their length, those on one of the six directions are invisible. Thus viewing on a  $[100]$  plane, we observed the morphology shown in Fig.1.3.

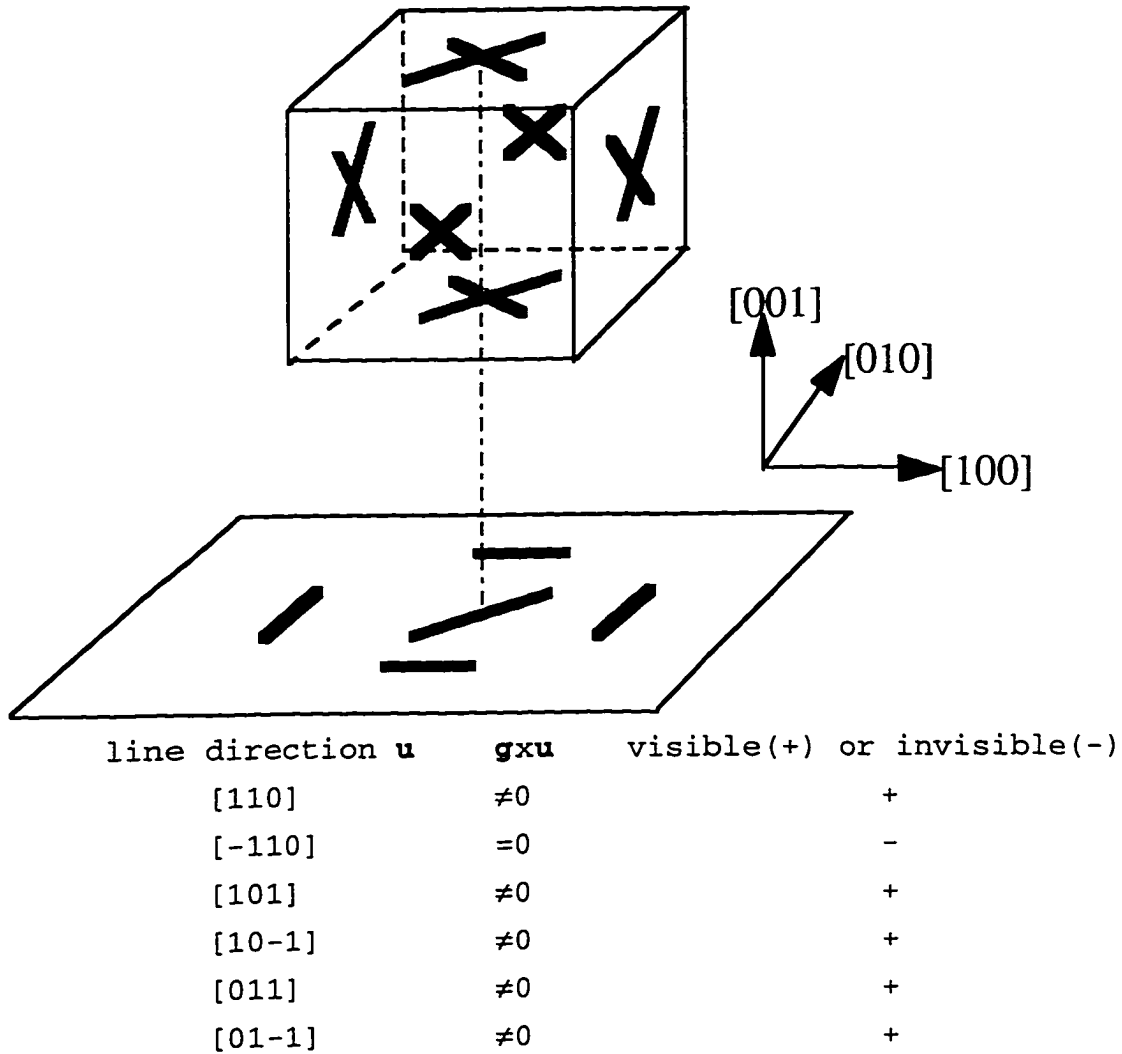


Figure 1.4. Schematic of  $\{311\}$  defect directions and defect visible conditions under reflection  $g=220$ .

Various atomic models incorporated by self-interstitials have been proposed for the  $\{311\}$  defects. Salisbury and Loretto<sup>52,53</sup> suggested that self-interstitial atoms located on the tetrahedral sites are responsible for  $\{311\}$  defect



formation. Models of split self-interstitials with or without dangling bonds were proposed by Tsubokawa et al.<sup>54</sup> and Pasemann et al.<sup>55</sup> respectively. Tan<sup>56</sup> developed a homogeneous nucleation model which shows that for extrinsic defects, a chain of interstitial atoms form  $\{311\}$  defects having non-six-membered atomic rings with matrix atoms, while for intrinsic defects, a chain of matrix atoms is cut out and the remaining atoms surrounding the cut are used to form  $\{311\}$  defects having non-six-membered atomic rings. A schematic diagram for the different steps involved in the formation of extrinsic  $\{311\}$  defects is shown in Fig.1.5 (a)~(d). This non-six-membered atomic ring configuration minimizes the dangling bond that may present.

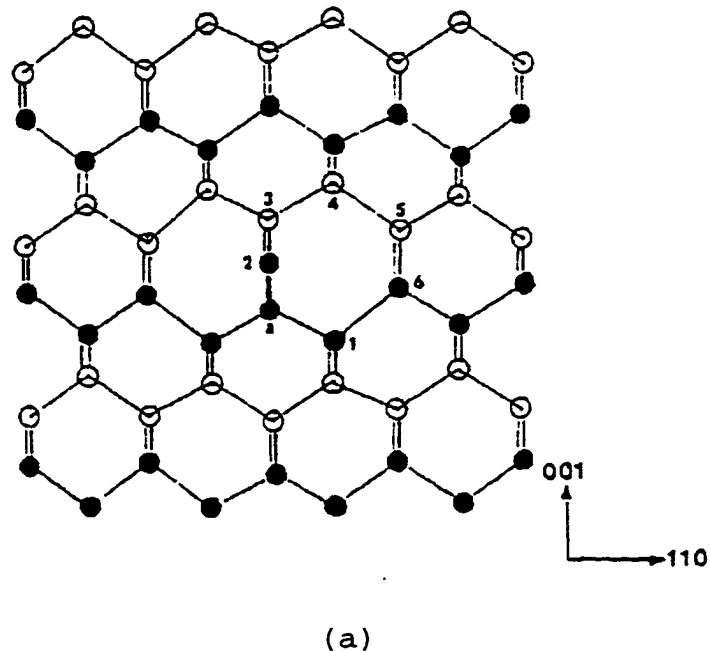
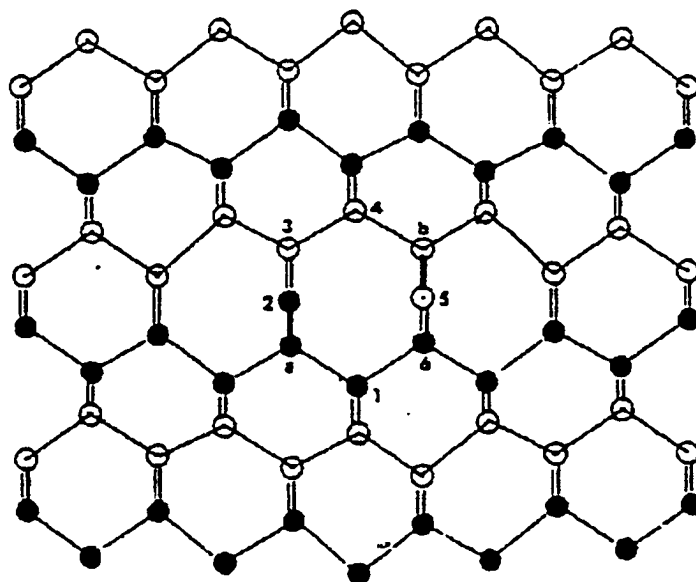
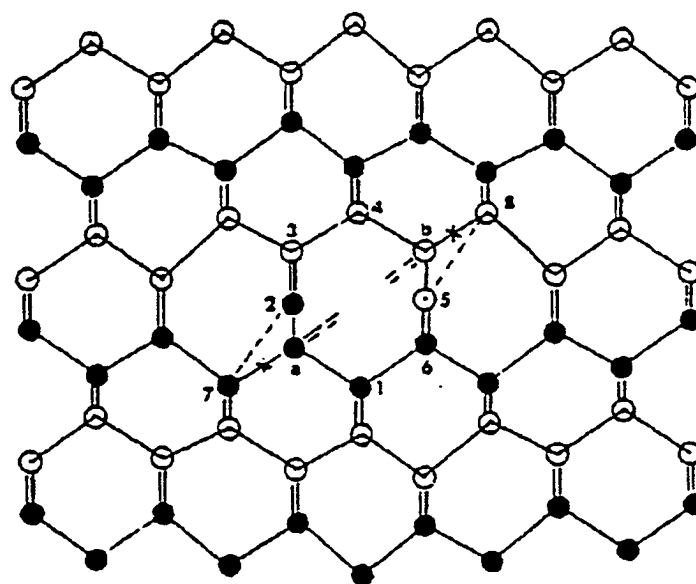


Figure 1.5. Schematic of four step  $\{311\}$  defect formation process: (a) The accepted split  $[100]$  interstitial chain, (b) The addition of one more split  $[100]$  chain, (c) Details of the bond rearrangement and (d) The resulting defect configuration.

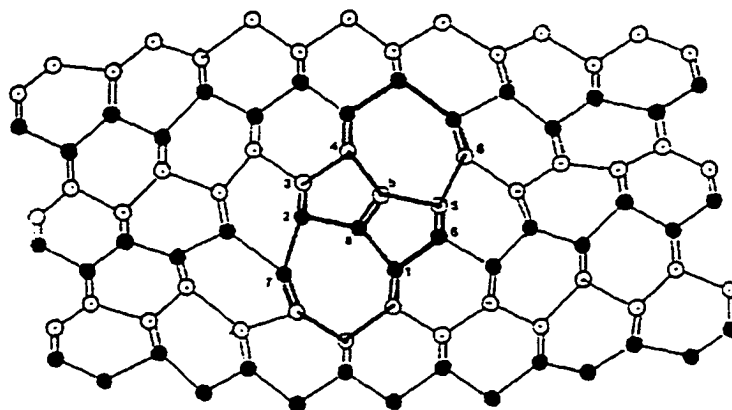


(b)



(c)

Figure 1.5. (Continued)



(d)

Figure 1.5. (Continued)

The displacement vector of  $\{311\}$  defects is perpendicular to the line and has a prominent  $[100]$  component. This vector has been determined to be  $a\langle 100 \rangle/2$ ,<sup>57</sup>  $a\langle 411 \rangle/6$ ,<sup>58</sup>  $a\langle 311 \rangle/11$ <sup>52</sup> or  $a\langle 611 \rangle/k$  by various groups, where  $a$  is the lattice constant and  $k=25$ <sup>59</sup> or  $31$ .<sup>60</sup> The discrepancy between these values reflects the inaccuracy of the measurement because of the narrowness of the defects. Different methods have been used to determine the displacement vector, including the traditional image contrast analysis and the energy minimization calculation based on the relaxation of the interstitial agglomerate model under the Stillinger-Weber potential.

$\{311\}$  defects have been studied in various ion implanted or particle irradiated systems for more than two decades. They were found in silicon,<sup>61</sup> boron,<sup>57,62-64</sup> arsenic,<sup>65</sup>

phosphorous<sup>66-68</sup> and  $\text{BF}_2$ <sup>69</sup> implanted silicon, electron,<sup>52,70</sup> neutron<sup>71</sup>, proton<sup>72</sup> and neon<sup>73</sup> irradiated silicon as well as electron irradiated germanium.<sup>59</sup> The implant temperature effect on {311} defect formation has also been studied. Tamura<sup>74</sup> found that room temperature phosphorous implants in silicon at low energies resulted in the formation of dislocation loops, whereas elevated temperature implants (200~400°C) gave rise to the formation of rod-like {311} defects. This temperature effect has also been shown by Chadderton and Eisen.<sup>75</sup> They found that dislocation loops formed in boron implanted silicon if the implantation was held at liquid nitrogen temperature, in contrast with the room-temperature implants which showed {311} defects. This behavior might arise from the self-annealing effect occurring at higher temperatures which reduces the number of free interstitials. Under this condition {311} defects may be easier to form than dislocation loops presumably because the energy to form a {311} defect is less than that of a loop.<sup>76</sup>

Back in the seventies, the formation of {311} defects was associated with the presence of boron by Seshan and Washburn.<sup>67,68</sup> They observed {311} defects in phosphorous implanted boron-doped silicon. However, the {311} defects were absent from n-type silicon under the same implant and annealing conditions. Thus they concluded that boron is essential for the formation of {311} defects. Recently, a research group at Bell Laboratories (private communication) investigated the role of boron during {311} defect formation

by studying  $\text{Si}^+$  implanted silicon doped with various concentrations of boron. They measured the number of interstitials trapped in {311} defects after the same post-implantation anneal and found that the interstitial density actually decreased with the increase of boron concentration. We have also observed a higher formation threshold of {311} defects in boron implanted than that in silicon implanted silicon. It is believed that boron atoms pair with interstitials and form submicroscopic boron interstitial clusters and mobile boron interstitial pairs, which consume part of the interstitials and reduce the number available for {311} defect formation. This will be discussed further in the following chapters. It should also be mentioned that the new interest in {311} defects arises partly from the fact that they have been claimed to be the only source of interstitials for TED, which is still controversial at this time.

#### 1.2.4 Dopant Diffusion in Silicon

The diffusion of dopant atoms can be described by

$$D_A = D_0 \exp\left(-\frac{Q_A}{kT}\right) \quad (1.1)$$

where  $D_A$  is dopant diffusivity,  $D_0$  is the pre-exponential constant and  $Q_A$  is the activation energy for diffusion. It is generally agreed that on an atomic level, dopant atoms in silicon diffuse through interactions with silicon self-interstitials and vacancies. The type of point defects which dominates the diffusion process determines the type of

diffusion mechanism, vacancy, interstitial or interstitialcy mechanism. In the vacancy mechanism, a substitutional dopant atom exchanges position with an empty lattice site. In the interstitial mechanism, the dopant atom is kicked out of the silicon lattice by a silicon self-interstitial and diffuses as a pure interstitial before returning to the lattice as a substitutional atom. In the interstitialcy mechanism, the silicon self-interstitial and the dopant atom form a diffusion pair. This process is illustrated in Fig. 1.6. Usually no distinction is made between the interstitial and the interstitialcy mechanisms.

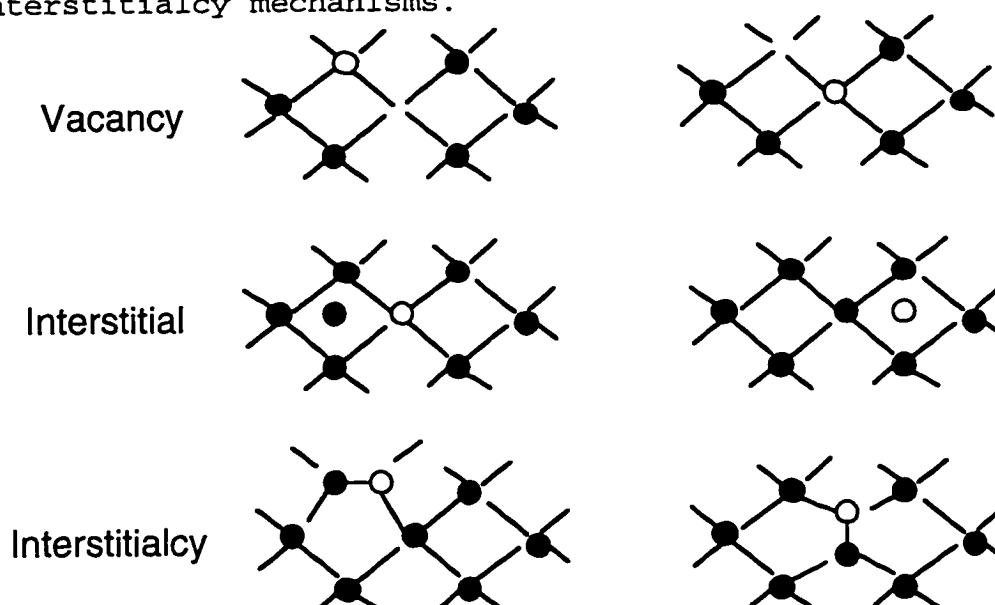


Figure 1.6. Schematic diagram of different dopant diffusion mechanisms.

If an asterisk is used to represent atoms in their free states, then the interaction of dopant atoms and the point defects can be expressed as



where  $X=I$  corresponds to interstitial/interstitialcy

mechanism while  $X=V$  refers to a vacancy mechanism.

Mathematically the ratio of dopant diffusivity under nonequilibrium conditions over its intrinsic, equilibrium value can be written as

$$\frac{D_A}{D_{A^*}} = f_{AI} \frac{C_I}{C_{I^*}} + f_{AV} \frac{C_V}{C_{V^*}} \quad (1.3)$$

where  $f_{AX} = D_{AX^*}/D_{A^*}$  ( $X=I$  or  $V$ ),  $f_{AI} + f_{AV} = 1$ ,  $C_I$  and  $C_V$  are the concentration of interstitials and vacancies under nonequilibrium conditions,  $C_{I^*}$  and  $C_{V^*}$  are the quantities under intrinsic, equilibrium conditions. Equation (1.3) shows that the diffusion of dopant atoms consists of two parts: diffusion by coupling with interstitials and with vacancies. The fraction of each is represented by  $f_{AI}$  and  $f_{AV}$ , respectively. While this treatment of diffusion allows us to mathematically explain the experimental results, it is possible that the actual mechanism is quite different.

Dopant diffusion in silicon has been under investigation for many years; however, the diffusion mechanisms responsible for some of the impurities are still under debate. It is generally accepted that antimony diffusion is dominated by a vacancy mechanism. Phosphorous and boron diffuse predominately by an interstitial/interstitialcy mechanism. Arsenic appears to diffuse by both vacancy and interstitial/interstitialcy mechanisms. The diffusion of Al, Ga and In is believed to have a strong interstitial component<sup>77</sup>. Elements such as Li, Na, He and H are believed to diffuse by an interstitial/interstitialcy mechanism as do

most of the transition metals<sup>78,79</sup>. The mechanism of Si self-diffusion appears to be vacancy controlled at temperatures <1000°C and interstitial controlled at higher temperatures.<sup>80</sup>

Boron is the diffusing species that will be discussed in this study. The set of nonequilibrium reactions involved in the kinetic model for boron diffusion is described as follows:



where  $B_S$  and  $(BI)$  are the substitutional boron and the boron interstitial pair, respectively, and  $[0]$  denotes the silicon lattice site.

The relationship between point defect concentration and dopant diffusion is given by Eq. (1.3). To understand dopant diffusion in silicon, it is necessary to understand how different processes affect point defect concentration. Because of its small value relative to the concentration of silicon atoms residing on the lattice sites, the concentration of point defects is not a quantity that can be measured directly. Diffusion studies are mostly used to gain information of the interstitials and vacancies. An enhanced diffusion of a species which diffuses by interstitial (or vacancy) mechanism indicates a supersaturation of interstitials (or vacancies) in the bulk. Ways of quantitatively monitoring these point defects will be discussed later.



Under equilibrium conditions at a particular temperature, the possible sources of point defects are chemical reactions at the silicon surface, such as oxidation,<sup>81-86</sup> nitridation<sup>87-90</sup> and silicidation,<sup>91-96</sup> the impurity clustering and precipitation,<sup>97-100</sup> and the radiation damage,<sup>20,101-105</sup> etc. Deviations from equilibrium will cause excess or depletion of either interstitials or vacancies, which will further affect dopant diffusion. For dopants that diffuse predominantly by an interstitial/interstitialcy mechanism, an excess of interstitials or depletion of vacancies will enhance the dopant diffusion, while for dopants that diffuse primarily by vacancy mechanism, the same conditions will retard dopant diffusion.

Two possible detectors for excess point defects in silicon are dopant profiles and extended defects. Dopant profiles include both epitaxially grown doping superlattices or implant profiles. Boron and antimony superlattices can be used to monitor the in-diffusion of silicon interstitials or vacancies produced by processes such as surface oxidation, nitridation, silicidation and aluminization, or the implant damage. Since boron diffuses mostly via interstitial/interstitialcy mechanism, the boron epi layer spike will broaden after oxidation and implantation during which processes interstitials are injected into the bulk. On the contrary, silicidation, nitridation and aluminization will cause vacancy injection or interstitial depletion, therefore broadening the antimony epi layer spike. The

implant profiles behave in the same way as the epi layer spikes but are less sensitive because the epi layer profiles are thinner and possess a more ideal Gaussian shape. Simulation programs such as FLOOPS can then be used to calculate the diffusivity of the dopant atoms and quantify the enhancement or retardation effect.

Other than dopant profiles, extended defects can also be used to monitor the point defect perturbation. Early studies of the trapping of point defects by extended defects were conducted by using stacking faults,<sup>82,106-108</sup> which grow by absorbing interstitials and shrink by emitting interstitials, thereby giving a good indication of the change in point defect concentration. However, because of their large size ( $> 5 \mu\text{m}$ ) and low density ( $< 10^6 \text{ cm}^{-2}$ ), the stacking faults are not ideal for detecting small perturbations. Instead, post-implantation annealed dislocation loops (end-of-range loops) have the advantage of much smaller size ( $\sim 0.02 \mu\text{m}$  in diameter) and larger density ( $\geq 10^{10} \text{ cm}^{-2}$ ), therefore being more sensitive detectors. In addition, the dislocation loops form at well-defined depth, which can not only be utilized to measure the net interstitial flux,<sup>105,109</sup> but have also been found to be an effective barrier to interstitials driving anomalous dopant diffusion.<sup>17,110,111</sup>

Extended defects themselves can act as a source of interstitials during annealing. Since dislocation loops dissolve at temperatures that are too high ( $> 1000^\circ\text{C}$ ) to explain TED which is completed within seconds at  $T > 950^\circ\text{C}$ , the

{311} rod-like defects have been examined as the possible sources of interstitials that cause TED. Cowern et al.<sup>103</sup> claimed that the release of interstitials which drive TED of boron in silicon occurs at two different time scales. Interstitials emerging from the ion collision cascade give rise to a primary (ultra fast) pulse of diffusion, and at a sufficiently high displacement density, emission of interstitials from {311} defects causes a secondary (much slower) diffusion transient. Later, Eaglesham et al.<sup>112</sup> and Stolk et al.<sup>113</sup> reported that {311} defects are the only source of interstitials driving TED based on their study of Si<sup>+</sup> implanted Si. They reasoned that interstitials are emitted from {311} defects in the damage region during annealing. This emission occurs at a rate which exhibits the same activation energy as that of the interstitial in-diffusion, and the duration of {311} dissolution process is in close agreement with that of TED. Our group have been studying {311} defects and TED in boron implanted silicon. We found that TED occurs without the formation of {311} defects if the implant energy (4 keV) and dose ( $1 \times 10^{14} \text{ cm}^{-2}$ ) are low.<sup>114</sup> The source of interstitials driving TED in this case was attributed to sub-microscopic mobile boron interstitial pairs. These B-I pairs play a key role in TED of boron in silicon, as will be discussed.

Therefore, understanding the correlation between implantation induced defects (e.g., {311} defects and boron interstitial clusters) and TED is essential to the

understanding of dopant diffusion. This correlation will be further investigated in this study.

### 1.3 Ion Implantation, Characterization and Simulation Techniques

#### 1.3.1 Ion Implantation

Ion implantation is the introduction of energetic charged particles into targets with enough energy to penetrate beyond the surface region. The ions enter the substrate, collide with the host atoms, gradually lose energy and finally come to rest at some depth within the substrate. Ion implantation is involved in several steps during the fabrication sequence of MOSFET and bipolar transistors when the controlled doping of selected areas is required.

An ion implanter consists of the following major components: an ion source, an extracting and ion analyzing system, an accelerating column, a scanning system and an end station. The ions produced by the source are extracted by a small accelerating voltage and then injected into the analyzer magnet. A spatial separation of ions subjected to the Lorentz force occurs due to the differences in the mass and charge. The selected ions are injected into the accelerating column and the rest are screened out. In this case the system operates in the pre-analysis configuration. If the ions are accelerated to their full energy before the mass separation, then it works in the post-analysis

configuration. The extraction voltage ranges usually between 15 and 40kV. For low energy implants, a retarding voltage can be used after separation. The selected ions are accelerated by a static electric field and focused and shaped in the column and ready to be implanted.

Some important quantities during the ion implantation process are listed below. The implant dose can be expressed as

$$Q_i = \frac{It}{nqA} \quad (1.7)$$

where  $I$  is the implant current,  $t$  is the time,  $n=1$  for singly ionized species and 2 for doubly ionized species,  $q$  is the charge and  $A$  is the area of the implanted surface. For an ion accelerated through a potential  $V$  and deflected through a magnetic field  $B$ , the radius of the ion's path is

$$r = \frac{1}{B} \sqrt{\frac{2MV}{q}} \quad (1.8)$$

where  $M$  is the mass of the dopant atom. In absence of crystal orientation effects, the range distribution is roughly Gaussian and to a first approximation the projected range distribution  $N(x)$  is described as a one-dimensional Gaussian profile characterized by the projected range  $R_p$  and the standard deviation  $\Delta R_p$ , as given by

$$N(x) = \frac{Q}{\sqrt{2\pi}\Delta R_p} \exp\left[-\frac{1}{2}\left(\frac{x-R_p}{\Delta R_p}\right)^2\right] \quad (1.9)$$

Schematic diagram of an implanted impurity profile is shown in Fig. 1.7. Due to the channeling effect, the use of a Gaussian profile is not accurate. The UT-Marlowe code (a

Monte Carlo simulator) yields a much more accurate picture of the ion distribution just after implantation.

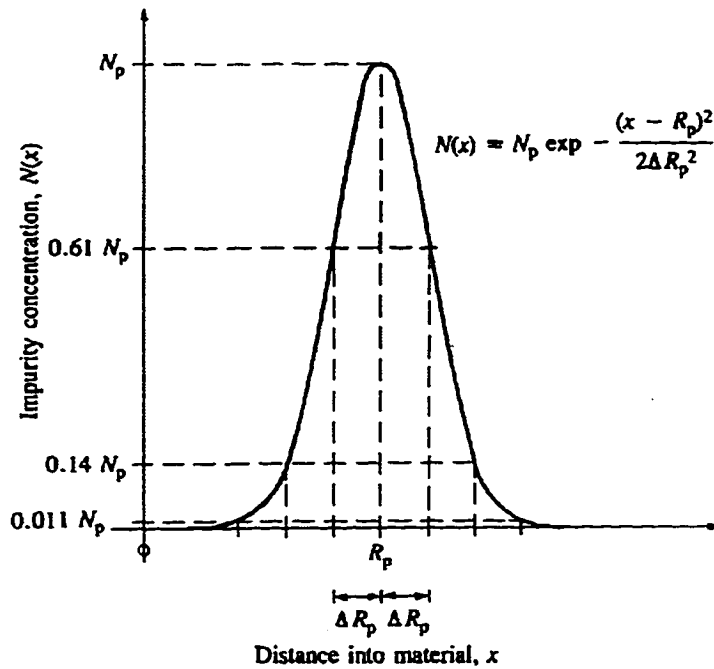


Figure 1.7. Schematic illustration of a Gaussian distribution resulting from ion implantation.

### 1.3.2 Transmission Electron Microscopy

The transmission electron microscope (TEM) is used to obtain information from samples which are thin enough to transmit electrons. A bright-field image is formed if the directly transmitted beam is selected and a dark-field image is formed if a diffracted beam is selected. Dark-field images normally have higher resolution than bright-field images and this is the mode we used in our study. The defect structure can be analyzed by both plan-view and cross-sectional TEM. Plan-view TEM (PTEM) is used to study the defect evolution during annealing and cross-sectional TEM

(XTEM) is used to get the side view and the depth of the defect layer.

To make a PTEM sample, the sample is first cut into 3mm diameter pieces using an ultrasonic disk cutter. The small disk is then polished down to about half of its original thickness using a polishing jig with 15 $\mu$ m aluminum oxide powder. A coat of wax is then applied to the top surface (i.e. the implanted surface) of the sample to protect it during the etch. The sample is mounted with wax on a Teflon holder facing down and etched from the back side in a jet etcher using a HF:HNO<sub>3</sub>=25%:75% solution until a small hole with an electron transparent region around it is obtained. The wax is then removed from the sample using heptane and/or acetone and the sample is ready for analysis.

To make a XTEM specimen, a piece of silicon wafer is cut into 10mil thick strips using a dicing saw. The top surface of the two strips is coated with M600 Bond epoxy resin. The two top surfaces are then brought into close contact with each other. Two silicon dummy strips can also be glued on the side of each sample strip to improve the mechanical stability. The bonded strips are heated in a conventional oven at 100°C for 1hr to harden the epoxy resin. The cured strips are then polished down to a thickness of about 40 $\mu$ m using 5 $\mu$ m aluminum oxide powder. A copper ring is mounted onto the thinned strips using the M600 Bond, leaving the interface of the sample strips exposed in the center of the ring. The specimen is then further thinned in a Gatan two-

stage ion mill by using two  $\text{Ar}^+$  ion guns at a gun voltage of 4 kV and a gun current of 0.5 mA until a small hole is obtained at the sample strips' interface. The region in the vicinity of the hole is sufficiently thin ( $<0.5 \mu\text{m}$ ) to be transparent to the electron beam of the TEM.

### 1.3.3 Secondary Ion Mass Spectroscopy

In secondary ion mass spectroscopy (SIMS), an energetic beam of focused ions is directed at the sample surface in a high or ultrahigh vacuum environment. The momentum transfer from the impinging primary ions to the sample surface causes sputtering of the surface atoms and molecules. The most commonly used sputtering ions are  $\text{Cs}^+$ ,  $\text{O}_2^+$ ,  $\text{O}^+$  and  $\text{Ar}^+$  in the energy range from 2 to 20 keV at angles of incidence between  $45^\circ$  and  $90^\circ$ .  $\text{O}_2^+$  ions are used in this study to enhance secondary ion yield. Some of the sputtered species are ejected with positive or negative charges. These are termed secondary ions. The secondary ions are then mass analyzed using a mass spectrometer. SIMS can be used to obtain a depth concentration profile of the near-surface region to a resolution of 2~30 nm at a detection limit of  $10^{12}$ ~ $10^{16} \text{ cm}^{-3}$ . For further information see ref.115

### 1.3.4 Florida Object Oriented Process Simulator

FLOOPS modeling program is a physically based two-dimensional process simulator capable of modeling a complex device structure. It uses local point defect concentration



to determine dopant diffusivities. In order to keep track of the spatial distribution of point defects, FLOOPS solves the diffusion equations for the dopant atoms as well as the equivalent equations for the point defects. Since vacancies and interstitials can interact, the equations describing their motion are coupled. The equations used to determine dopant diffusion include

$$\frac{\partial C_A}{\partial t} = -\nabla \cdot J_A \quad (1.10)$$

$$J_A = -K_{tr} \left( C_{A1} - \frac{C_{A2}}{m} \right) \quad (1.11)$$

$$J_A = -\sum_X D_{AX} C_A \frac{C_X}{C_X^*} \nabla \ln \left( C_A \frac{C_X}{C_X^*} \frac{n}{n_i} \right) \quad (1.12)$$

where  $J_A$  is the flux of the dopant,  $C_A$  is the total concentration of the dopant species, the summation over  $X$  is for all possible diffusion mechanisms,  $C_X$  is the concentration of the  $X$  species,  $D_{AX}$  is the diffusivity corresponding to the  $X$  mechanism,  $n_i$  and  $n$  refer to the intrinsic and actual electron concentrations,  $C_{A1}$  and  $C_{A2}$  are the concentration of the dopant species on the two sides of a materials boundary,  $K_{tr}$  is the transport coefficient across the material boundary and  $m$  is the segregation coefficient of the dopant for the boundary materials. The equations solved for interstitials or vacancies are

$$\frac{\partial C_x}{\partial t} = -\nabla \cdot J_x - K_{bulk} (C_I C_V - C_I^* C_V^*) \quad (1.13)$$

$$G_x = J_x + K_{xs} (C_x - C_x^*) \quad (1.14)$$

$$J_x = -D_x C_x^* \nabla \frac{C_x}{C_x^*} \quad (1.15)$$

where  $x=I$  for interstitials and  $V$  for vacancies,  $J_x$  is the flux of the  $X$  point defect species,  $C_x^*$  and  $C_x$  are the

equilibrium and actual concentrations of X,  $G_X$  is the surface generation rate for X,  $K_{XS}$  is the surface recombination constant and  $K_{bulk}$  is the bulk recombination constant.

For the case of dopant diffusion following an implantation, the initial distribution of point defects is determined by the implantation process. These point defects then diffuse according to the above equations. Anomalous diffusion can be observed until the point defect concentrations return to the equilibrium values, when only normal diffusion can be seen.

#### 1.4 Thesis Statement

The contributions of this work are in the following areas:

1. Determination of the formation threshold of extended defects in low energy  $B^+$  implanted silicon.
2. Quantitative TEM studies of the annealing kinetics of {311} defects arising from B implantation.
3. Experimental investigation of the implant energy and dose effects on {311} defect behavior.
4. Experimental investigation of the implant energy and dose effects on TED.
5. Extraction of diffusivity enhancement for different implant energies, doses, annealing times and temperatures.
6. Experimental investigation of the sources of interstitials driving dopant diffusion.

7. Provision of experimental basis for the improvement of process development and process simulators.

## CHAPTER 2 THE FORMATION THRESHOLD OF {311} DEFECTS AND SUB- AMORPHIZATION DISLOCATION LOOPS

### 2.1 Overview

The formation of very shallow p-type region by ion implantation requires the use of low energy boron implants. Although there have been many reports on the defect and diffusion behavior in boron implanted silicon,<sup>63,116-118</sup> none of them have systematically studied the defect formation threshold in the low energy implantation regime. For boron implantation, because of the low mass of the implanted ions, even if the ion fluences reach  $2 \times 10^{15} \text{ cm}^{-2}$ , the damaged surface layer still does not amorphize. In this case the extended defects that form after annealing can be classified as type I or sub-amorphization defects. The implant energy and dose combinations in this study are similar to those used in the semiconductor industry for B implants and fall in the sub-amorphization regime.

In order to understand how the sub-amorphization defects influence dopant diffusion, it is important to know the implant conditions under which these defects are actually formed. This is the purpose of this section of the current study.

## 2.2 Experimental Procedure

Czochralski-grown (100) n-type 8-20  $\Omega\text{cm}$  150 mm wafers were implanted with boron ions at energies of 5 keV, 10 keV, 20 keV, 30 keV and 40 keV to doses of  $5 \times 10^{13} \text{ cm}^{-2}$ ,  $1 \times 10^{14} \text{ cm}^{-2}$ ,  $2 \times 10^{14} \text{ cm}^{-2}$ ,  $5 \times 10^{14} \text{ cm}^{-2}$  and  $1 \times 10^{15} \text{ cm}^{-2}$ . The tilt/rotation angles were  $5^\circ/0^\circ$ . The implant current was 3 mA. During ion implantation, the samples were kept at room temperature using water cooling. Furnace anneals were then performed at  $750^\circ\text{C}$  for 5 min or  $900^\circ\text{C}$  for 15 min in a nitrogen ambient to study the formation threshold of {311} defects and sub-amorphization dislocation loops respectively. Plan-view transmission electron microscopy (PTM) samples were prepared using standard jet-etching procedures and Cross-sectional TEM (XTEM) samples were prepared using ion-milling. Micrographs were taken from each sample to examine the presence or absence of secondary defects. The g220 reflection was used to acquire all the micrographs under weak-beam dark field imaging conditions. A defect density of  $1.2 \times 10^7 \text{ cm}^{-2}$  was used to distinguish between samples with and without extended defects, i.e., if no defect is observed in three randomly-picked areas each with a size of  $7 \times 10 \text{ cm}^2$  under a magnification of 50000X, then it is stated that there are "no" defects in that sample.

### 2.3 Defect Microstructure

Figure 2.1 shows PTEM micrographs of some of the samples in the implant matrix after an anneal at 750°C for 5 min. Micrographs of 5 keV, 20 keV and 40 keV implants with doses of  $1 \times 10^{14} \text{ cm}^{-2}$ ,  $2 \times 10^{14} \text{ cm}^{-2}$  and  $5 \times 10^{14} \text{ cm}^{-2}$  are shown in the figure. At a dose of  $1 \times 10^{14} \text{ cm}^{-2}$ , there are no {311} defects in the 5 keV sample and the defect density increases with increasing energy. When the dose is doubled to  $2 \times 10^{14} \text{ cm}^{-2}$ , there are still no {311} defects in the 5 keV sample, but more defects are observed in the other two implants. Increasing the dose further to  $5 \times 10^{14} \text{ cm}^{-2}$  results in {311} defect formation at 5 keV. Figure 2.1 clearly presents a transition from samples without to those with {311} defects. It is obvious that as the implant energy increases, the critical dose for forming {311} defects decreases. From this figure it is also obvious that the interstitial supersaturation necessary to nucleate {311} defects is far less than that for dislocation loops. This is consistent with Eaglesham's observation (private communication) of {311} defects at  $7 \times 10^{12} \text{ cm}^{-2}$  for 40 keV Si implants and the observation of Jones et al.<sup>42</sup> that stable dislocation loops (approximately the same implant energy) do not form until a dose of  $2 \times 10^{14} \text{ cm}^{-2}$ . In addition, the threshold dose for {311} defects in a 20 keV B implant is around  $2 \times 10^{14} \text{ cm}^{-2}$ , which is much greater than the threshold dose of  $7 \times 10^{12} \text{ cm}^{-2}$  for a comparable depth of 40 keV Si implant. This is

presumably due to the formation of immobile boron interstitial clusters and mobile boron interstitial pairs that reduces the concentration of free interstitials available to form {311} defects.

PTEM micrographs of selective samples annealed at 900°C for 15min are shown in Fig. 2.2. This temperature/time condition was chosen to reveal stable sub-amorphization dislocation loops and dipoles that evolve from unstable {311} defects. The {311} defects have completely dissolved after the anneal. A submatrix of 5 keV, 20 keV and 40 keV implants with doses of  $2 \times 10^{14} \text{ cm}^{-2}$ ,  $5 \times 10^{14} \text{ cm}^{-2}$  and  $1 \times 10^{15} \text{ cm}^{-2}$  are shown in Fig. 2.2. The 40 keV sample has dislocation loops and dipoles at a dose of  $2 \times 10^{14} \text{ cm}^{-2}$ . The 20 keV and 5 keV samples do not show loops or dipoles until the dose is increased to  $5 \times 10^{14} \text{ cm}^{-2}$ . The critical dose for type I loop formation appears to decrease with increasing implant energy. The threshold dose at 40 keV ( $2 \times 10^{14} \text{ cm}^{-2}$ ) matches the previous results of Jones et al.'s for 30 keV boron. Table 2.1 lists the formation threshold for both {311} defects and [110] loops for the whole implant matrix.

XTEM micrographs of 10 keV, 20 keV, 30 keV and 40 keV implants to a dose of  $1 \times 10^{15} \text{ cm}^{-2}$  after an anneal at 750°C for 5 min are shown in Fig. 2.3. The reason for choosing the highest dose in our implant matrix is that both {311} defects and dislocation loops are present in these implants under this annealing condition. A layer of sub-amorphization extended defects is expected to form at the projected range

$R_p$ . Compared with the SIMS profiles which will be shown later in Chapter 4, the depth of the defect layer was found to correspond to  $R_p$ . Both the distance between the defect layer and the surface and the width of the defect layer decrease as implant energy decreases. This decrease of distance between the damage region and the surface may induce a more prominent recombination effect at the surface, as will be discussed later.

#### 2.4 Criteria for the formation of {311} Defects and Sub-amorphization Loops

Various suggestions have been made for the criterion for secondary defect formation. Tamura et al.<sup>119</sup> have stated that implant dose can be used as such a criterion. They studied defect formation in 1~2 MeV B, P and As implanted silicon and found that secondary defects form if the dose range of  $2 \times 10^{13} \sim 1 \times 10^{14} \text{ cm}^{-2}$  is exceeded, independent of the implant species. Other experiments, however, show that a higher dose is required for defect formation if the ion mass is smaller. Gibbons<sup>120</sup> studied B, Al, N, P, Sb, Ne and Si implanted silicon at energies from 40 keV to 100 keV. The threshold for small loop formation for Sb implant is about  $5 \times 10^{13} \text{ cm}^{-2}$  while for B implant it is above  $1 \times 10^{14} \text{ cm}^{-2}$ . This implies that the implant dose cannot be the sole criterion for loop formation. Furthermore, the results of studies on channeling versus random implants show that the defect formation is not dependent only on impurity dose but on the damage introduced



during implantation. Raineri et al.<sup>121</sup> studied random and [100] channeling implants with B and P ions. 100 keV P implants with doses from  $5 \times 10^{13} \text{ cm}^{-2}$  to  $2 \times 10^{14} \text{ cm}^{-2}$  does not show defects under channeling conditions after an anneal at 500°C for 1 hr. The same implants in a random direction give rise to a network of dislocation loops. A systematic study on implant damage using TEM, RBS and TRIM simulations was reported by Schreutelkamp et al.<sup>122</sup> They claimed that if the total number of silicon atoms displaced by the implant ions exceeds a critical value, stable sub-amorphization dislocation loops are observed. They implanted Si with B, Si, P, Ga, As, In and Sb ions at keV and MeV energies. For B implants with energies ranging from 50 keV to 190 keV, the critical value of displaced Si atoms was  $4.7 \times 10^{16} \text{ cm}^{-2}$  based upon TRIM calculations and  $1.4 \times 10^{16} \text{ cm}^{-2}$  based upon Rutherford Backscattering (RBS) analysis. This value increases with the mass of the implant ions. To the author's best knowledge, there has been no report on the formation threshold of {311} defects or stable loops in the low energy (<20 keV) regime of B implanted silicon.

We have calculated the number of displaced silicon atoms using TRIM for our implant matrix and the results are listed in Table 2.2. As can be seen, when the displaced atom density reaches about  $1.5 \times 10^{16} \text{ cm}^{-2}$ , {311} defects form, and when it reaches about  $2.6 \times 10^{16} \text{ cm}^{-2}$ , sub-amorphization loops form. The latter value is less than the result of Schreutelkamp et al., but considering the fact that we used a

new version of TRIM, the results are in reasonable agreement. It thus appears that the number of displaced silicon atoms can be used effectively as the criterion for both {311} defect and sub-amorphization dislocation loop formation.

If the above argument is true, we expect to see more extended defects after annealing in samples containing more displaced silicon atoms after implantation. This indeed is the case for both anneal conditions with only two exceptions. The first is the 5 keV  $1 \times 10^{15} \text{ cm}^{-2}$  implant after an anneal at 750°C for 5 min (Fig. 2.1). Keeping the dose at  $1 \times 10^{15} \text{ cm}^{-2}$ , we see less {311} defects but more dislocation loops in the 5 keV implant than in the higher energies. The reason might be that the 5 keV  $1 \times 10^{15} \text{ cm}^{-2}$  implant has the highest interstitial concentration in the whole implant matrix. When the number of free interstitials reaches a critical value, the system may form loop nuclei. If the energetics are such that interstitials would rather be in a loop, then the loop/{311} ratio increases, i.e., loop formation might be more favorable than {311} defect formation. The second exception to the damage alone being the reason for threshold changes arises when one compares the 5 keV and the 20 keV implant. The displaced atom density for 5 keV  $5 \times 10^{14} \text{ cm}^{-2}$  implant ( $2.56 \times 10^{16} \text{ cm}^{-2}$ ) is slightly less than that of the 20 keV  $2 \times 10^{14} \text{ cm}^{-2}$  implant ( $2.94 \times 10^{16} \text{ cm}^{-2}$ ) (Table 2.2), but after an anneal at 900°C for 15 min, the 5 keV sample shows a low density of half loops while the 20 keV implant shows no defects. The reason might be that these displaced atom

densities are near the threshold for defect formation so the behavior is due to the other fluctuations. However, the reason may also be due to the above argument for why loops are seen most prominently for 5 keV implant.

Besides the effect of implant energy on damage production, interstitial recombination at the sample surface may also affect the formation of secondary defects. Figure 2.4 shows the projected range  $R_p$  as a function of implant energy obtained from the XTEM micrographs and the SIMS profiles which will be shown in Chapter 4.  $R_p$  increases with increasing energy. It is about 230Å for the 5keV implant and about 1750Å for the 40keV implant according to SIMS. As the implant energy decreases, the damage region gets closer to the sample surface. Surface recombination could then become more efficient and thus reduce the number of free interstitials available to form secondary defects. It is difficult to determine which effect, decreased damage, increased boron interstitial cluster formation due to higher interstitial supersaturation in the dopant peak region or increased surface recombination, is primarily responsible for the increased threshold dose with decreasing implant energy. Additional experiments to sort out these effects will be necessary.

In summary, the formation threshold for both {311} rod-like defects and [110] dislocation loops in low energy boron implanted silicon have been investigated. A matrix was chosen with implant energies ranging from 5keV to 40keV and

doses from  $5 \times 10^{13} \text{cm}^2$  to  $1 \times 10^{15} \text{cm}^{-2}$ . TEM was used to evaluate the presence of both types of defects. It was observed that the threshold dose for both {311} defect and sub-amorphization dislocation loop formation increases significantly with decreasing implant energy. This threshold is higher for boron implants than for silicon implants presumably because of the formation of boron interstitial clusters and mobile boron interstitial pairs. As discussed earlier there are several possible explanations for the higher threshold dose with decreasing implant energy. These include a decrease in the displaced atom density, increased formation of boron interstitial clusters and/or increased surface recombination. Experimentally a displaced atom density of about  $1.5 \times 10^{16} \text{cm}^{-2}$  for {311} defects and  $2.6 \times 10^{16} \text{cm}^{-2}$  for sub-amorphization loops from TRIM calculations reasonably predicts defect formation for these implant conditions. However, the results of Zhang et al.<sup>114</sup> and Eaglesham et al. (private communication) clearly indicate that boron is a very effective interstitial trap and that increasing the boron concentration clearly results in an increase in the concentration of interstitial trapping.

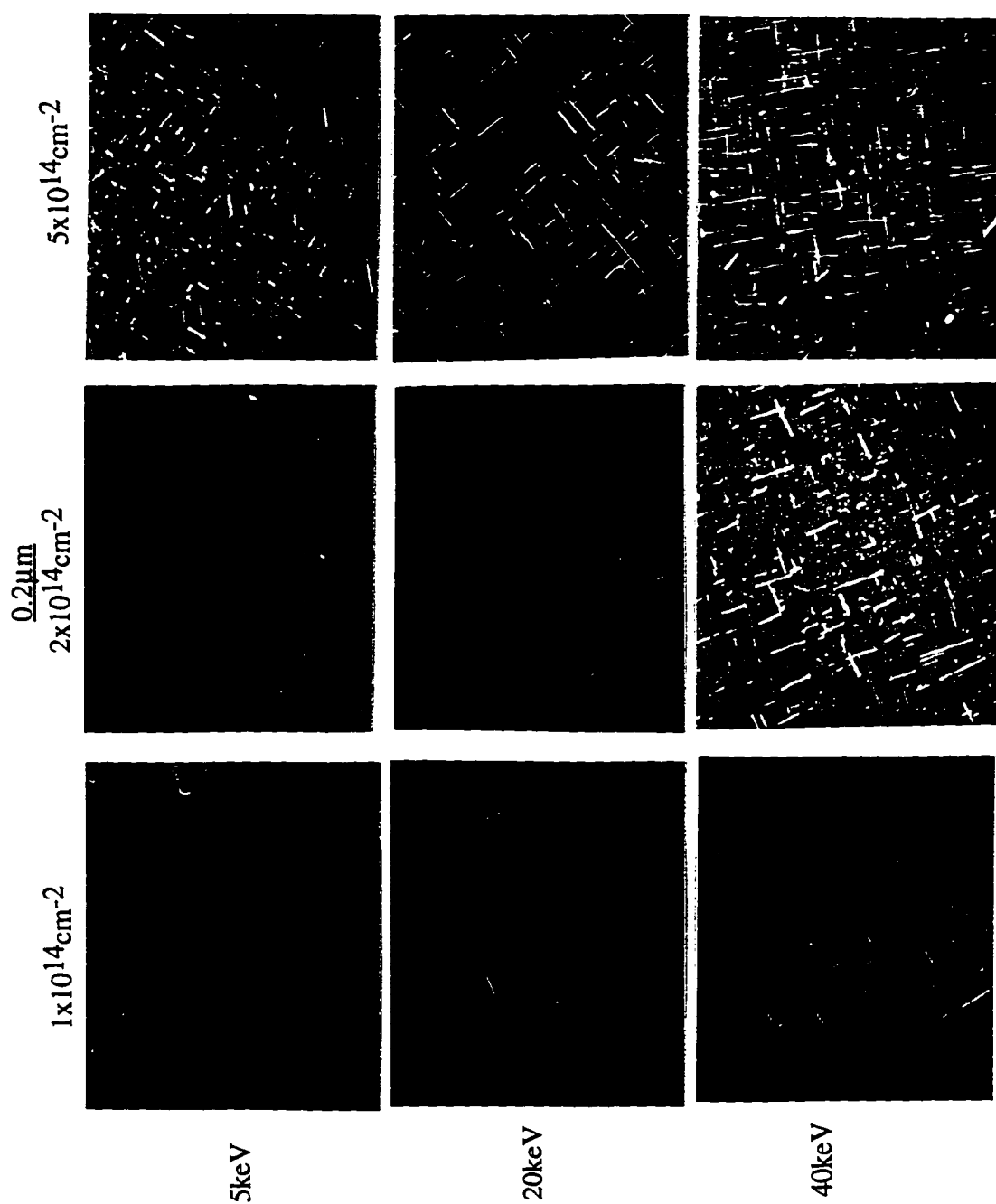


Figure 2.1. Weak beam dark field (g220) PTM images of 5keV, 20keV and 40keV  $\text{B}^+$  implanted Si to doses of  $1 \times 10^{14} \text{cm}^{-2}$ ,  $2 \times 10^{14} \text{cm}^{-2}$  and  $5 \times 10^{14} \text{cm}^{-2}$ , after an anneal at  $750^\circ\text{C}$  for 5min in  $\text{N}_2$ .

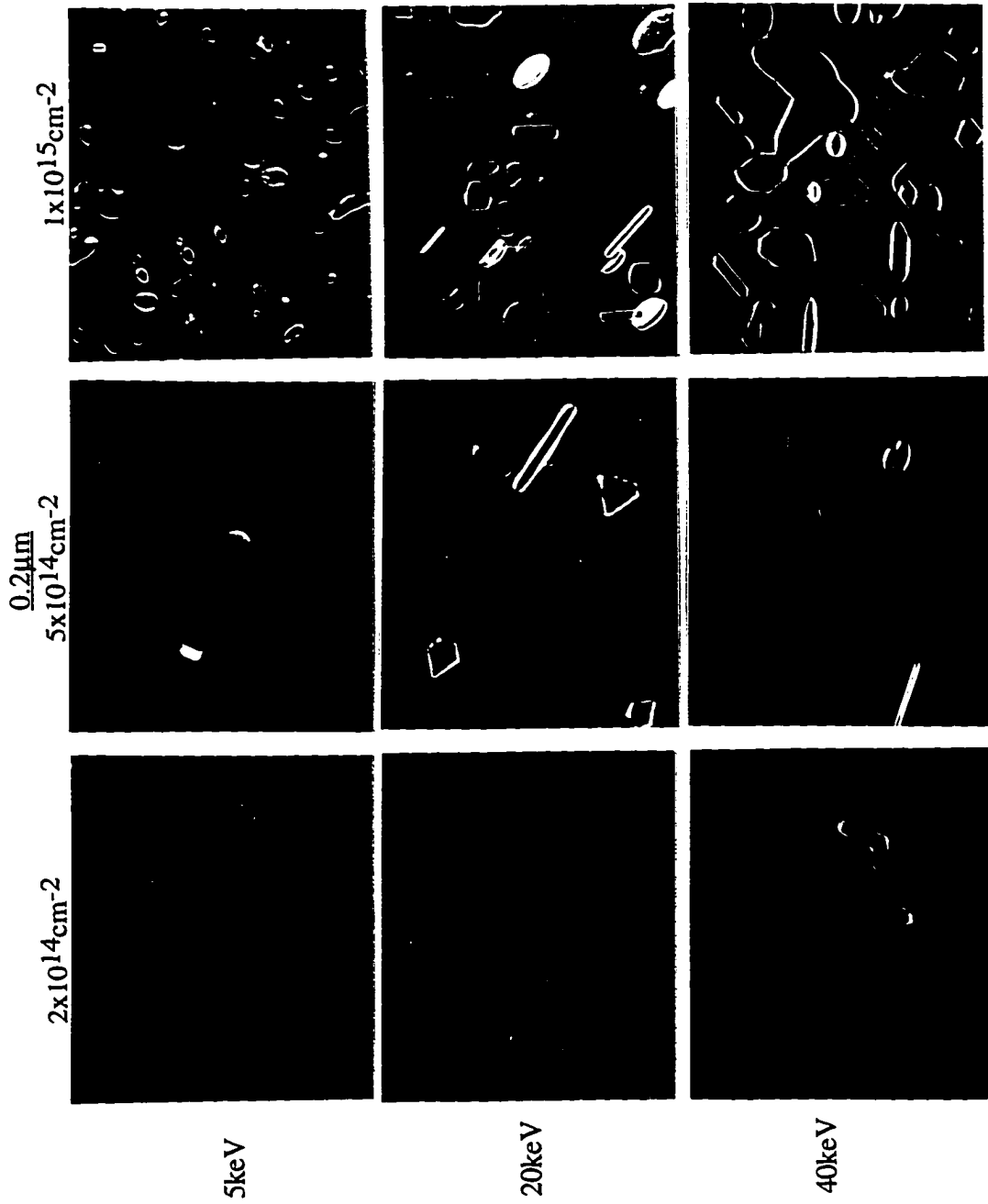


Figure 2.2. Weak beam dark field (g220) PTM images of 5keV, 20keV and 40keV  $\text{B}^+$  implanted Si to doses of  $2 \times 10^{14} \text{cm}^{-2}$ ,  $5 \times 10^{14} \text{cm}^{-2}$  and  $1 \times 10^{15} \text{cm}^{-2}$ , after an anneal at  $900^\circ\text{C}$  for 15min in  $\text{N}_2$ .

Table 2.1 Types of extended defects formed in B<sup>+</sup> implanted silicon

	5keV	10keV	20keV	30keV	40keV
$5 \times 10^{13} \text{cm}^{-2}$	none	none	none	none	none
$1 \times 10^{14} \text{cm}^{-2}$	none	none	{311}s	{311}s	{311}s
$2 \times 10^{14} \text{cm}^{-2}$	none	{311}s	{311}s	{311}s Loops	{311}s Loops
$5 \times 10^{14} \text{cm}^{-2}$	{311}s Loops	{311}s Loops	{311}s Loops	{311}s Loops	{311}s Loops
$1 \times 10^{15} \text{cm}^{-2}$	{311}s Loops	{311}s Loops	{311}s Loops	{311}s Loops	{311}s Loops

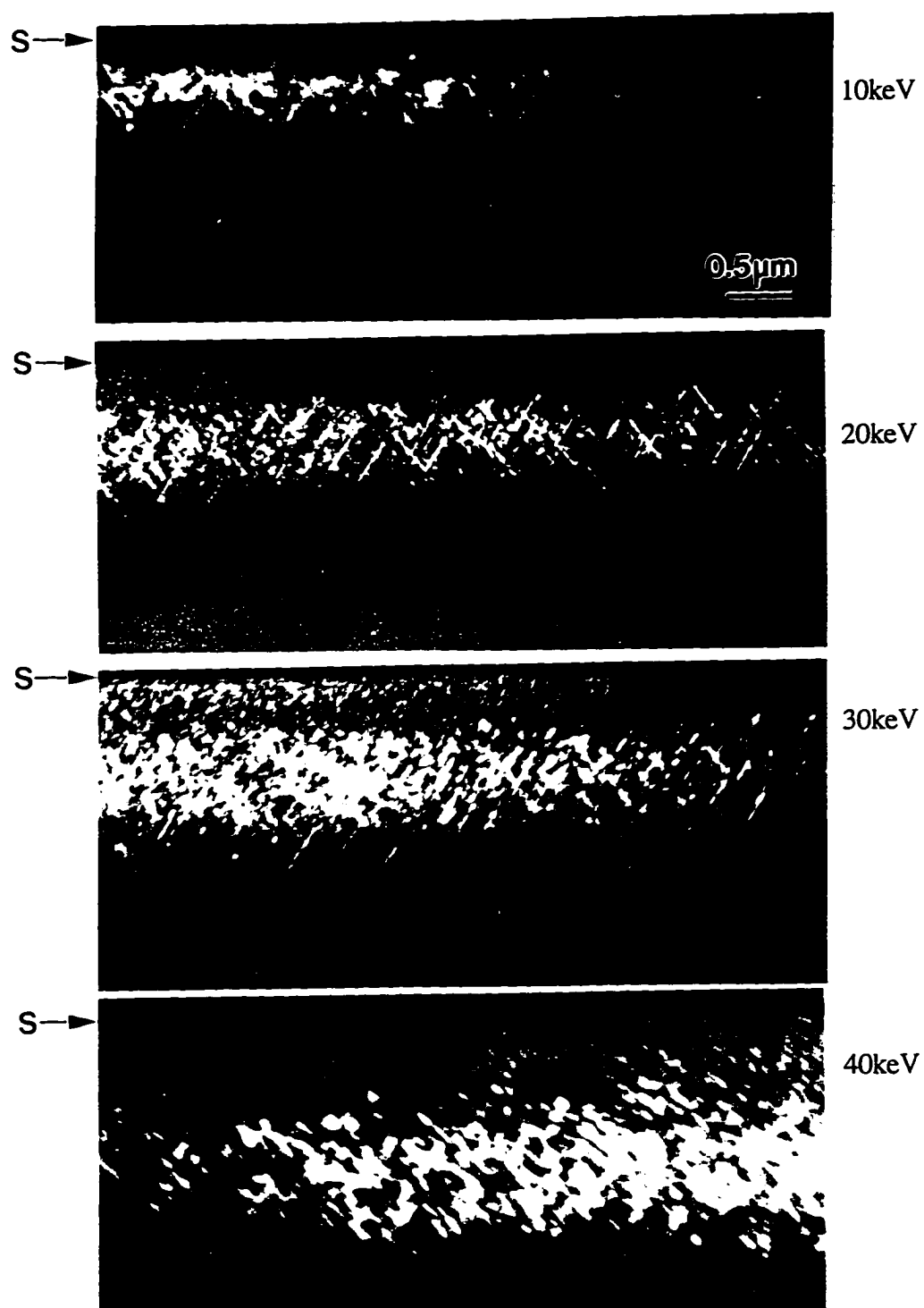


Figure 2.3. Weak beam dark field ( $g_{220}$ ) XTEM images of 10keV, 20keV, 30keV and 40keV  $B^+$  implanted Si to a dose of  $1 \times 10^{15} \text{cm}^{-2}$ , after an anneal at  $750^\circ\text{C}$  for 5min in  $N_2$ .



Table 2.2 Displaced atom density (#/cm<sup>2</sup>) from TRIM calculations  
(B<sup>+</sup> implanted silicon)

	5keV	10keV	20keV	30keV	40keV
5x10 <sup>13</sup> cm <sup>-2</sup>	2.56e15	4.51e15	7.35e15	9.60e15	1.16e16
1x10 <sup>14</sup> cm <sup>-2</sup>	5.12e15	9.02e15	1.47e16	1.92e16	2.31e16
2x10 <sup>14</sup> cm <sup>-2</sup>	1.02e16	1.80e16	2.94e16	3.84e16	4.62e16
5x10 <sup>14</sup> cm <sup>-2</sup>	2.56e16	4.51e16	7.35e16	9.60e16	1.16e17
1x10 <sup>15</sup> cm <sup>-2</sup>	5.12e16	9.02e16	1.47e17	1.92e17	2.31e17

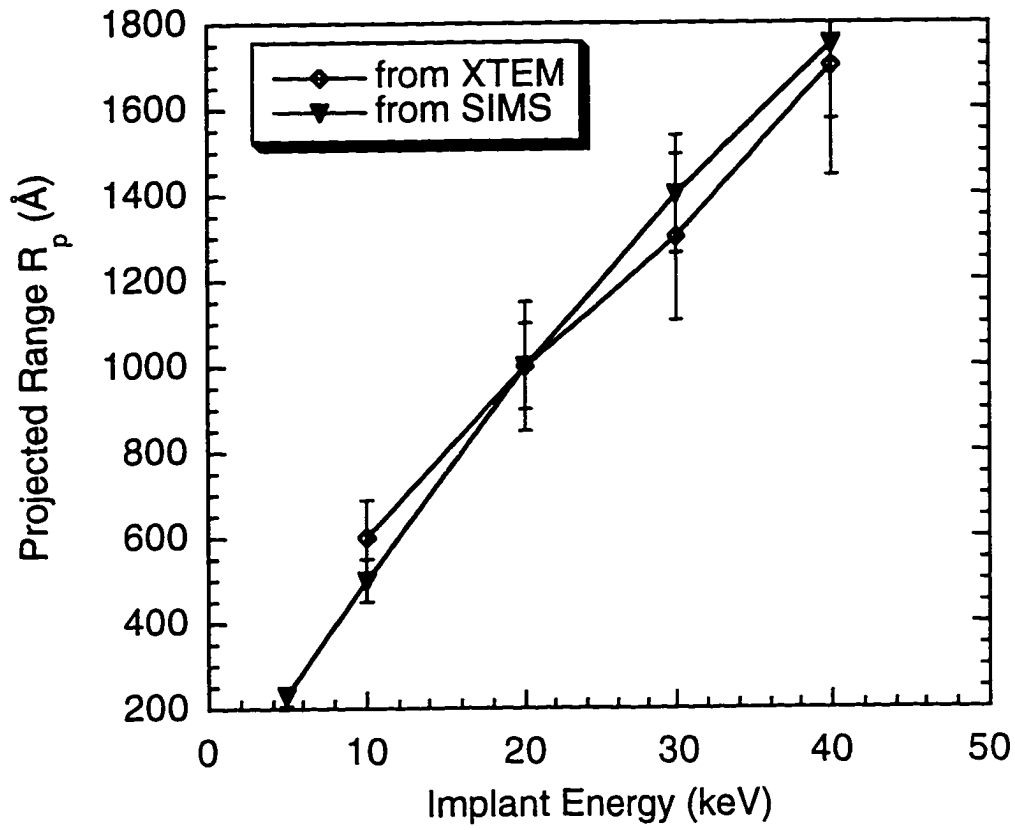


Figure 2.4. Projected range  $R_p$  of 5keV to 40keV  $B^+$  implanted Si, determined from XTEM micrographs and SIMS profiles.

CHAPTER 3  
EFFECT OF ANNEALING ON DEFECT EVOLUTION AND TRANSIENT  
ENHANCED DIFFUSION

3.1 Overview

Due to the limitation that TED imposes on the minimum device dimensions, it has been the subject of considerable studies for many years, yet its mechanism is still under debate. TED has been attributed to the excess point defects introduced by the implantation process. The magnitude of TED is related to the implantation conditions, the annealing conditions and the surface and bulk recombination effects. Recently, Stolck et al.<sup>113</sup> have suggested that TED occurs by the emission of silicon self-interstitials from rod-like {311} defects during annealing. The activation energy ( $3.6 \pm 0.1$  eV) for the {311} defect dissolution process relates closely with that of TED (3.5 eV). Later, Zhang et al.<sup>114</sup> reported that they observed TED in B<sup>+</sup> implanted samples without {311} defects and they attributed the interstitial source of TED to submicroscopic clusters. More recently, Cowern et al.<sup>123</sup> studied the role of carbon and boron clusters on the diffusion process. The number of self-interstitials trapped per clustered impurity atom is about 1.15 for carbon and about 1 for boron. This provided further evidence to the

possibility that there was more than one storage mechanism for excess interstitials that contribute to TED.

The purpose of this section is to discuss the effect of annealing on defect behavior and TED in order to investigate the correlation between the two.

### 3.2 Effect of Annealing on Defect Behavior

#### 3.2.1 Experimental Procedure

In order to study the dissolution kinetics of {311} defects from B<sup>+</sup> implantation without the complication of stable loop formation, we picked one sample (20 keV  $2 \times 10^{14} \text{ cm}^{-2}$ ) from the implant matrix discussed in Chapter 2 (refer to section 2.2). Subsequent furnace anneals were performed in a nitrogen ambient using fast pushes and pulls. The annealing temperatures and times were chosen as 650°C for 2 hr, 6 hr, 14 hr, 24 hr, 36 hr, 48 hr; 700°C for 30 min, 1 hr, 2 hr, 4 hr, 8 hr; 750°C for 5 min, 20 min, 30 min, 1 hr, 1.5 hr and 800°C for 3 min, 5 min, 8 min, 10 min, 13 min. PTEM micrographs were taken under weak beam dark field imaging condition using a g220 reflection. The density and length of {311} rod-like defects were measured directly from the TEM micrographs. The areal interstitial density bound by {311} defects after each anneal was calculated by multiplying the defect length by the density of interstitials per unit length. The time constant for the interstitial decay process at each temperature was plotted in an Arrhenius graph as a

function of the reciprocal of temperature to obtain the activation energy for the {311} defect dissolution process.

### 3.2.2 Defect Evolution: Microstructure, Interstitial Density and the Activation Energy of Interstitial Decay

Figure 3.1 (a)~(d) shows the PTEM micrographs of the sample after anneals at 650°C, 700°C, 750°C and 800°C for various times. The formation and coarsening/dissolution processes of {311} defects are faster at higher temperatures. After 2 hr at 650°C, these defects are not fully formed yet. The defects in their initial stages exhibit a "black dot" contrast. After 14 hr, {311} defects start to form. However, Ostwald ripening along with the dissolution process is so slow at this low temperature that the number of the defects is relatively large and their size is relatively small even after 48 hr of annealing. If the annealing temperature is increased to 750°C, {311} defects are observed after only 5 min and the dissolution process becomes more rapid. At 800°C, {311} defects almost dissolve completely after 13 min of annealing.

We have measured the net interstitials trapped in {311} defects from the PTEM micrographs after each anneal. Figure 3.2 shows the {311} defect dissolution process at each temperature. As we can see, the dissolution process shows an exponential dependence on annealing time. The dots in Fig. 3.2 are the actual data points and the lines are exponential fitting curves of the form

$$Si_i(t) = Si_i(0) \exp\left(-\frac{t}{\tau}\right) \quad (3.1)$$

where  $\tau$  is defined as the characteristic time constant of the decay. Although the decay process is strongly dependent on annealing temperature, the initial density of interstitials at all four temperatures is very close to the same value of  $3\text{--}4 \times 10^{13} \text{ cm}^{-2}$ , which is only 15–20% of the implant dose of  $2 \times 10^{14} \text{ cm}^{-2}$ . According to the "plus one" model,<sup>124</sup> the initial density of interstitials should closely mimic the implant dose, because each implanted ion is supposed to give rise to one excess interstitial during annealing. This model assumes that the implant ion induces a series of Frenkel pair formation and then comes to rest in the lattice at an interstitial site. Subsequent annealing results in annihilation of all vacancy-interstitial pairs with just the one interstitial remaining. This theory is proved to be reasonable by the study of Si implanted silicon of Listebarger et al.<sup>105</sup> and valid to a remarkable degree by the study of Eaglesham et al.<sup>125</sup>. Listebarger et al. used dislocation loops as point defect detectors to measure the flux of interstitials introduced by a 30keV B<sup>+</sup> implant to doses of  $7 \times 10^{13} \text{ cm}^{-2}$ ,  $1 \times 10^{14} \text{ cm}^{-2}$  and  $2 \times 10^{14} \text{ cm}^{-2}$ . The loops layer was formed by 100 keV Ge<sup>+</sup> implant to a dose of  $1 \times 10^{15} \text{ cm}^{-2}$  followed by an anneal at 550°C for 16 hr to regrow the amorphous surface and another anneal at 800°C for 30 min to coarsen the loops. They reported that the net flux of interstitials measured using the loop detectors is very

similar to the dose for each B<sup>+</sup> implant. Eaglesham et al. measured the density of interstitials trapped in {311} defects in 40 keV Si implanted silicon to a dose of  $5 \times 10^{13} \text{ cm}^{-2}$ . The interstitial density versus dose plot shows a slope of 1.5, indicating slightly more than one interstitial per implanted ion. However, in our B<sup>+</sup> implanted silicon study, the observed interstitials only account for approximately one tenth of the dose. We therefore believe that there is another type of defects, i.e., boron interstitial complexes, which trap the missing interstitials. These complexes are sub-microscopic and are not resolvable in the TEM. There appear to be more than one form of boron interstitial complexes. From our low energy low dose implants (as will be discussed later), we observed as did Zhang et al.<sup>114</sup> that there is a significant fraction of the implant profile peak that is immobile. This could be explained by the formation of B-B-interstitial clusters. A second portion of the profile is mobile and may simply be B-interstitial pairs as suggested by Cowern.<sup>123</sup> Both of these non-visible defects could help account for the "missing" interstitials in the {311} defects.

An Arrhenius plot of the characteristic rate constant  $k=1/\tau$  of {311} defect dissolution process as a function of  $1/T$  is shown in Fig. 3.3. This temperature dependence shows an activation energy of 3.8 eV. Along with our results, Fig. 3.3 also presents the temperature dependence of {311} defect dissolution from the study of Stolk et al.<sup>113</sup> of Si<sup>+</sup> implanted

silicon. It is interesting to notice that our activation energy is in close agreement with theirs of  $3.6 \pm 0.1$  eV, yet there is a y-axis shift of the two curves, i.e., the {311} defects in our sample are more stable. The similar activation energies implies the process of dissociation of an interstitial from {311} defects is the same, independent of the implant species. The reasons for the change in stability could be: (1) The dose for our implant ( $2 \times 10^{14} \text{ cm}^{-2}$ ) is much higher than what they used ( $5 \times 10^{13} \text{ cm}^{-2}$ ) and thus there are more interstitials in our sample to stabilize {311} defects. (2) The dissolution of boron interstitial clusters in our sample during the anneal induces a higher concentration of interstitials in the background environment and again delays the dissolution of {311} defects.

### 3.2.2 Defect Evolution: Density, Size and Distribution

Quantitative results that one can obtain from the PTEM micrographs include the {311} defect density, the average defect length and the defect distribution after annealing.

Figure 3.4 shows the {311} defect density as a function of annealing time for each temperature. The defect density decreases dramatically with increasing annealing time. Although the rate is just slightly higher for higher temperature, it takes much longer for a lower temperature to reach a particular density. For example, the density drops to  $10^9 \text{ cm}^{-2}$  after about 10 min at  $800^\circ\text{C}$ , but it takes more than 10 hr at  $700^\circ\text{C}$ . This rapid decrease in the number of



defects explains the decay of interstitials trapped in  $\{311\}$ s even when the average defect size increases.

The average  $\{311\}$  defect size is shown in Fig. 3.5 as a function of annealing time for each temperature. The width change of these defects have been found to be very small during the anneal by high resolution TEM studies conducted by Eaglesham et al.<sup>125</sup>, so that the size change is represented by the change of the length. As can be seen from Fig. 3.5, the average defect size increases initially with annealing time and then starts to decrease at some point during the dissolution process. This breaking point can be seen for anneals at 700°C and 750°C but not for anneals at 650°C or 800°C. We believe this final drop of defect size indicates a pure dissolution stage which should be observed as well at 650°C and 800°C if the anneals are long enough. Again, to reach a particular defect size, it takes longer for lower temperatures. For example, for 800°C anneal, the defect size reaches 400 Å after about 3min, while at 700°C, it takes about 1.5 hr.

To further illustrate the  $\{311\}$  defect evolution process, the defect distributions after each anneal at each temperature are shown in Fig. 3.6 (a)~(d). The distribution moves to a larger size with increasing time at each temperature and the defect density  $N(l)$  at every size  $l$  shifts to a lower value. This movement is faster for a higher temperature. During the anneal, the interstitial concentration in the vicinity of large defects is lower than

that in the vicinity of small defects. As a result, interstitials are emitted from the small defects and move toward the large ones. The large defects then absorb these interstitials and grow at the expense of the shrinkage of the small defects. This is the so-called Ostwald ripening process. Meanwhile, since the interstitial concentration in the area surrounding a defect is higher than that in the background environment, interstitials tend to leave the defect and move into the bulk. As a result, defect shrink and system approaches equilibrium condition. This is the defect dissolution process. During the Ostwald ripening process, defect density is expected to decrease, defect size is expected to increase and the total number of interstitials trapped in the defects is expected to remain as a constant. On the other hand, during the dissolution process, all three quantities are expected to decrease. In our experiment, we observed a decreasing interstitial concentration, an increasing defect size and a decreasing defect density with increasing annealing time. This indicates an Ostwald ripening process along with dissolution process. The distribution plots for longer time anneals (e.g., 800°C 13 min) show considerable scatter rather than a regular distribution because the total number of defects is small and the counting results are not as representative as those of the short time anneals.

The driving force for the Ostwald ripening process is the self-energy difference between the defects with different

sizes. Self-energy of the  $\{311\}$  defect was calculated by Parisini and Bourret<sup>76</sup> by approximating the rod-like shape with a dipole of edge dislocations of the same sense and opposite Burgers vector. It is given by

$$W = \frac{\mu b^2}{2\pi(1-\nu)} \left[ \ln\left(\frac{\eta}{2\rho}\right) + \cos^2 \theta \right] L \quad (3.2)$$

where  $\mu$  is the shear modulus,  $b$  the Burgers vector,  $\nu$  the Poisson's ratio,  $\eta$  the distance between the two edge dislocations (i.e., the width of the  $\{311\}$  defect),  $\rho=b/8$  the cut-off distance,  $\theta$  the angle between the Burgers vector and the normal to the plane containing the  $\{311\}$  defect and  $L$  the length of the  $\{311\}$  defect. To obtain the energy per interstitial, one can divide the previous expression by the number of interstitials  $N$  trapped in a  $\{311\}$  defect with a length of  $L$ .  $N$  is given by

$$N = \rho_l L \eta \quad (3.3)$$

where  $\rho_l$  is the atomic density on the  $\{311\}$  plane. The energy of one interstitial is thus given by

$$W_I = \frac{\mu b^2}{2\pi(1-\nu)} \left[ \ln\left(\frac{\eta}{2\rho}\right) + \cos^2 \theta \right] \frac{1}{\rho_l \eta} \quad (3.4)$$

As we can see from eq.(3.4),  $W_I$  is independent of the length  $L$  but is dependent on the width  $\eta$ . Since  $\ln(\eta/\rho)$  decays slower than  $\eta$ ,  $W_I$  decreases when  $\eta$  increases. We thus speculate that the width of a shorter  $\{311\}$  defect is smaller than that of a longer one. As a result, the self-energy of an interstitial trapped in a shorter  $\{311\}$  defect is higher than that in a longer one. Interstitials would thus flow from shorter rods to longer ones. This explains the Ostwald ripening process.

In fact we have observed the  $\{311\}$  defect width change under the TEM. PTEM pictures were taken on the  $\langle 311 \rangle$  zone with  $g=220$ . The following trend was found: the width is about 20 Å when the length  $L$  is 200~400 Å. It increases to about 40 Å when  $L$  is around 1000 Å, to about 80 Å when the  $L$  is around 1200~1400 Å, then to about 100 Å for  $L=1600\sim 1800$  Å and about 120 Å when  $L\sim 3000$  Å. These measurements were performed on samples annealed at 750°C for 5 min, 15 min and 1 hr. The error range might be large because of the narrow width of these defects. However, the width change with length can be used to account for the interstitial flow during the coarsening process. It should be mentioned that in this study this width change is ignored when the areal density of interstitials trapped in  $\{311\}$  defects was measured from the length of  $\{311\}$  defects and the interstitial density per unit length. In fact it is almost impossible to measure both the width and the length of every defect to obtain a more accurate result.

In summary, in this section of Chapter 3 we have discussed the  $\{311\}$  defect evolution process during anneals at 650°C to 800°C for various times. The areal density of interstitials bound by  $\{311\}$  defects decays exponentially with annealing time with a characteristic time constant which is larger at lower temperatures. This dependence has an activation energy of 3.8 eV. The number of interstitial trapped in  $\{311\}$  defects is only 15~20% of the implant dose, implying the presence of boron interstitial complexes,

including both immobile clusters and mobile boron interstitial pairs. The defect density decreases with increasing annealing time and the average defect size increases initially and then decreases with time. The distribution of {311} defects shows a shift of the average defect size to a larger value and a decrease of density at each size. The defect evolution shows the characteristics of Ostwald ripening process accompanied by a defect dissolution process.

### 3.3 Effect of Annealing on Transient Enhanced Diffusion

#### 3.3.1 Experimental Procedure

The same wafer ( $20 \text{ keV } 2 \times 10^{14} \text{ cm}^{-2} \text{ B}^+$  implant) which we used to study the effect of annealing on defect evolution was also used for diffusion study. Subsequent anneals were again performed in a nitrogen ambient at  $650^\circ\text{C}$ ,  $700^\circ\text{C}$ ,  $750^\circ\text{C}$  and  $800^\circ\text{C}$  for various times. SIMS analysis was performed on the CAMECA IMS4f system.  $\text{B}^+$  ions were monitored under  $\text{O}_2^+$  bombardment at an impact angle of about  $42^\circ$ . Secondary ions were collected from the center 12% of a  $150 \mu\text{m} \times 150 \mu\text{m}$  rastered area to avoid edge effects. Atomic concentrations were calculated using a relative sensitivity factor (RSF) for boron determined from an implanted standard. Stylus profilometry was used to calibrate the depth scale for the profiles. The dopant profiles were then imported into

Florida Object Oriented Process Simulator (FLOOPS) and the diffusivity enhancement was extracted for each anneal.

### 3.3.2 Dopant Diffusion during Annealing

#### 3.3.2.1 Static Peak at High Concentration

As an example of the dopant diffusion behavior during annealing, Fig.3.7 (a)~(d) shows the boron profiles obtained through SIMS after anneals at 650°C for 2 hr, 14 hr, 24 hr, at 700°C for 30 min, 2 hr and 4 hr, at 750°C for 20 min, 1 hr, 2 hr and at 800°C for 3 min, 30 min and 1 hr. We can see that a critical concentration exists under every annealing condition, separating the low concentration tail region where transient diffusion occurs, from the high concentration peak region where the profile is relatively immobile. The breaking point between the mobile and immobile region ( $C_{enh}$ ) moves to higher concentration when annealing temperature increases. It is about  $2.5 \times 10^{18} \text{ cm}^{-3}$  at 700°C and moves up to about  $7 \times 10^{18} \text{ cm}^{-3}$  at 800°C. Figure 3.8 shows  $C_{enh}$  as a function of inverse temperature for our study and some of the previous studies. Also plotted in Fig. 3.8 are the solid solubility for boron in silicon  $C_s$  and the intrinsic carrier concentration  $n_i$ .

There are several groups which have reported the peak clustering behavior of an implant profile. Michel et al.<sup>126</sup> studied 60 keV  $2 \times 10^{14} \text{ cm}^{-2}$  B<sup>+</sup> implanted silicon. Over an annealing temperature range of 800°C~950°C, their measurements show that both the maximum concentration of the

displaced boron and the electrical activity are related to the intrinsic carrier concentration. Later, Fair<sup>127</sup> has extended the correlation between  $C_{enh}$  and  $n_i$  to the temperature range of 600°C~800°C. It was observed that when  $T > 850^\circ\text{C}$ ,  $C_{enh}$  approaches B solid solubility  $C_s$ . A model was proposed by Fair, suggesting that the existence of  $C_{enh}$  is due to the Fermi level and the charge state of the defect affecting diffusion. For boron diffusion the location of the donor level of self-interstitials  $I^+$  in the energy gap causes  $C_{enh}$  to equal  $n_i$  for  $T < 800^\circ\text{C}$ . Under this condition, a significant fraction of the excess interstitials are in the neutral charge state  $I^X$ . For doping under  $C_{enh} \sim n_i$ , diffusion is dominated by  $I^X$ . Since  $D_{I^X}/D_{I^+}$  is 10~100, more enhanced diffusion occurs at  $C < C_{enh}$ . For  $T > 850^\circ\text{C}$ , the  $E_{I^+}$  level is sufficiently above  $E_F$  and the majority of injected interstitial exist in  $I^+$  state. Then the thermally assisted, concentration dependent diffusion via  $I^+$  becomes dominant and  $C_{enh}$  is limited by B solid solubility  $C_s$ . The study of Cowern et al.<sup>128</sup> on 25 keV  $2 \times 10^{14} \text{ cm}^{-2}$   $B^+$  implants agreed with Fair's results.  $C_{enh}$  lies within a factor of 2 of  $n_i$  in a temperature range of 550°C~900°C. A relative insensitivity of  $C_{enh}$  to the implant energy and dose was suggested by all three groups. As shown in Fig. 3.8, our data of 20 keV  $2 \times 10^{14} \text{ cm}^{-2}$   $B^+$  implants also agree with those of the above groups to a reasonable degree within 650°C~800°C. However, the data of Zhang et al. for 4 keV  $1 \times 10^{14} \text{ cm}^{-2}$   $B^+$  implants<sup>114</sup> do not match the intrinsic carrier concentration but are

rather higher than that, especially at higher temperatures ( $T > 700^\circ\text{C}$ ). This mismatch can not be explained by Fair's model. We therefore speculate that the correlation between  $C_{\text{enh}}$  and  $n_i$  might just be a coincidence. A better explanation is that clustering effect induces an immobile fraction of the profile. As for the kinetics of peak clustering, Cowern et al.<sup>128</sup> suggested the following reactions:



where the intermediate defect configurations (IDCs), which was originally proposed by Tan,<sup>56</sup> might include boron pairs or clusters, rodlike {311} defects, certain stacking faults, etc. Silicon interstitials (I) pair or kick out substitutional boron atoms ( $B_S$ ) to form migrating interstitial boron atoms ( $B_I$ ). During the transient phase, the concentration of  $B_I$  is high enough to allow homogeneous nucleation of boron containing defects. The defect formation is most favorable near the peak region where the B concentration is highest. Stolk et al.<sup>113</sup> proposed another clustering reaction given by



where  $B_C$  refers to immobile clusters containing  $m+1$  boron atoms, and  $n$  is the number of interstitials injected upon clustering to allow stress relief ( $n < m$ ). While eq. (3.5) sustains the enhanced diffusion of  $B_S$ , eqs. (3.6) and (3.7) lead to cluster formation and reduce the amount of  $B_S$



available for diffusion at high B and I concentrations. Comparing eq.(3.6) and (3.7) will raise the question of whether the immobile B-I complexes contain  $B_S-B_I-I$  clusters or  $B_S-B_S-I$  clusters. Diaz de la Rubia et al. (private communication) have shown through ab initio calculation that the  $B_I-B_S$  pair has a positive binding energy of about 1.8 eV. This  $B_I-B_S$  pair also traps silicon interstitial. It is immobile and electrically inactive. The  $B_S-B_S$  pair, on the other hand, is found to be energetically unfavorable with a binding energy of -1.7 eV and electrically active. According to this calculation, the immobile, electrically inactive implant profile peak might be consisted of the  $B_I-B_S-I$  clusters.

It should be mentioned that rod-like  $\{311\}$  defects also locate in a depth corresponding to the profile peak region, so do the sub-amorphization dislocation loops. However, the  $\{311\}$  defects<sup>113</sup> dissolve on a time scale comparable to the transient diffusion (e.g. <30 min at 800°C), while the static B-I clusters dissolve much slower (e.g. > 4 hr at 800°C<sup>128</sup>).  $\{311\}$  defects and unstable loops contribute to transient enhanced diffusion before it saturates. When the clusters and stable loops finally break up, there will be a second burst of enhanced diffusion. The slight increase of  $C_{enh}$  with increasing temperature is due to a decreasing interstitial supersaturation level which results in less clustering or even breaks up some existing clusters. There is no experimental evidence on how many interstitials are

trapped in one  $B_S-B_I$  cluster. In our 20 keV  $2 \times 10^{14} \text{ cm}^{-2}$   $B^+$  implant, after an anneal at  $750^\circ\text{C}$  for 2 hr,  $\{311\}$  defects almost dissolved completely. The density of activated boron atoms is estimated to be  $< 7 \times 10^{13} \text{ cm}^{-2}$  by integrating the non-clustered region of the implant profile. Assuming a valid "plus 1" model and assuming that one activated B atom pairs with one interstitial, the number of interstitials trapped in the B-I clusters must exceed  $1.3 \times 10^{14} \text{ cm}^{-2}$ . Thus we speculate that one  $B_S-B_I$  cluster might trap more than two interstitials.

The annealing time scale we used in this study is much shorter than that is needed to break up the clusters and stable loops, so our focus is on TED at low concentration after relatively short anneals.

#### 3.3.2.2 Broadened Tail at Low Concentration

From Fig. 3.7 we notice that significant diffusion occurred in the tail region ( $C < C_{enh}$ ) of the profiles at all four temperatures. This is caused by the pairing of excess interstitials induced by ion implantation with dopant atoms. The boron profile displacement at this region changes with the temperature. A 4 hr anneal at  $700^\circ\text{C}$  resulted in a displacement of about 2200 Å at a concentration of  $1 \times 10^{16} \text{ atoms/cm}^3$  relative to the as-implanted profile, whereas a 1hr anneal at  $800^\circ\text{C}$  resulted in a displacement of about 1750 Å for the same concentration. As will be shown later, TED is complete after 1 hr at  $800^\circ\text{C}$  but is still continuing after

2 hr at 700°C. Lower temperature annealing causes more diffusion before the saturation point is reached.

The SIMS profiles of boron in the as-implanted and annealed samples were imported into FLOOPS and the enhancement of diffusivity  $\langle D_B \rangle / D_B^*$  after each anneal was obtained after the simulations. Here  $\langle D_B \rangle$  is the time-averaged boron diffusivity and  $D_B^*$  is the intrinsic equilibrium value.  $D_B^*$  has the form of

$$D_B^* = 0.757 \exp(-3.46 \text{ eV} / kT) \quad (3.8)$$

as a default value in FLOOPS, which was originally taken from Fair's review article<sup>129</sup>. This value is about  $1.03 \times 10^{-19} \text{ cm}^2/\text{sec}$ ,  $9.64 \times 10^{-19} \text{ cm}^2/\text{sec}$ ,  $7.22 \times 10^{-18} \text{ cm}^2/\text{sec}$  and  $4.48 \times 10^{-17} \text{ cm}^2/\text{sec}$  at 650°C, 700°C, 750°C and 800°C, respectively. Since the dopant profiles are not perfectly Gaussian, instead of choosing the whole profile, we chose a portion of the tail region (approximately 1600 Å–2600 Å) as the target profile during simulation. Figure 3.9 shows these simulation results of  $\langle D_B \rangle / D_B^*$  as a function of annealing time for each temperature. As we can see, the time-averaged diffusivity enhancement decreases with increasing annealing time. Since  $\langle D_B \rangle / D_B^*$  is proportional to the interstitial supersaturation level,  $\langle C_I \rangle / C_I^*$ , in the case of B diffusion, the decrease of  $\langle D_B \rangle / D_B^*$  represents a process during which the interstitial concentration returns to its equilibrium value. Here  $\langle C_I \rangle$  is the time-averaged interstitial concentration in the bulk, and  $C_I^*$  is the equilibrium value.  $C_I^*$  is smaller and  $\langle C_I \rangle / C_I^*$  is higher at lower temperatures

so that  $\langle D_B \rangle / D_B^*$  is higher. It requires longer time for the system to reach equilibrium at a lower temperature. However, the time point at which the equilibrium is reached cannot be read directly from the  $\langle D_B \rangle / D_B^*$  graph mainly because they are the time-averaged values. This time will be determined from the diffusion length vs. time plot as will be presented in the following section, from which we will derive the activation energy for the diffusion process.

### 3.3.3 The Activation Energy for the Diffusion Saturation Process

The diffusion length can be calculated as  $\sqrt{\langle D_B \rangle t}$  from the diffusivity enhancement, the intrinsic diffusivity  $D_B^*$  and the annealing time at each temperature. Figure 3.10 summarizes the results. The dots in Fig. 3.10 are the actual data points and the lines are the fitting lines in the form of  $a\sqrt{1-\exp(-t/\tau)}$ , where  $a$  and  $\tau$  are constants and  $t$  is the annealing time. This is obtained by assuming the instantaneous value of  $D_B$  is proportional to  $\exp(-t/\tau)$ , and the diffusion length  $L$  of boron is the square root of the time integration of  $D_B$ , i.e.,

$$D_B(t) \propto e^{-\frac{t}{\tau}} \quad (3.9)$$

$$\begin{aligned} L &= \sqrt{\langle D_B \rangle t} = \sqrt{\int_0^t D_B(t_1) dt_1} \\ &= \sqrt{\int_0^t e^{-\frac{t_1}{\tau}} dt_1} \propto \sqrt{(1 - e^{-\frac{t}{\tau}})} \end{aligned} \quad (3.10)$$

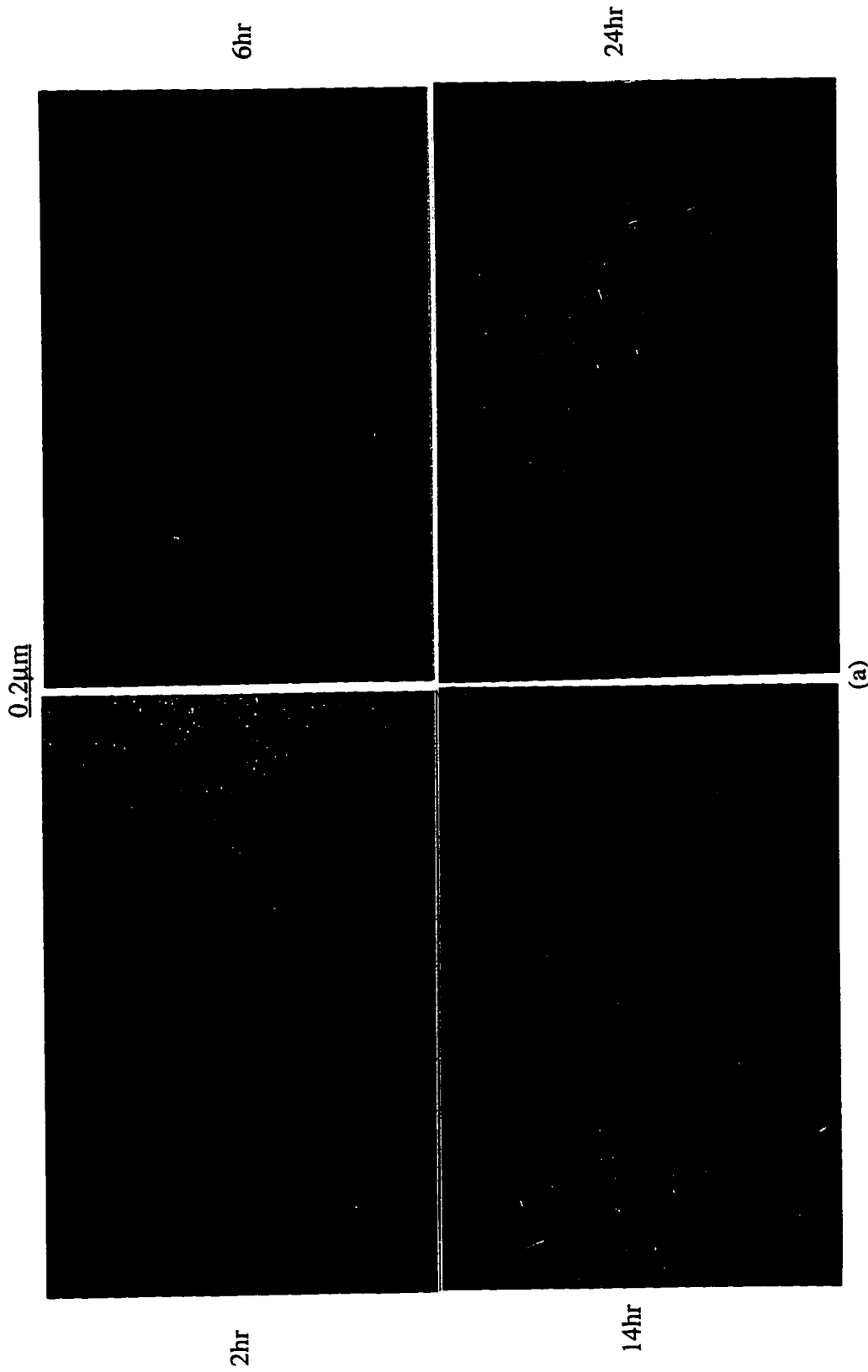
The diffusion length increases initially with time and then plateaus out. The time till the "knee" region, i.e., just before it plateaus out is  $2\tau$ . If we choose  $2\tau$  as the time

constant for the TED saturation process, from Fig. 3.10 we can see that this constant increases dramatically as annealing temperature decreases. It is about 4.5 hr at 650°C and decreases more than one order of magnitude to about 15min at 800°C.

The temperature dependence of the time constant for the TED saturation process is shown in Fig. 3.11. Such a dependence exhibits an activation energy of about 1.6eV. This value is smaller than the 3.1-3.7eV reported by Packan,<sup>130</sup> 3.5 eV reported by Stolk et al.<sup>113</sup> yet it is greater than the < 1 eV we calculated from the data of Zhang et al.<sup>114</sup> as shown together in Fig. 3.10. The difference between these experiments is that both Packan and Stolk et al. studied silicon self-implanted silicon. In these samples the interstitial source for TED is believed to be only {311} defects. Zhang et al. studied low energy (4 keV) boron implanted silicon where the energy and dose combination resulted in no extended defects observed by TEM. The source of interstitials driving TED in this case was claimed to be sub-microscopic clusters, which may be as simple as just mobile B-I pairs that diffuse until the pair breaks up. In our case, the samples were implanted with boron, but at a higher energy and dose so that not only {311} defects are present, B-I pairs might also exist. The activation energy of the TED saturation process reflects a complex process, including the release of interstitials from B-I pairs and {311} defects, the migration of interstitials through the

bulk, the surface recombination effect, impurity trapping, etc. Variation in the activation energy is thus not unexpected in these different systems. However, we still believe that in our case, not only {311} defects play a role in terms of releasing interstitials during annealing and thereby driving TED, boron interstitial pairs also play an important role.

In summary, 20 keV  $2 \times 10^{14} \text{ cm}^{-2}$  boron implanted silicon was studied for the purpose of identifying the possible sources of interstitials driving TED. The static peak region was presumably consisted of immobile  $B_I$ - $B_S$ -I clusters which breaks up in times much longer than normal TED. Boron TED in the tail region was measured through SIMS analysis and FLOOPS simulation. The duration of TED increases dramatically when the annealing temperature decreases. The activation energy for the TED saturation process is about 1.6 eV, higher than that in the sample presumably with only B-I pairs contributing to TED and lower than that in samples with only {311} defects. The interstitials driving TED in our sample are believed to come from both mobile boron interstitial pairs and {311} defects. The dissolution of {311} defects and B-I pairs may interact with each other and result in a single activation energy lying in between.



(a) Figure 3.1. Weak beam dark field (g220) PTEM micrographs of {311} defects in 20keV  $2 \times 10^{14} \text{ cm}^{-2}$   $B^+$  implanted Si after anneals at (a) 650°C, (b) 700°C, (c) 750°C and (d) 800°C for various times.

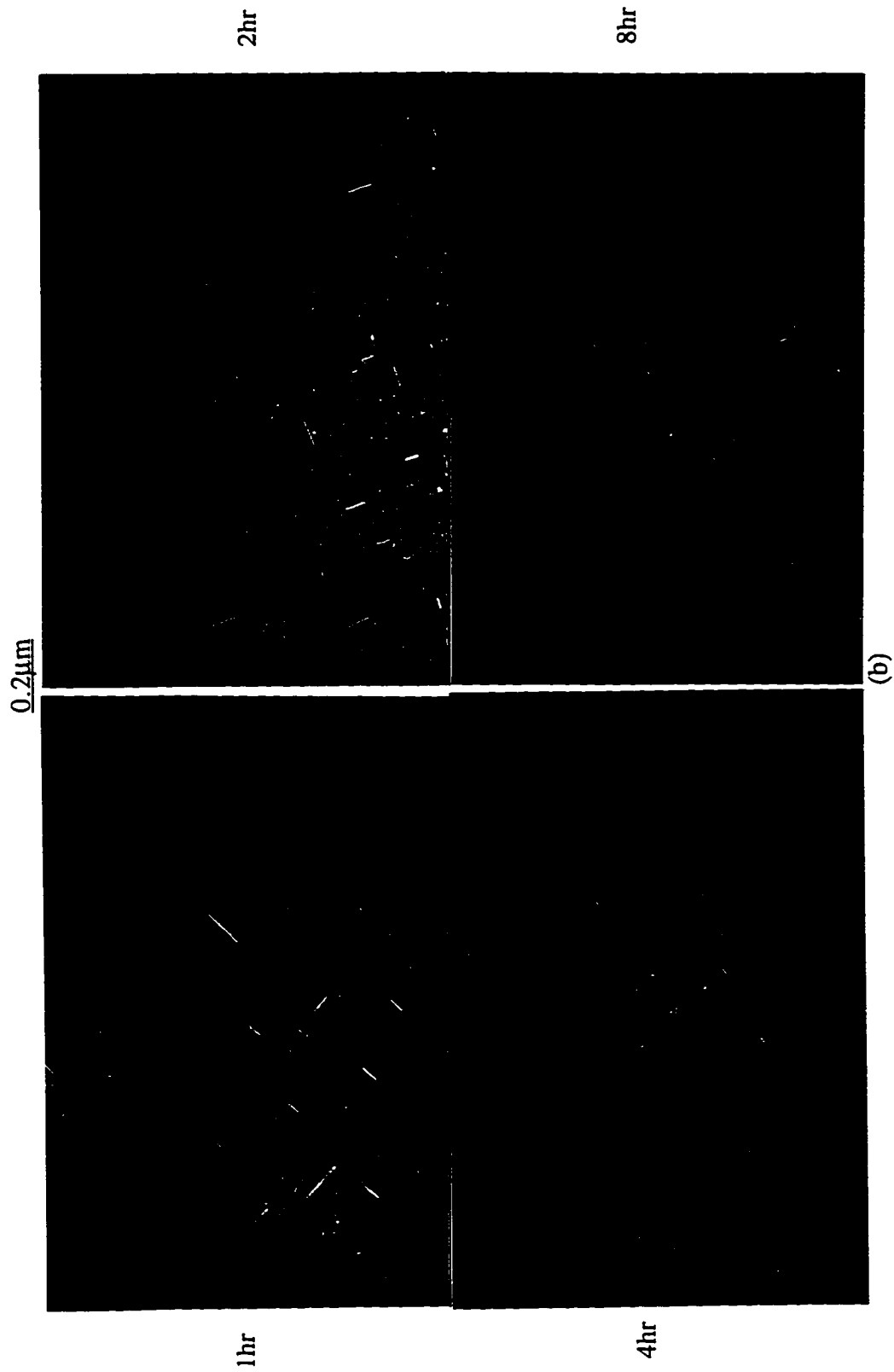


Figure 3.1. (Continued)



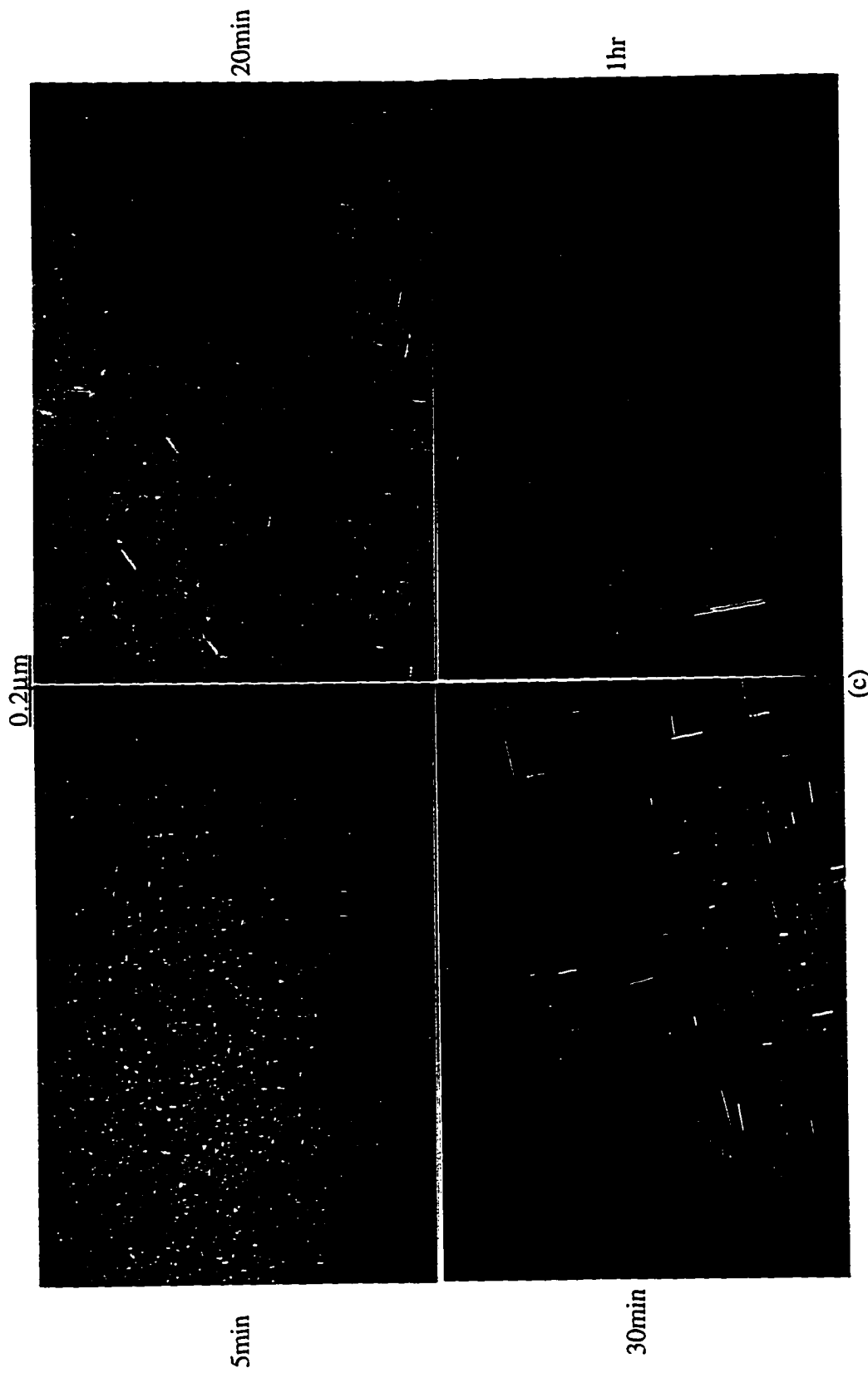


Figure 3.1. (Continued)

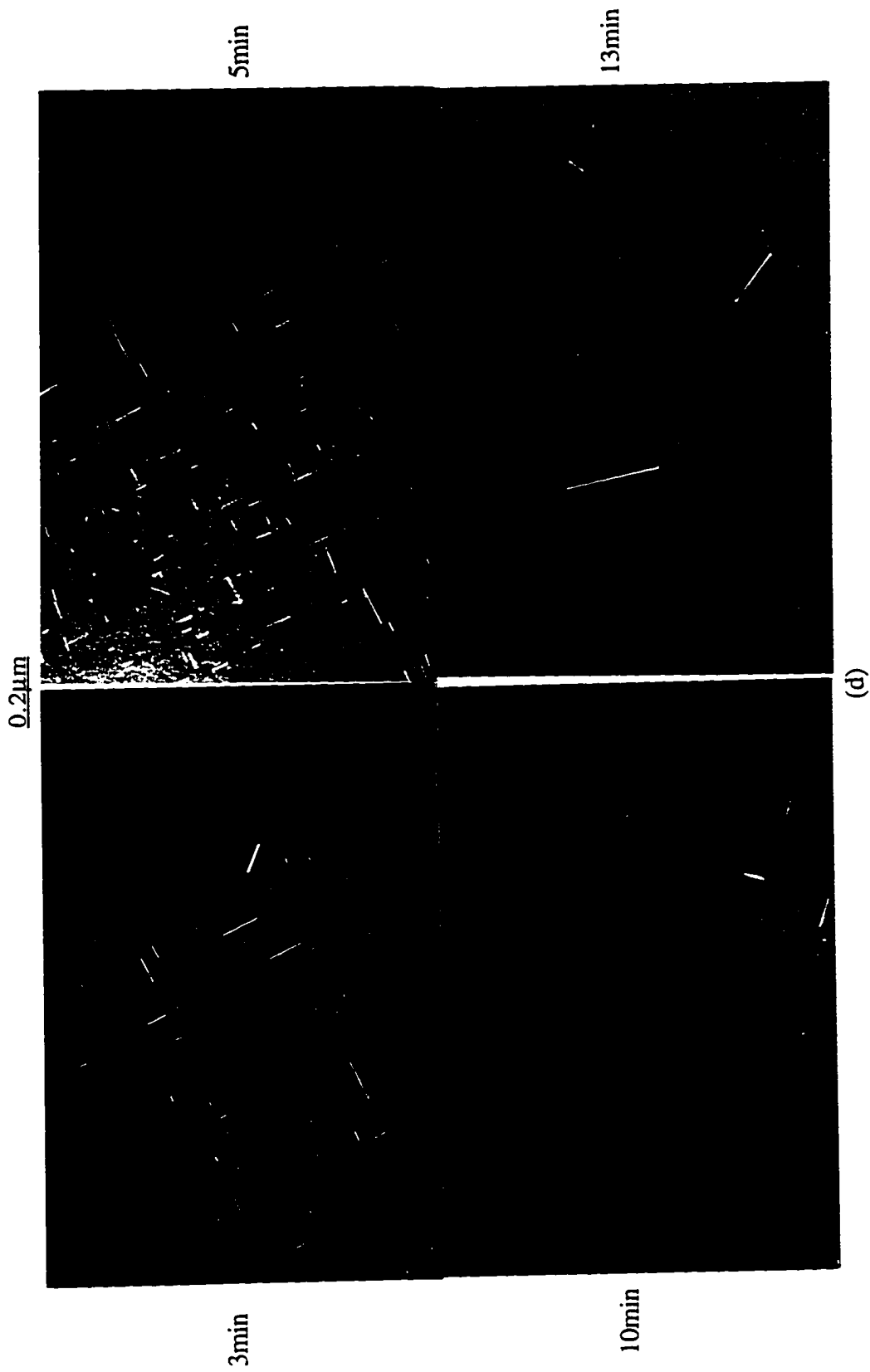


Figure 3.1. (Continued)

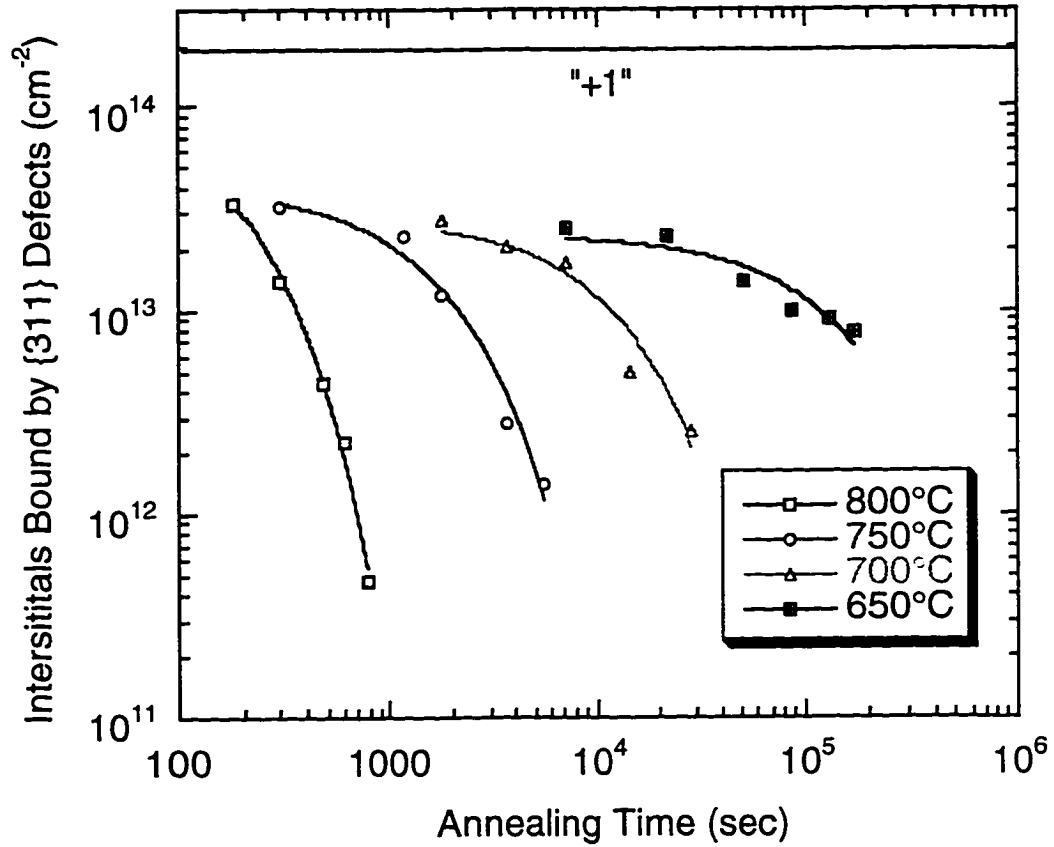


Figure 3.2. The exponential decay of interstitials trapped in {311} defects in 20keV B<sup>+</sup> implanted Si after anneals at 650°C to 800°C for various times.

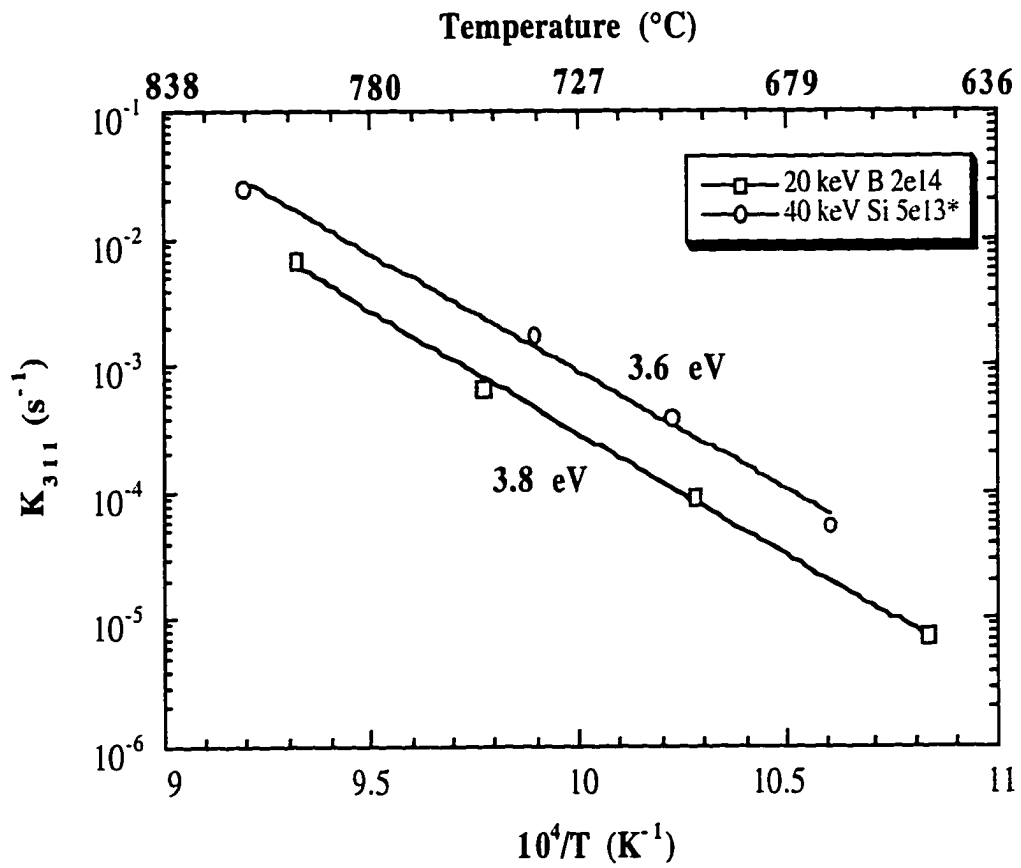


Figure 3.3. Rate of {311} dissolution process and the activation energy.

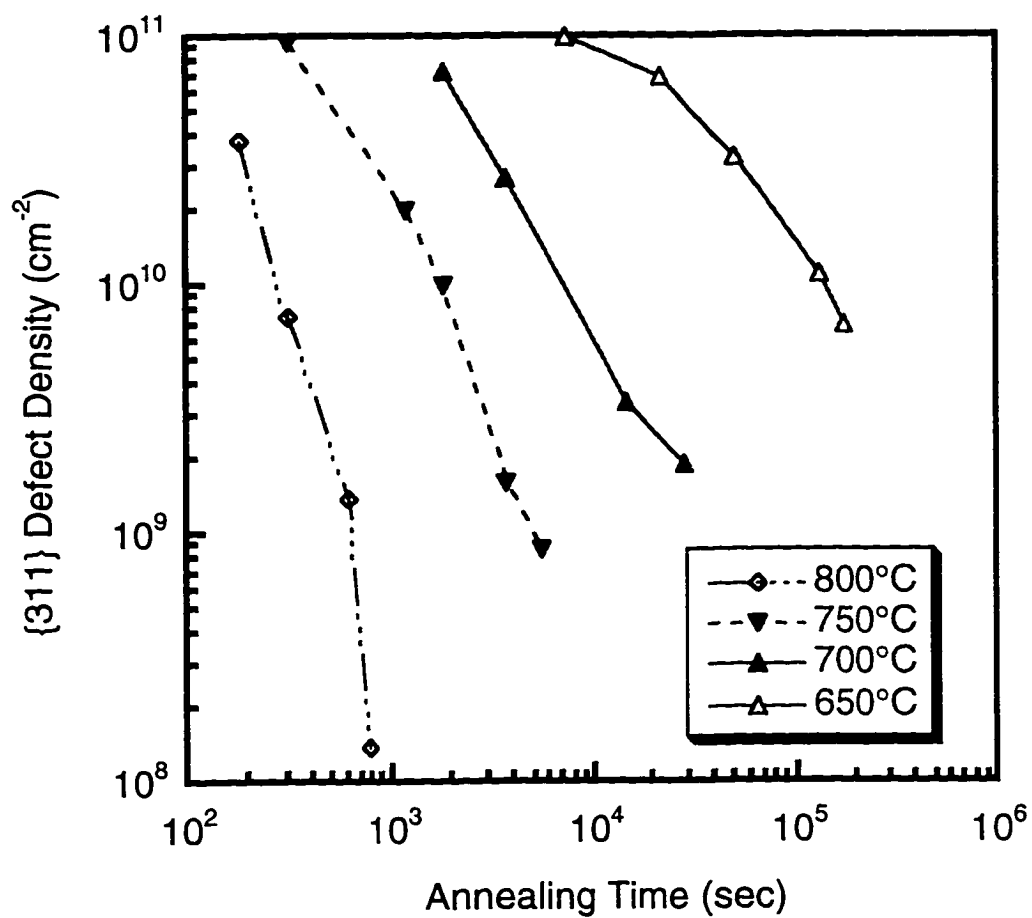


Figure 3.4. {311} defect density as a function of annealing time in 20keV B<sup>+</sup> implanted Si for different annealing conditions.

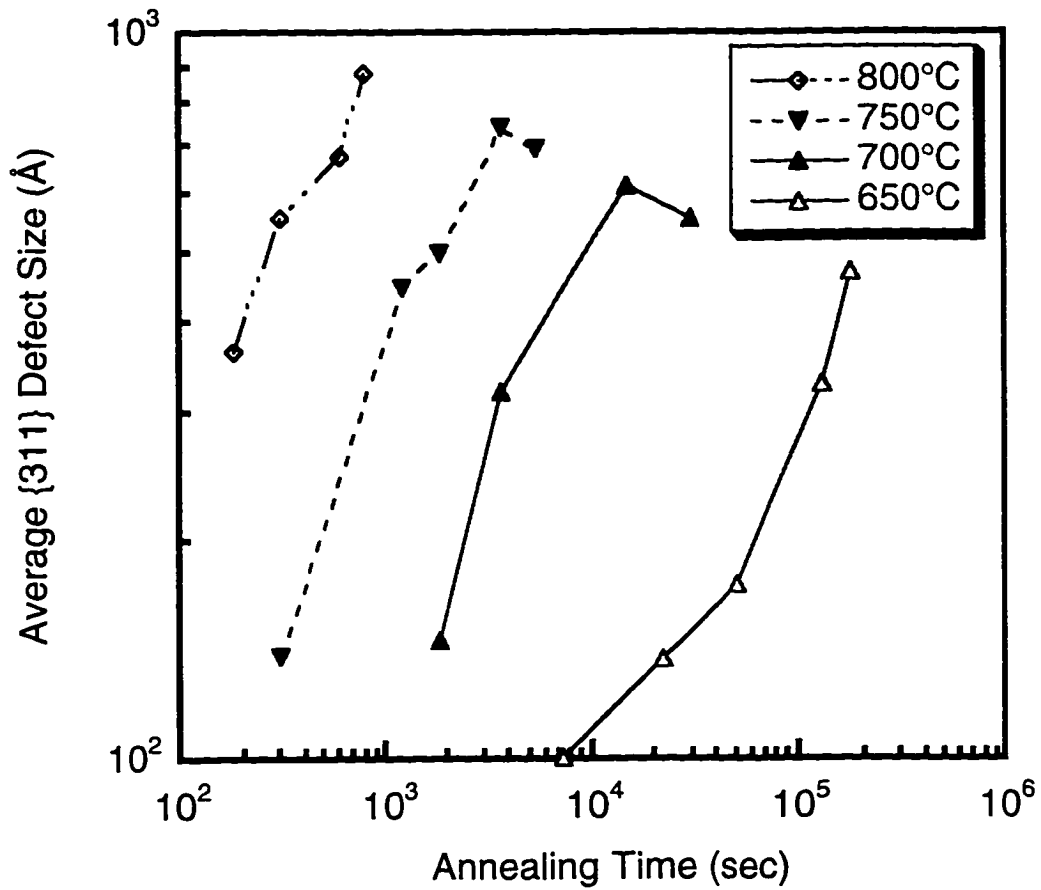
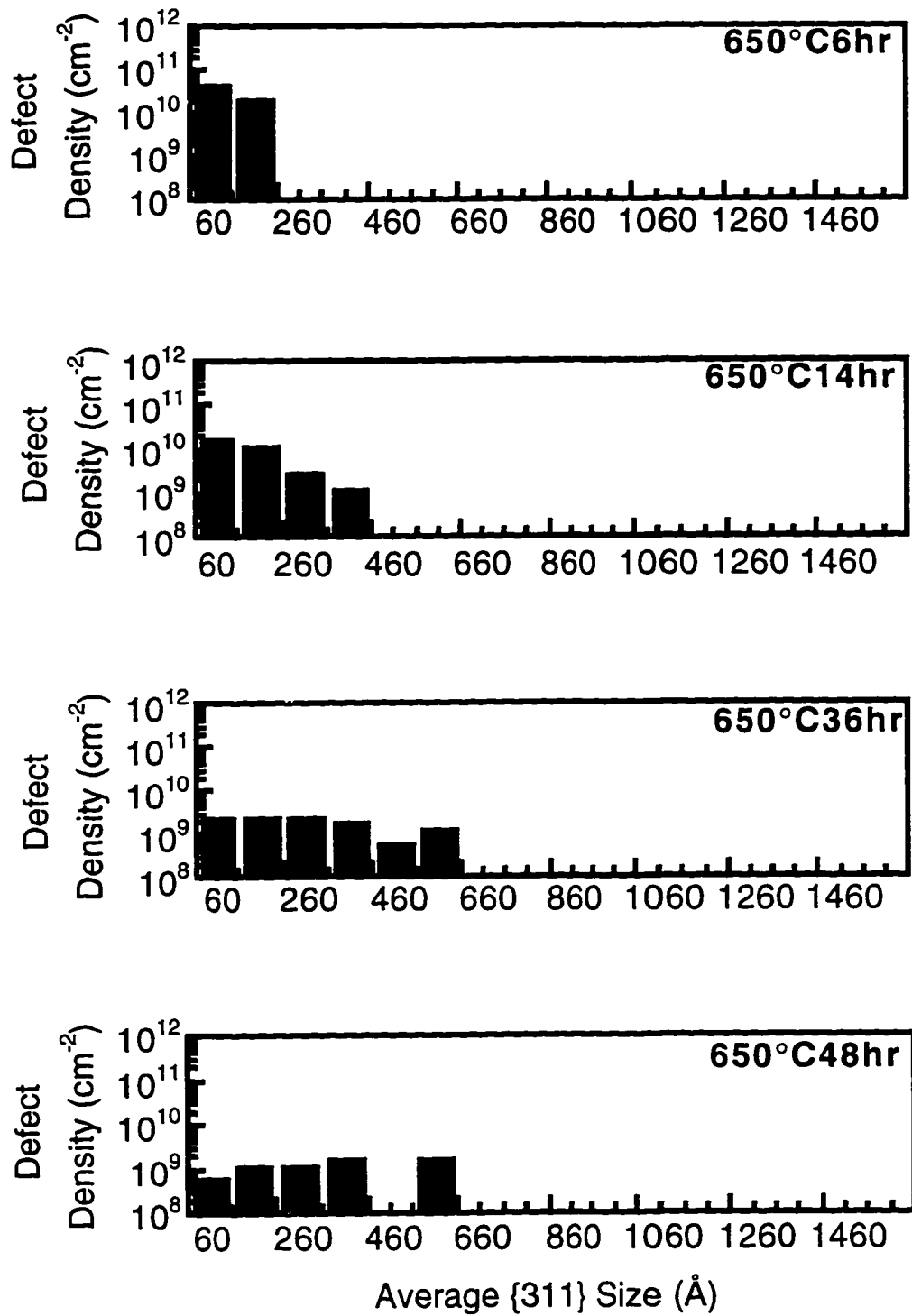
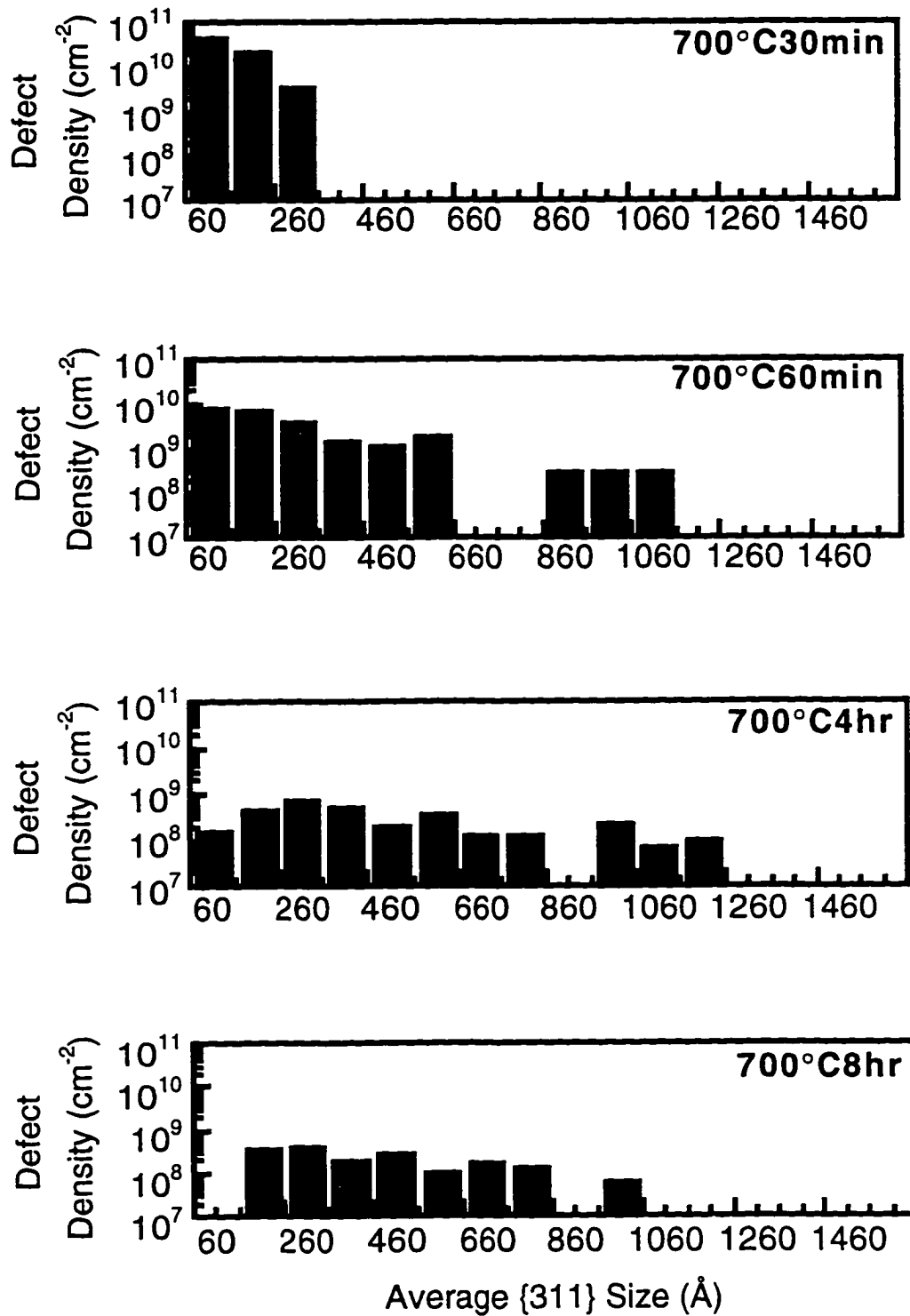


Figure 3.5. Average {311} defect size as a function of annealing time in 20keV B<sup>+</sup> implanted Si for different annealing conditions.



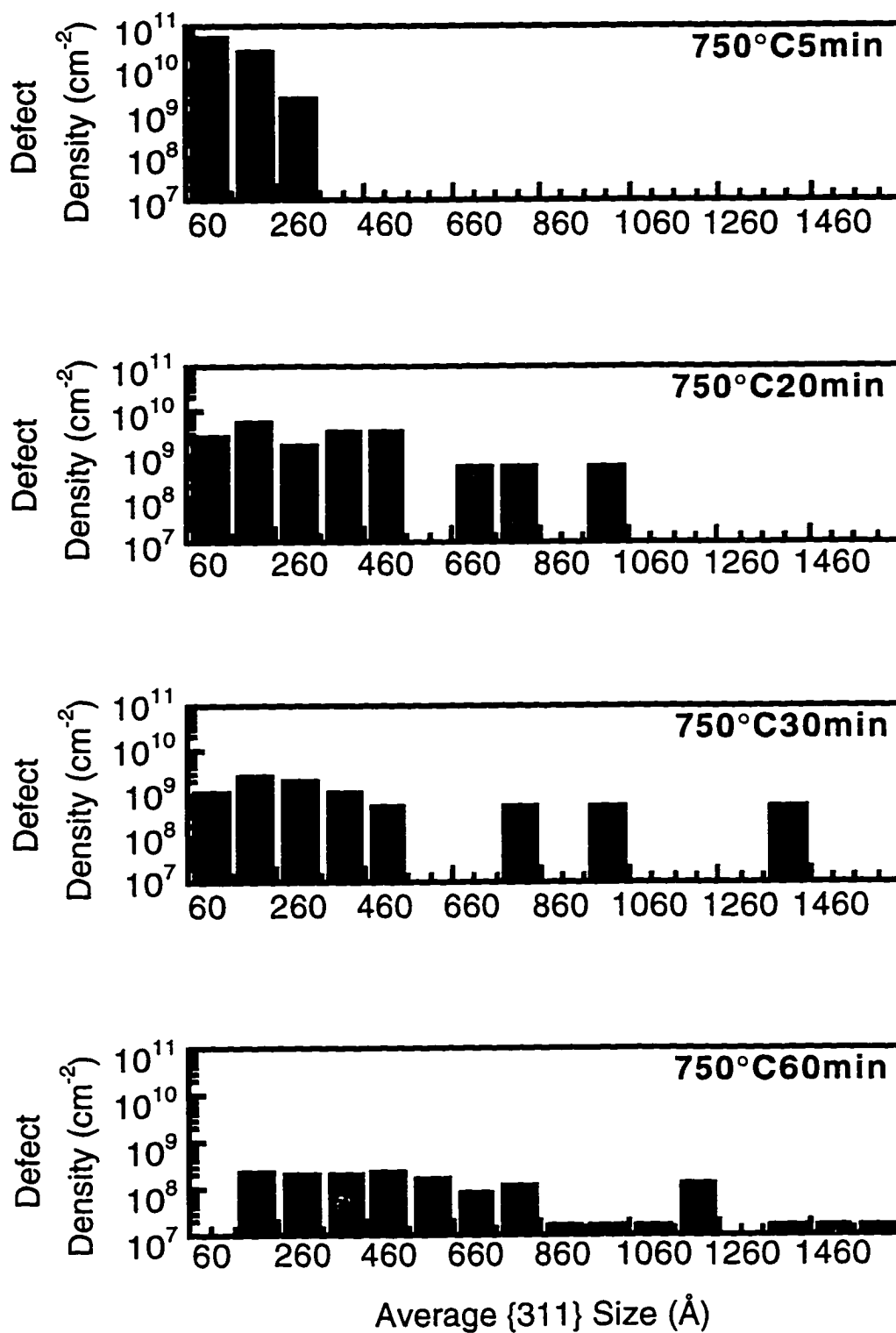
(a)

Figure 3.6. {311} defect size distribution during annealing at (a) 650°C, (b) 700°C, (c) 750°C and (d) 800°C.

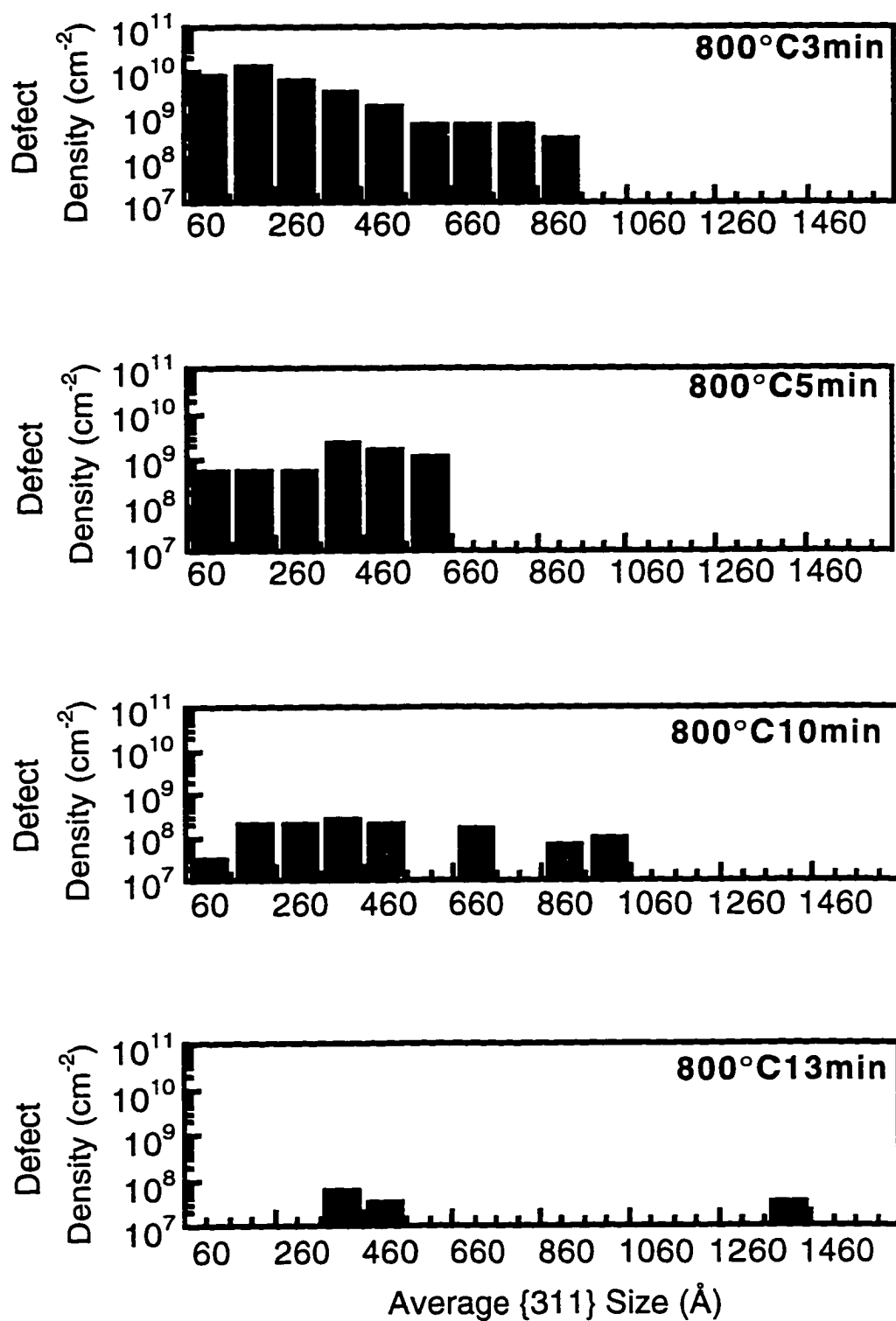


(b)  
Figure 3.6. (Continued)





(c)  
Figure 3.6. (Continued)



(d)  
Figure 3.6. (Continued)

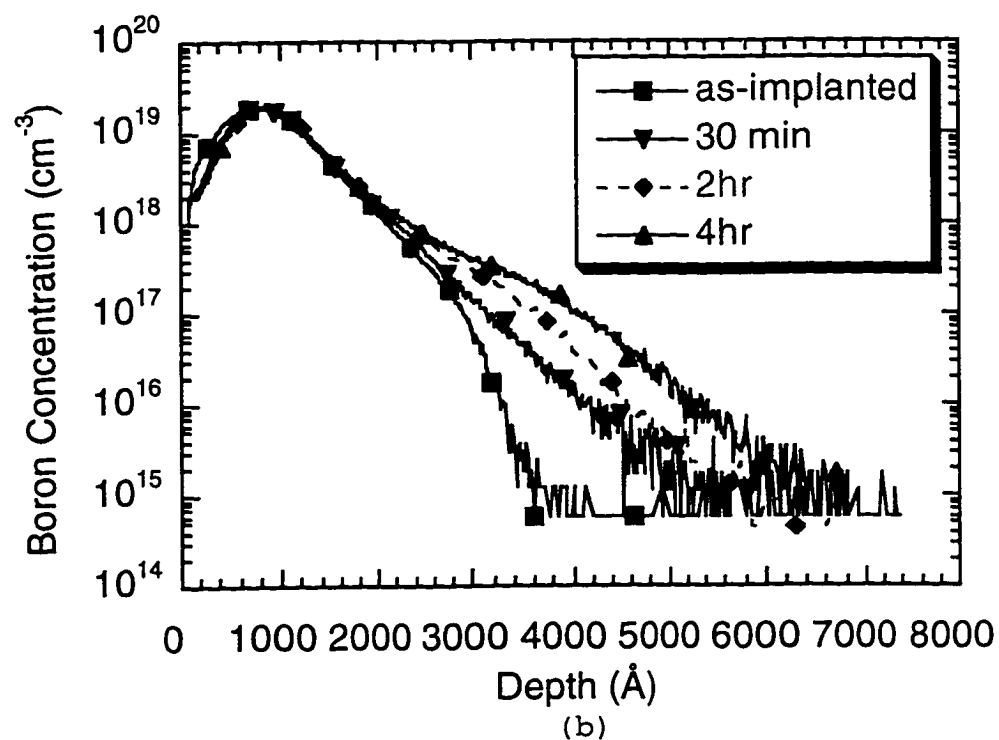
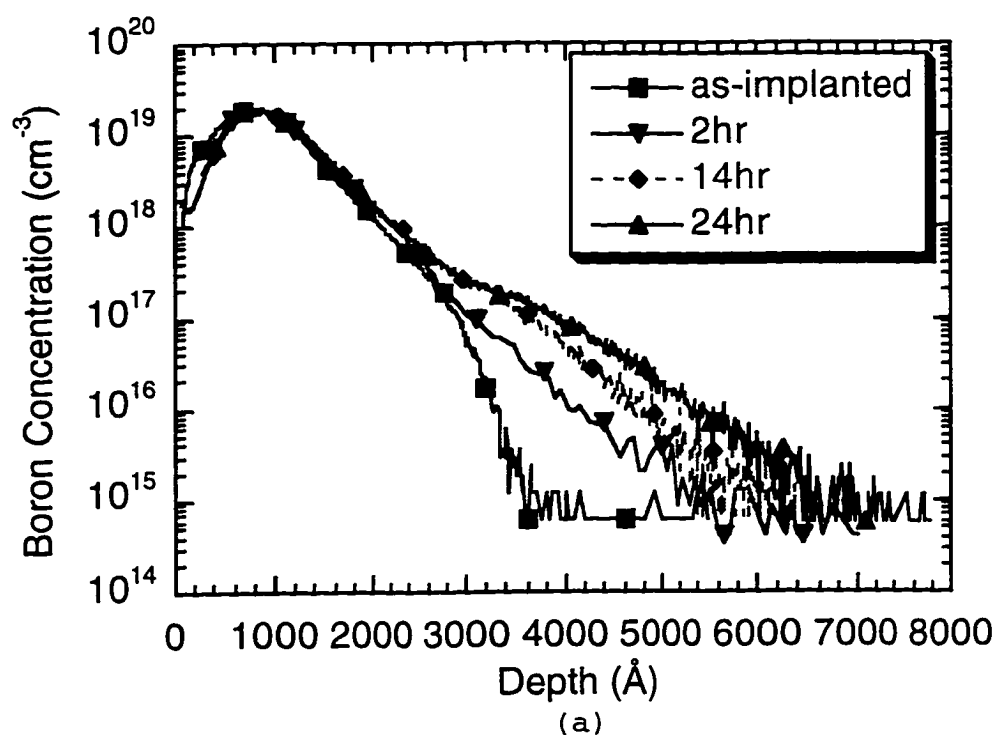
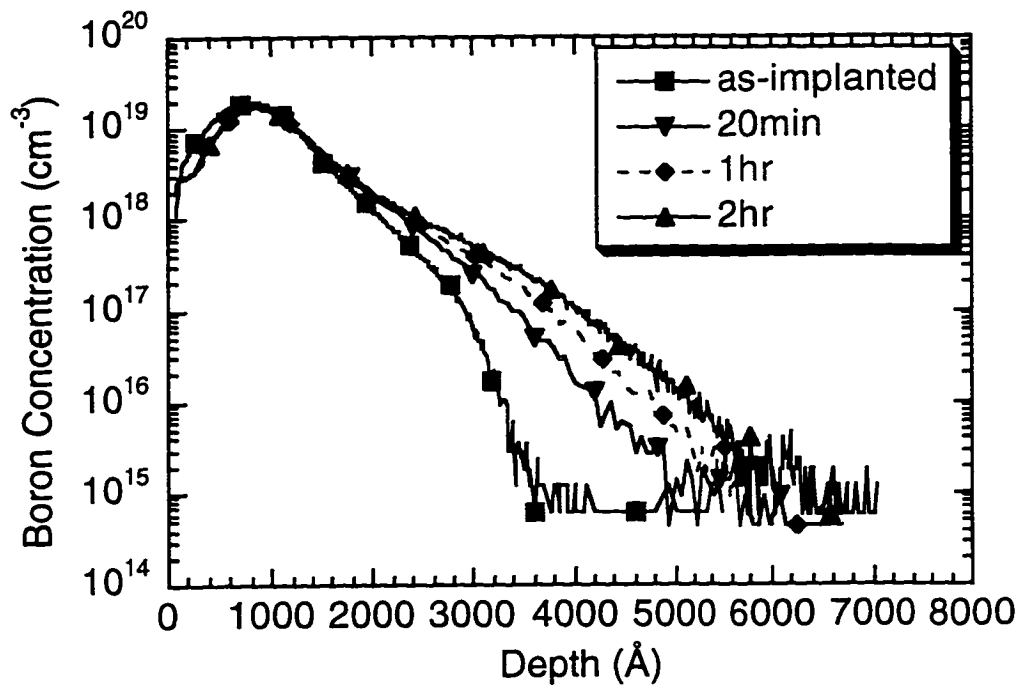
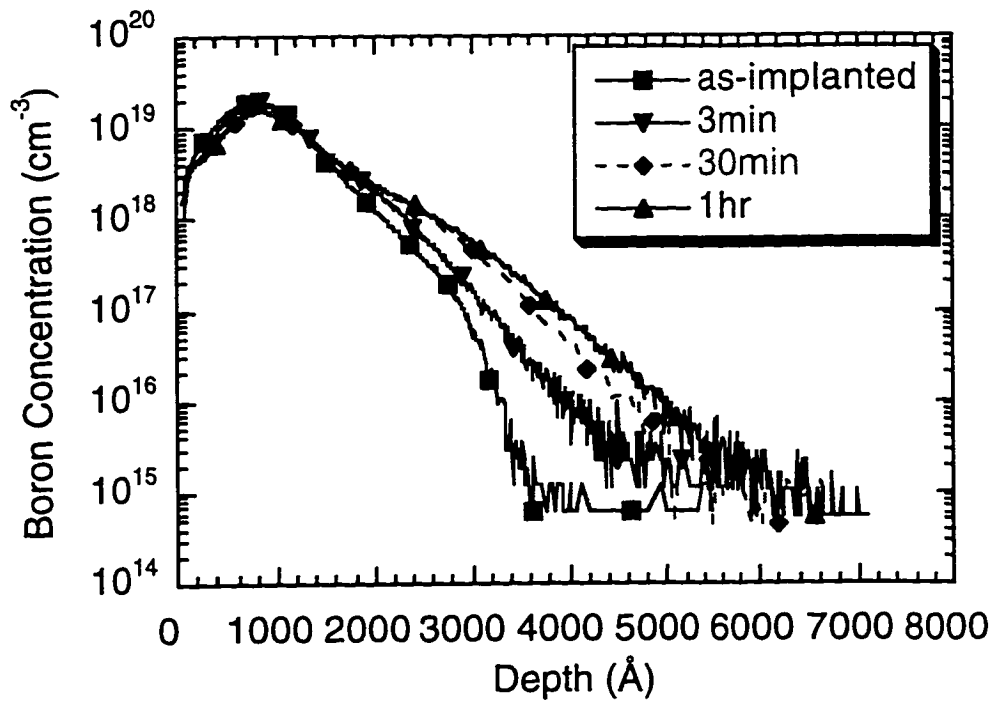


Figure 3.7. Dopant SIMS profiles of 20keV  $2 \times 10^{14} \text{ cm}^{-2}$   $\text{B}^+$  implanted Si after anneals at (a) 650°C, (b) 700°C, (c) 750°C and (d) 800°C for various times.



(c)



(d)

Figure 3.7. (Continued)

Reproduced with permission of the copyright owner. Further reproduction prohibited without permission.

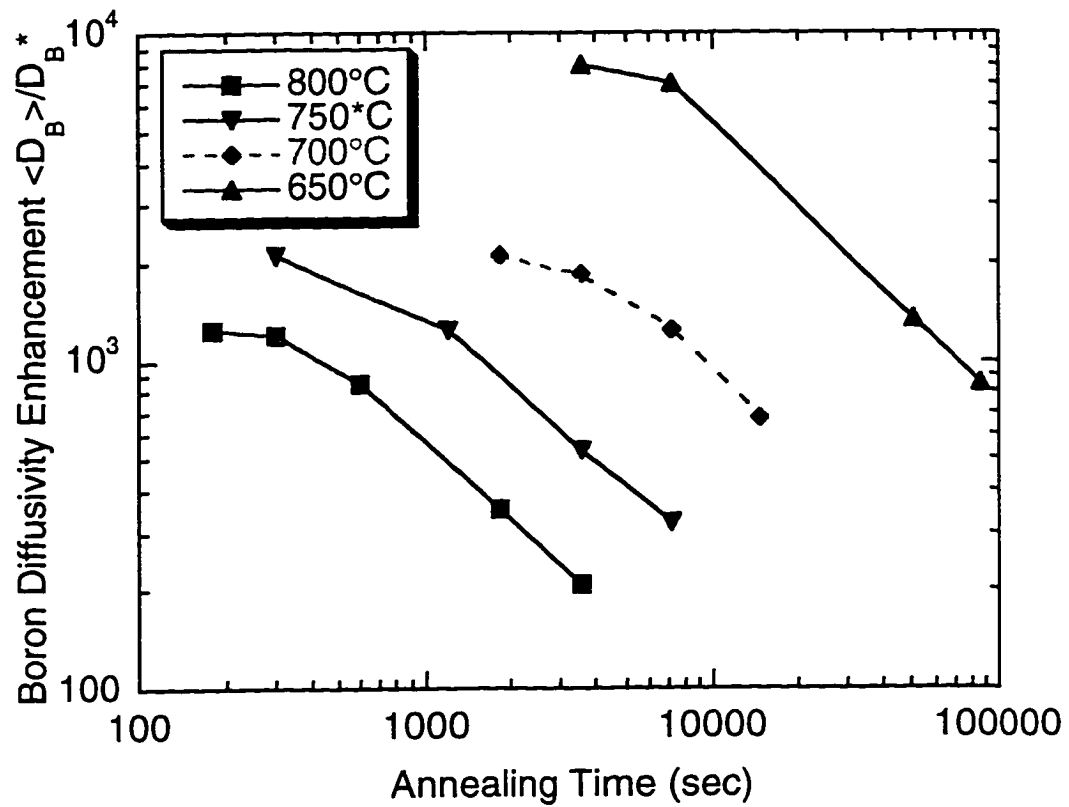


Figure 3.9. Time-averaged Boron diffusivity enhancement  $\langle D_B \rangle / D_B^*$  as a function of annealing time for different annealing temperatures.

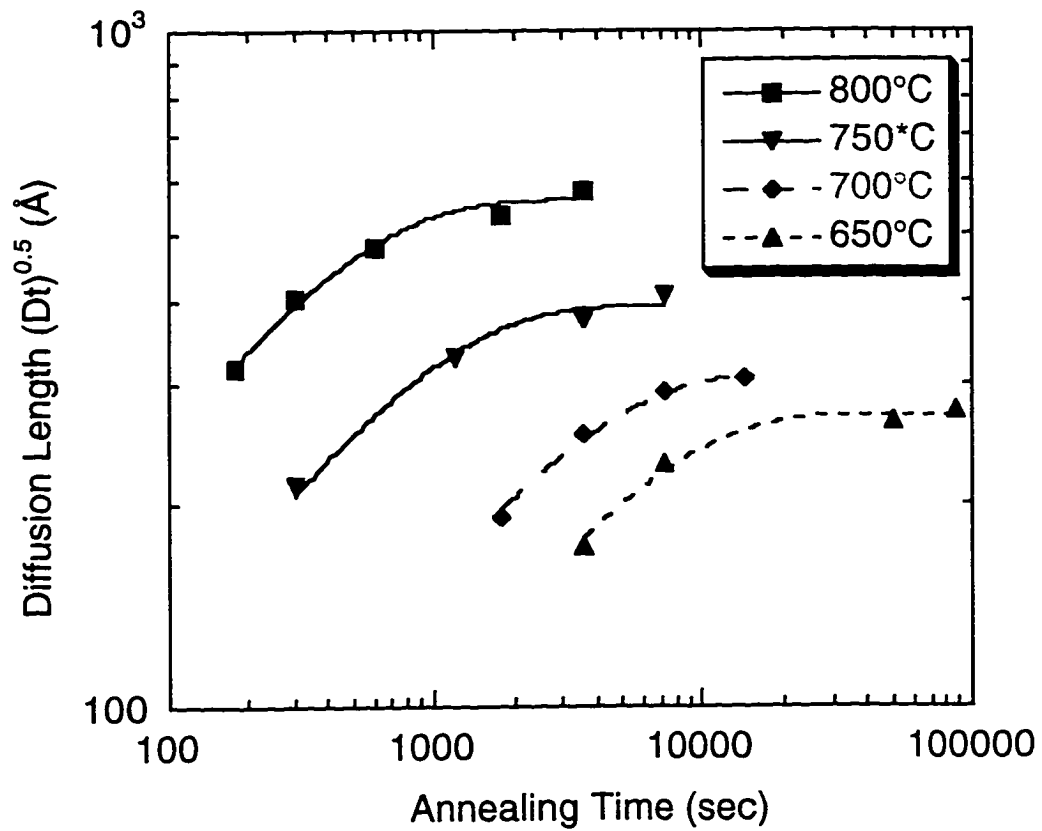


Figure 3.10. Boron diffusion length vs. annealing time for different annealing temperatures.

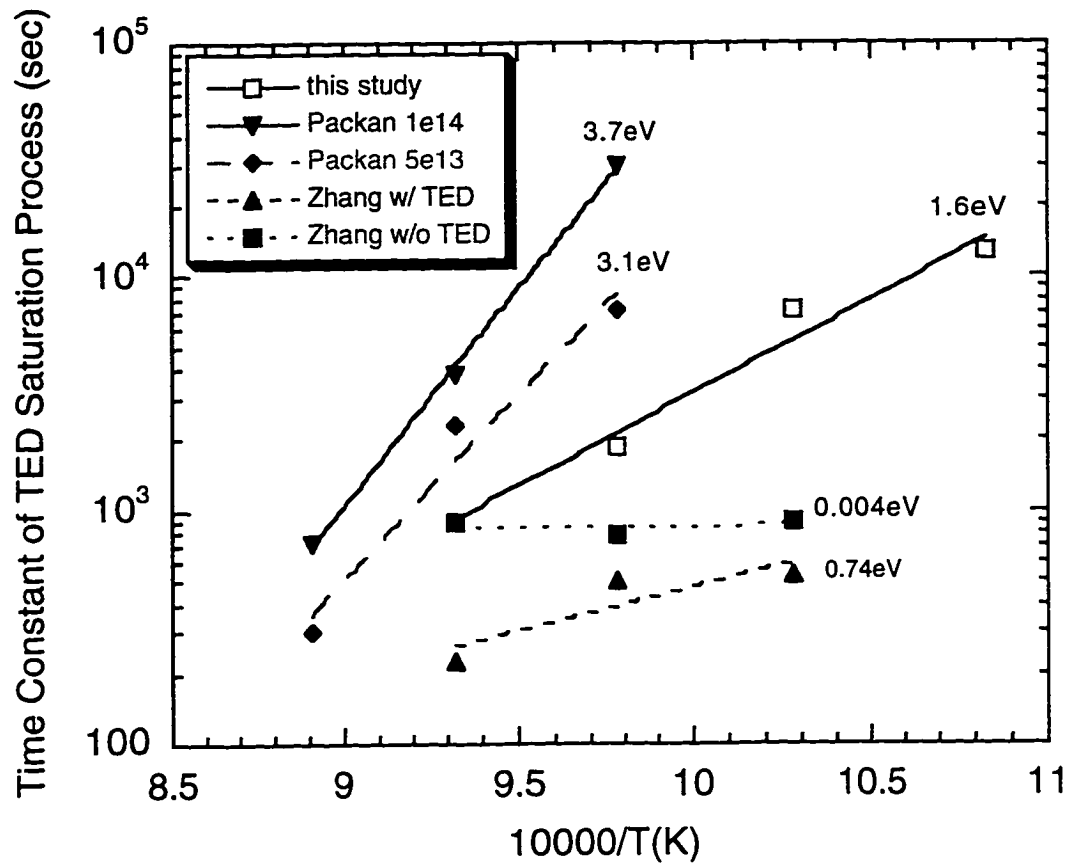


Figure 3.11. Time constant and activation energy of TED saturation process, comparison with previous studies.



CHAPTER 4  
THE INFLUENCE OF IMPLANT ENERGY ON DEFECT BEHAVIOR AND  
TRANSIENT ENHANCED DIFFUSION

4.1 Overview

It is believed that transient enhanced diffusion is a direct result of the damage created by the implantation process. Characteristics of the implanted ions (such as the mass), the substrate conditions (such as crystalline versus amorphous), and variations in implantation parameters (such as energy, dose, dose rate and temperature) would all cause variations in the damage and therefore affect dopant diffusion. This section discusses the effect of implant energy on defect behavior and TED.

It has been claimed that the amount of damage created by the implantation process is strongly dependent on the dose and the mass of the implant species but only weakly dependent on the implant energy.<sup>42</sup> Although higher energy does mean more kinetic energy per implanted ion, the resulting implant profile is more spread out and thus the "energy density" deposited per volume is lessened by this dilution effect. The effect of increasing energy is thus weakened and the number of interstitial-vacancy pairs would not be increased much provided the dose is the same. However, increasing energy can indeed change the location of the damage and the

depth of the interstitial and vacancy profiles and the separation between these two profiles. These changes can affect the defect behavior and TED, as will be discussed later.

## 4.2 Implant Energy Effect on Defect Behavior

### 4.2.1 Experimental Procedure

A single row of the implant matrix discussed in Chapter 2 was used to study the implant energy on {311} defect evolution. The implant dose was kept at  $2 \times 10^{14} \text{ cm}^{-2}$  and the energy was varied from 5 keV to 40 keV. Subsequent furnace anneals were conducted in a nitrogen ambient for times between 5 min and 1 hr at 750°C. The {311} defect density, average defect size and, areal density of interstitials trapped by {311} defects and the defect distribution during annealing were measured from the PTEM micrographs.

### 4.2.2 Defect Microstructure and Dissolution Process

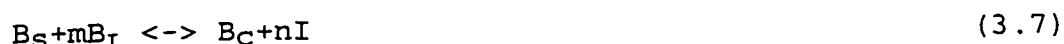
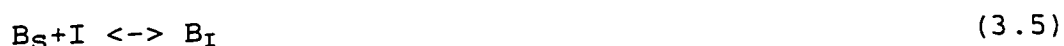
PTEM micrographs of the defects after implantation at 10 keV to 40 keV and anneals at 750°C from 5 min to 1 hr are shown in Fig. 4.1(a)~(d). No defects were observed for the 5 keV implant and therefore the pictures for those samples are not included. {311} defects are the only type of extended defects observed under the TEM in the 10 keV and 20 keV implants. A majority of {311} defects together with just a few dislocation loops are observed in the 30 keV and 40 keV

implants. For each of those implants showing {311} defects, the number of the defects decreases with increasing annealing time. This dissolution process is more rapid for a lower implant energy.

The areal density of interstitials bound by {311} defects during the annealing process was measured from the PTEM micrographs and the results are presented in Fig. 4.2. The dots in the plot are the actual data points and the lines are the exponential fitting curves for the data with the form of eq. (3.1). The emission of interstitials from {311} defects clearly shows an exponential time-dependence, which is stronger for lower implant energies. After a 30 min anneal at 750°C, {311} defects in the 10 keV implant almost dissolved completely. The density of the remaining trapped interstitials is about  $1.8 \times 10^{11} \text{ cm}^{-2}$ . For the 40 keV implant, after an anneal of 1 hr, there is still an areal interstitial density of about  $1.2 \times 10^{12} \text{ cm}^{-2}$  contained in {311} defects. The maximum density of trapped interstitials observed was about  $2 \times 10^{13} \text{ cm}^{-2}$  for the 10 keV implant and about  $3.5 \times 10^{13} \text{ cm}^{-2}$  for the 40 keV implant after an anneal for 5 min and these values are much lesser than the implant dose of  $2 \times 10^{14} \text{ cm}^{-2}$ . This implies the existence of immobile boron interstitial clusters and/or mobile boron interstitial pairs which might have trapped the missing interstitials assuming that the "plus one" model holds. There is, however, another possible configuration that could consume interstitials, i.e., silicon self-interstitial complex--two

interstitials split along  $\langle 110 \rangle$  direction occupying one lattice site. According the ab initio calculations conducted by Diaz de la Rubia et al. (private communication) this configuration is energetically unfavorable with a formation energy of about 3.7 eV. Interstitials are more likely to pair with boron atoms because the binding energy of a  $B_S$ -I pair is about 1.1 eV.

The lack of  $\{311\}$  defects in the 5 keV sample and the lower density of interstitials trapped by  $\{311\}$  defects in a lower energy implant could be attributed to at least the following four factors: (1) Higher energy might introduce more as-implanted damage which may further induce more trapped interstitials in extended defects (if formed) after annealing. (2) Higher energy causes larger separation between the as-implant vacancy profile (closer to the surface) and the interstitial profile (further away from the surface) because of the larger forward momentum carried by the implanted ions. The result of this might be that the I-V recombination rate is lower and the number of interstitials available to form extended defects is higher. (3) According to a series of proposed defect reactions<sup>113</sup> which describe the generation and clustering of mobile boron atoms given by eq.(3.5) and (3.7),



at a lower implant energy, the concentrations of  $B_S$  or  $B_I$  and silicon interstitials in the implant peak region are higher,

which favors the formation of boron clusters which bind excess interstitials. This will reduce the total number of interstitials available for forming {311} defects. (4) The surface recombination effect is more efficient for a lower energy when the damage region is closer to the surface. More interstitials are drawn to the surface and less are available for defect formation during annealing.

If the time constant of the {311} defect dissolution process is chosen as the time required for the number of interstitials to decrease to  $1/e$  of its maximum value, then it would be about 5 min for the 10 keV implant and 16 min for the 40 keV implant. This time constant is plotted in Fig. 4.3 as a function of energy. It is interesting to note that, if we derive from Fig. 4.3 the time constant of the 5 keV implant, it would be about 2.6 min. If {311} defects existed in the 5 keV implant from the beginning, we should be able to see them after a 5 min anneal, even though the defect density would be low, yet we do not see any defects. This could be attributed to one or a combination of the factors discussed above.

#### 4.2.3 Defect Density, Size and Distribution during Annealing

The {311} defect density for different implants as a function of annealing time measured from PTEM images is shown in Fig. 4.4. If the annealing time is short (e.g., less than 10 min), the lower energy implant shows a slightly higher density of {311} defects. This is probably due to earlier

formation and coarsening of {311} defects in the higher energy implants. However, the defects dissolve faster for a lower energy. As annealing time increases further, defect density is higher for a higher energy implant. The difference in defect density becomes more significant when the annealing time increases. After a 30 min anneal, the 10 keV implant shows a defect density of only  $3.2 \times 10^8 \text{ cm}^{-2}$ , while the 40 keV implant shows a density of  $2.7 \times 10^9 \text{ cm}^{-2}$ .

The average {311} defect size as a function of annealing time for different implant energies is shown in Fig. 4.5. The average defect size increases with annealing time initially, and then decreases when the defects enter a purely dissolution regime. This final dissolution regime is only observed for the 10 keV implant for the current annealing times. As the implant energy increases, the average defect size increases. After an anneal of 15 min, the 20 keV implant shows an average defect size of about 518 Å, while for the 40 keV implant, it is about 952 Å.

Figure 4.6 (a)~(d) show the size distribution of {311} defects after anneals at 750°C for various times for 10 keV to 40 keV implants. Higher energy implants have a broader distribution than lower energy implants. The figure also shows a larger average defect size and a slower dissolution rate for a higher energy. For each energy, the average defect size increases while the defect density at each size decreases during annealing. This behavior together with the fact that the total number of interstitials trapped in {311}

defect decreases with increasing time indicates that the Ostwald ripening process occurs along with the defect dissolution process. Large {311} defects grow by absorbing the interstitials released from small defects as a result of higher local interstitial concentration around small defects. Meanwhile, large defects themselves release interstitials into the bulk. This resulted in the final defect distribution we have observed.

As a summary, the {311} defect microstructure and annealing behavior as a function of implant energy (5 keV ~ 40 keV) have been studied using TEM. No defects are observed in the 5 keV implant. There are more interstitials bound by {311} defects in higher energy implants although the maximum density observed (about  $2\sim 3.5 \times 10^{13} \text{ cm}^{-2}$  after an anneal of 5 min at 750°C) are all far less than the implant dose ( $2 \times 10^{14} \text{ cm}^{-2}$ ). The defect density is higher for a lower implant energy after a short anneal time (10 min) and then becomes lower as time increases. The average defect size is larger for a higher implant energy. The size distribution of defects shows a co-occurrence of the Ostwald ripening process and the dissolution process. The lack of {311} defects in the 5 keV implant and the decrease in density of trapped interstitials by {311} defects with decreasing implant energy might be the result of one or a combination of the following factors: decreased damage product with decreasing energy, increased I-V recombinations, increased boron interstitial cluster formation and an increased surface recombination.

Each of these factors could decrease the number of interstitials available for the formation of {311} defects.

### 4.3 Implant Energy Effect on Transient Enhanced Diffusion

#### 4.3.1 Experimental Procedure

In order to study the effect of interstitial release during TED independent of the diffusing profile, doping superlattices were used. Boron  $\delta$ -doping superlattices were grown by low temperature molecular beam epitaxy (LTMBE) on float zone Si (100) substrate with boron-doped to a resistivity of 1000  $\Omega\text{cm}$ . The custom-made MBE system had a base pressure of  $4 \times 10^{-11}$  Torr. The temperature during growth was set through the choice of the heater power, which in turn had been calibrated in terms of temperature by laser interferometry. The samples contained six 100 Å wide box-shaped boron spikes with a separation of about 1000 Å between each spike. The peak boron concentration of these spikes was about  $1.4 \times 10^{18} \text{ cm}^{-3}$ . This low concentration kept boron diffusion intrinsic for the as-grown control samples during the following anneals and avoided the complication of extrinsic effects. Boron ions were implanted into the superlattices at energies of 5 keV, 10 keV, 20 keV and 40 keV to a dose of  $2 \times 10^{14} \text{ cm}^{-2}$  at room temperature. The samples were then annealed at 750°C for times of 3 min, 15 min and 2 hr in a nitrogen ambient. The temperature error range is estimated to be  $\pm 10^\circ\text{C}$ . Due to the finite rise time of the



sample temperature, the error range for the 3 min sample could be  $\pm 30^\circ\text{C}$ . The initial boron profile as well as the profiles after implantation and annealing were measured by SIMS with 3.0 keV  $\text{O}_2^+$  at a current of 50 nA. The raster size was  $150 \times 150 \mu\text{m}^2$  and the analyzed area was  $60 \times 60 \mu\text{m}^2$ . The broadening of the B profiles was simulated using the process simulator PROPHET. The spikes that merged into the B implant profile were excluded from the simulation.

#### 4.3.2 Dopant Diffusion Behavior

SIMS profiles of boron in the superlattices implanted with 5 keV to 40 keV boron ions are shown in Fig. 4.7(a)~(d). As can be seen, a higher energy results in a deeper implant profile and a greater enhanced diffusion of the buried boron spikes. The time-averaged boron diffusivities for a particular spike,  $\langle D_B \rangle$ , were extracted by finding the value of  $D_B$  in the simulation that resulted in the best match between diffused and target profiles. Using the literature value of  $D_B^* = 0.757 \exp(-3.46/kT)$  (eq. (3.8)), diffusivity enhancement  $\langle D_B \rangle / D_B^*$  is thus obtained. For the inert ambient annealed control samples, it is expected that no diffusion enhancement occurs, i.e.,  $\langle D_B \rangle / D_B^* = 1$  or  $\langle D_B \rangle = D_B^*$ . We have extracted  $\langle D_B \rangle$  via simulation for the 2hr annealed control sample. Taking an average over different spikes since  $\langle D_B \rangle$  is depth-independent, we found that  $\langle D_B \rangle$  is about  $1.6 \times 10^{-17} \text{ cm}^2/\text{s}$ , about 2 times greater than the predicted value ( $7.2 \times 10^{-18} \text{ cm}^2/\text{s}$ ), which is within the error range of

furnace temperature and SIMS analysis accuracy and the ability to predict  $D_B^*$ . The diffusion distance for the control sample is indeed too small to be extracted reliably since that the SIMS depth has an estimated error of 5%.

Figure 4.8 (a)~(d) are plots of  $\langle D_B \rangle / D_B^*$  as a function of depth for different implant energies after each anneal. The program assumes that the total sheet concentration is preserved for each spike during diffusion, i.e., the depth integration of boron concentration under each spike remains a constant after implantation and annealing. However, the influx from the surface implant into the spike region actually violates the conservation. The error bars of  $\langle D_B \rangle / D_B^*$  to be shown do not include this effect. The dots in Fig. 4.8 are the data points and the lines are exponential fitting curves. We can see that the value of  $\langle D_B \rangle / D_B^*$  decays exponentially with increasing depth, and the decay length is smaller at a shorter annealing time (3 min) than longer times (15 min and 2 hr), i.e., the  $\langle D_B \rangle / D_B^*$  versus depth curve is steeper. The cross of  $\langle D_B \rangle / D_B^*$  curves for the 3 min and 15 min anneals implies that interstitials have not diffused deep enough to cause a large diffusion enhancement after a shorter time. The slightly positive slopes of the  $\langle D_B \rangle / D_B^*$  curves for the 15 min and 2 hr anneals might be due to the SIMS analysis and the simulation error. After a short time (3 min) anneal, for each particular spike the value of  $\langle D_B \rangle / D_B^*$  increases with increase in implant energy. For example, for a boron spike at a depth of around 3800 Å, after

an anneal of 3 min, the 5 keV implant shows an enhancement of about 260, whereas the 40 keV implant shows a much greater enhancement of about 2800. As the anneal time increases to longer than 3 min, this difference is less distinguishable for energies above 5 keV.

#### 4.3.3 Correlation Between Defects and TED

The average boron diffusivity at a particular depth of the sample can be expressed as

$$\frac{\langle D_B \rangle}{D_B^*} = \frac{\langle C_I \rangle}{C_I^*} = \frac{1}{t} \int_0^t \frac{C_I}{C_I^*} dt_1 \quad (4.1)$$

where  $C_I$  is the instantaneous value of interstitial concentration at time  $t_1$  and  $t$  is the diffusion time. If the instantaneous interstitial supersaturation level  $C_I/C_I^*$  is greater than 1, we will see the enhancement of diffusivity. If we assume that the excess interstitials introduced by an implant are trapped in interstitial-contained defects (in our case, {311} defects and mobile B-I pairs) in the initial stage of the annealing, then we can consider these defects as an interstitial reservoir that keeps  $C_I/C_I^*$  constant for a short period of time ( $t < t_0$ ). If at time  $t > t_0$  all the {311} defects have dissolved and all B-I pairs have broken up, then the reservoir is empty and  $C_I/C_I^*$  drops abruptly to 1.

Mathematically this can be expressed as

$$\frac{C_I}{C_I^*} = \begin{cases} 1 + E \dots (t < t_0) \\ 1 \dots (t \geq t_0) \end{cases} \quad (4.2)$$

where  $E$  is the supersaturation of interstitials. The integral of eq. (4.1) would then become

$$\frac{\langle D_B \rangle}{D_B^*} = \frac{1}{t} \int_0^t (1+E) dt_1 = 1 + E \dots (t < t_0) \quad (4.3)$$

$$\frac{1}{t} \left[ \int_0^{t_0} (1+E) dt_1 + \int_{t_0}^t dt \right] = 1 + \frac{t_0}{t} E \dots (t \geq t_0)$$

From the above equation we can see that if  $\langle D_B \rangle / D_B^* - 1$  is plotted as a function of time in a log-log scale, it should be a curve that is flat for  $t < t_0$  and drops approximately as  $1/t$  for  $t \geq t_0$  and the breaking point  $t_0$  is the time when the interstitial concentration reaches equilibrium value and TED is completed. This of course is a simplified picture since TED sources do not turn off abruptly, but rather the interstitial supersaturation decays smoothly over the time period studied. In other words we may not see only one breaking point  $t_0$  but more than one, e.g.,  $t_0$ ,  $t_1$ ,  $t_2$ , etc.. Figure 4.9 shows a plot of  $\langle D_B \rangle / D_B^* - 1$  versus annealing time for different implant energies. Because of the finite speed of interstitial diffusion, we have to pick a fixed distance from the interstitial source to make the comparison. A distance of 3600 Å from the projected range of each implant was thus chosen in this plot. Because of the long interval between the annealing times, we did see just one breaking point  $t_0$  for  $E > 5$  keV. According to the above discussion, TED stops before 15 min for the 5 keV implant and within 15 min to 2 hr for higher energy implants.

The energy dependence of the time-averaged interstitial supersaturation  $\langle C_I \rangle / C_I^*$  after 3min and 2hr anneals is shown in Fig. 4.10 (a) and (b). For the 3 min anneal the interstitial supersaturation near the implant damage region

is much higher than that for larger depth and as a result the boron peaks near the implant damage region broaden much more than the deeper boron peaks. As time increases, this difference becomes less marked since the longer time allows for the excess interstitials to diffuse to deeper regions. For the 3min anneal, the overall trend shows  $\langle C_I \rangle / C_I^*$  decreasing with increasing depth and increasing with increasing implant energy. For the 2 hr anneal, the depth and energy dependencies of  $\langle C_I \rangle / C_I^*$  become much less prominent except for the lowest energy, 5 keV. The reason for the much shorter duration in TED and a less amount of diffusion enhancement at 5 keV may be related to several factors, including the source of the interstitials, as will be discussed later.

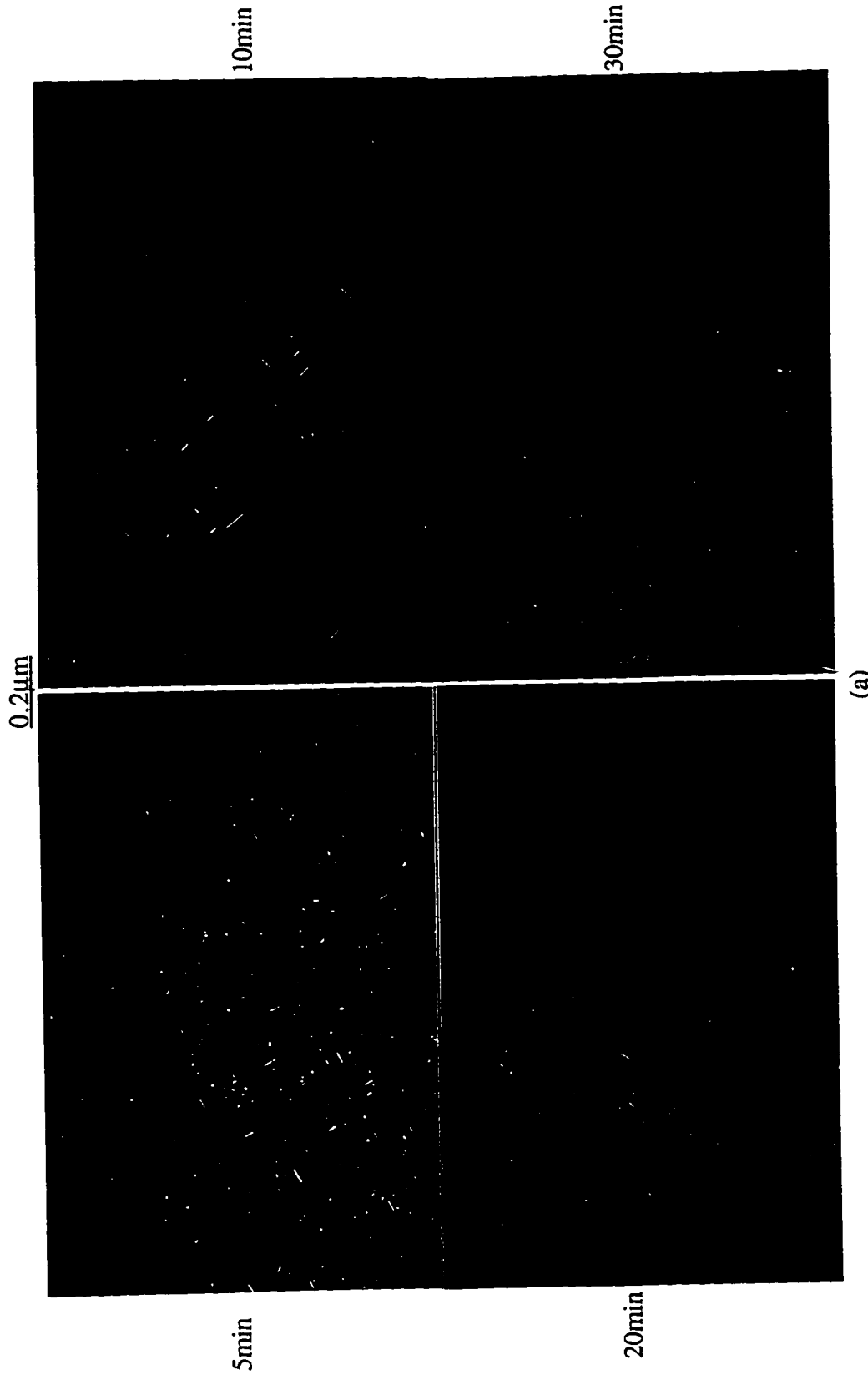
As we discussed in the first section of this chapter, there are no {311} defects in the 5 keV implant but they are the only type of visible defects in the 10 and 20 keV implants and comprise the majority of the defects in 30 and 40 keV implants. It is important to note that although there are no {311} defects in the 5 keV implant, TED of boron does occur. For this 5 keV sample annealed at 750°C, for times of 3 min to 2 hr, the diffusivity enhancement reduces from 980 to 17 for the second shallowest spike and from 100 to 11 for the deepest one. We believe TED occurs because interstitials are released from mobile boron interstitial pairs during annealing. Because of the relative proximity of the implant damage to the surface at this low energy, a large part of the

interstitials could be attracted to the surface so that the supersaturation of remaining interstitials is relatively low, however these remaining interstitials can still diffuse into the bulk and enhance dopant diffusion. Zhang et al.<sup>114</sup> have previously reported that TED was observed in 4keV  $1 \times 10^{14} \text{cm}^{-2}$  B<sup>+</sup> implanted Si without the existence of {311} defects. They attribute the source of interstitials driving TED to sub-microscopic clusters. They determined the duration of TED by noting when TED stops within the bounds of the SIMS resolution, and their TED saturation was 3 min~13 min at 750°C, much shorter than others have reported for TED saturation in samples with {311} defects. In our experiment we looked at the time averaged interstitial concentration instead of the instantaneous one, so we did not actually determine the time required for the interstitial concentration to return to its equilibrium level. However, we used the extracted  $D_B$  for the 2600 Å deep spike in the 5keV implant and simulated how Zhang et al.'s 4 keV  $1 \times 10^{14} \text{cm}^{-2}$  implanted boron profile would evolve after 3 min, 15 min and 2 hr and found that TED ended after 15 min, in agreement with their conclusion. Thus it is proposed that when {311} defects exist, their dissolution process might interact with that of mobile boron interstitial pairs, so that TED continues for much longer periods of time. The type of defects that supplies the interstitials regulates the duration of TED.

From Fig. 4.10(c) we can see that, after an anneal of

2 hr, i.e. after equilibrium is reached, the interstitial supersaturation level  $\langle C_I \rangle / C_I^*$  varies little when implant energy is above 5 keV. The factors that we discussed in the previous section on why {311} defects do not form in the 5 keV implant can also be used to explain the TED behavior. These factors include the formation of boron interstitial clusters, the implant damage, the I-V recombination rate and the surface recombination effect variations with implant energy. Since the first three factors are expected to change gradually with the changing of energy, surface recombination effect is believed to be the most significant factor that reduces the amount of diffusion in the 5keV implant. The energy threshold below which the surface starts to play an important role lies between 5keV and 10keV.

In summary, boron  $\delta$ -doping superlattices have been used to study the effect of implant energy (5 keV to 40 keV) on TED of boron implanted silicon. Higher implant energies ( $> 5$  keV) cause more total diffusion enhancement and longer TED duration. It is speculated that a threshold exists at an implant energy between 5keV and 10keV, below which the surface recombination effect strongly affects diffusion. It is also speculated that both mobile boron interstitial pairs and {311} defects existed in higher energy ( $> 5$  keV) implants and they function together to provide interstitials for TED. Hence the formation of {311} defects appears to result in a dramatic increase in the duration of TED.



(a)  
Figure 4.1 Weak beam dark field PTEM ( $g_{220}$ ) micrographs of  $2 \times 10^{14} \text{ cm}^{-2}$  B<sup>+</sup> implanted Si at an energy of (a) 10keV, (b) 20keV, (c) 30keV and (d) 40keV.



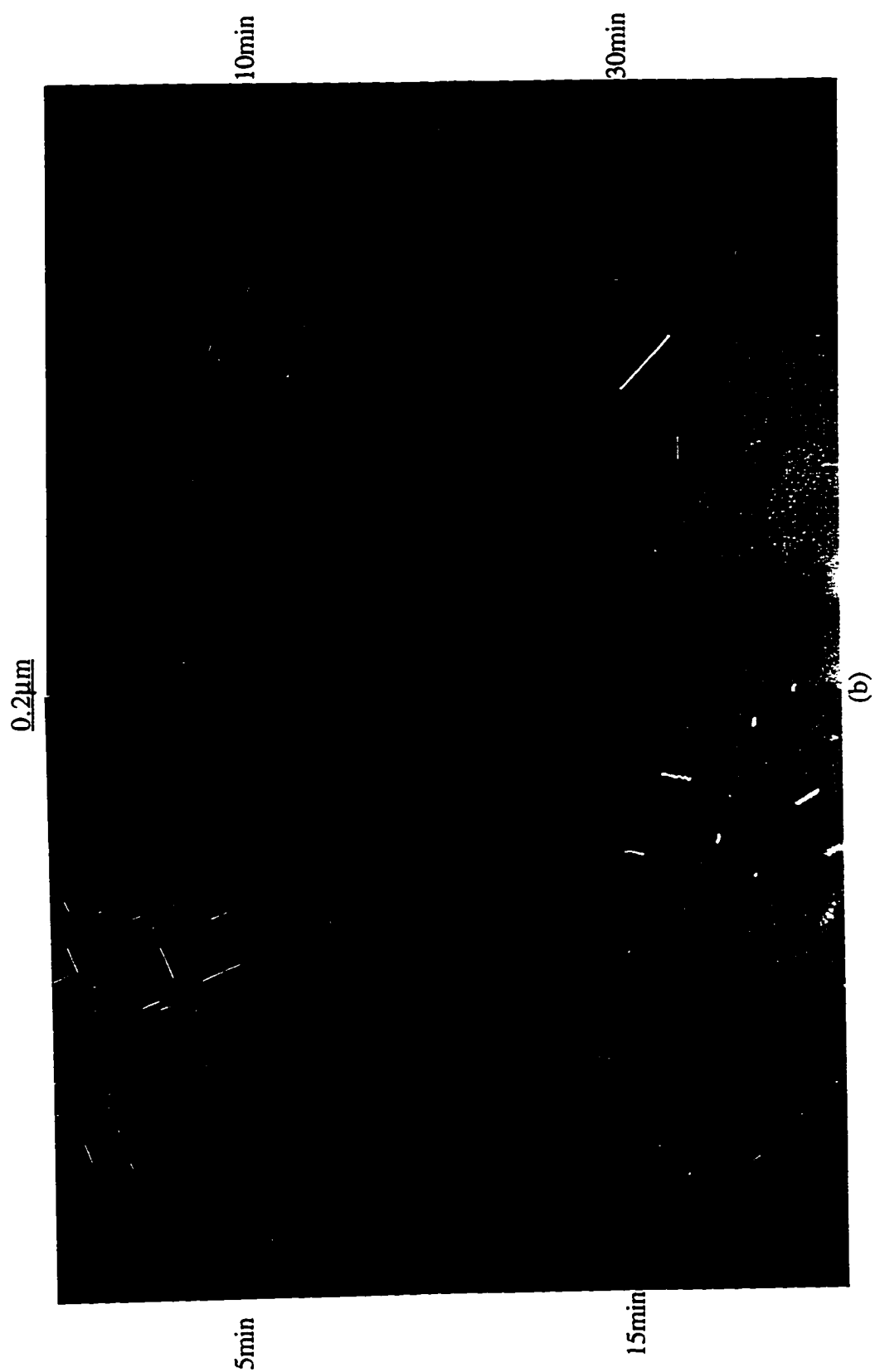


Figure 4.1 (Continued)

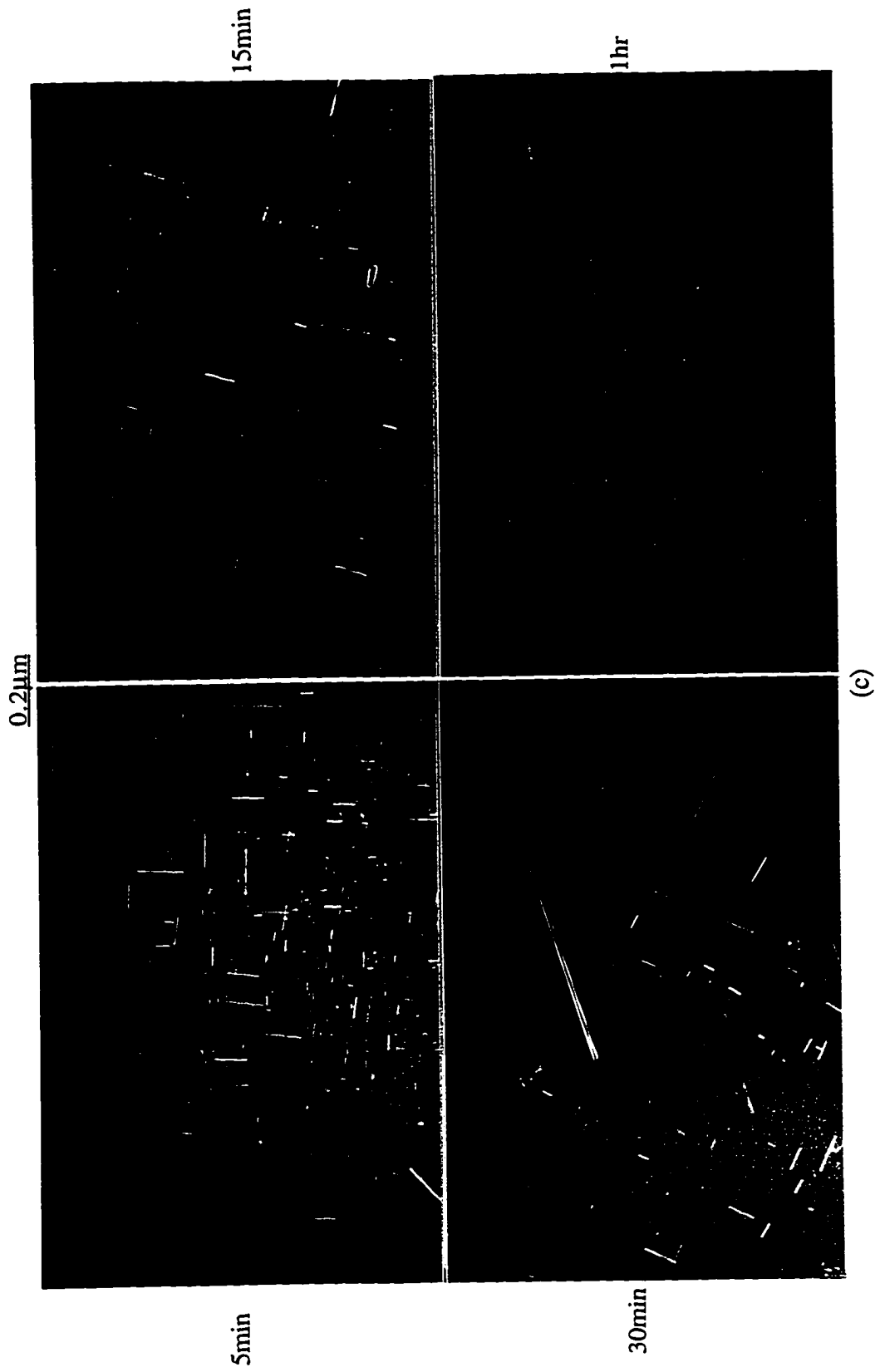


Figure 4.1 (Continued)

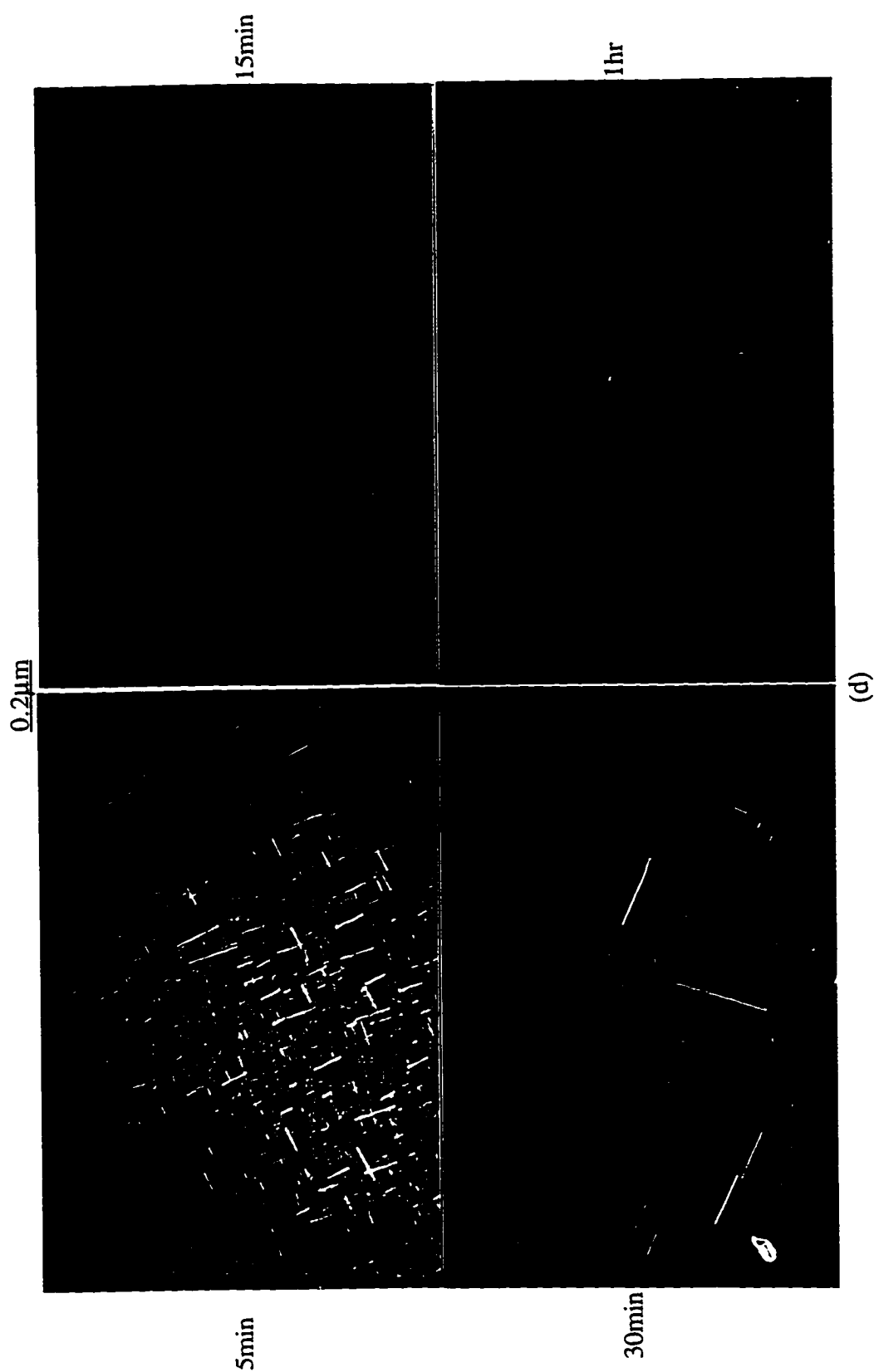


Figure 4.1 (Continued)

(d)

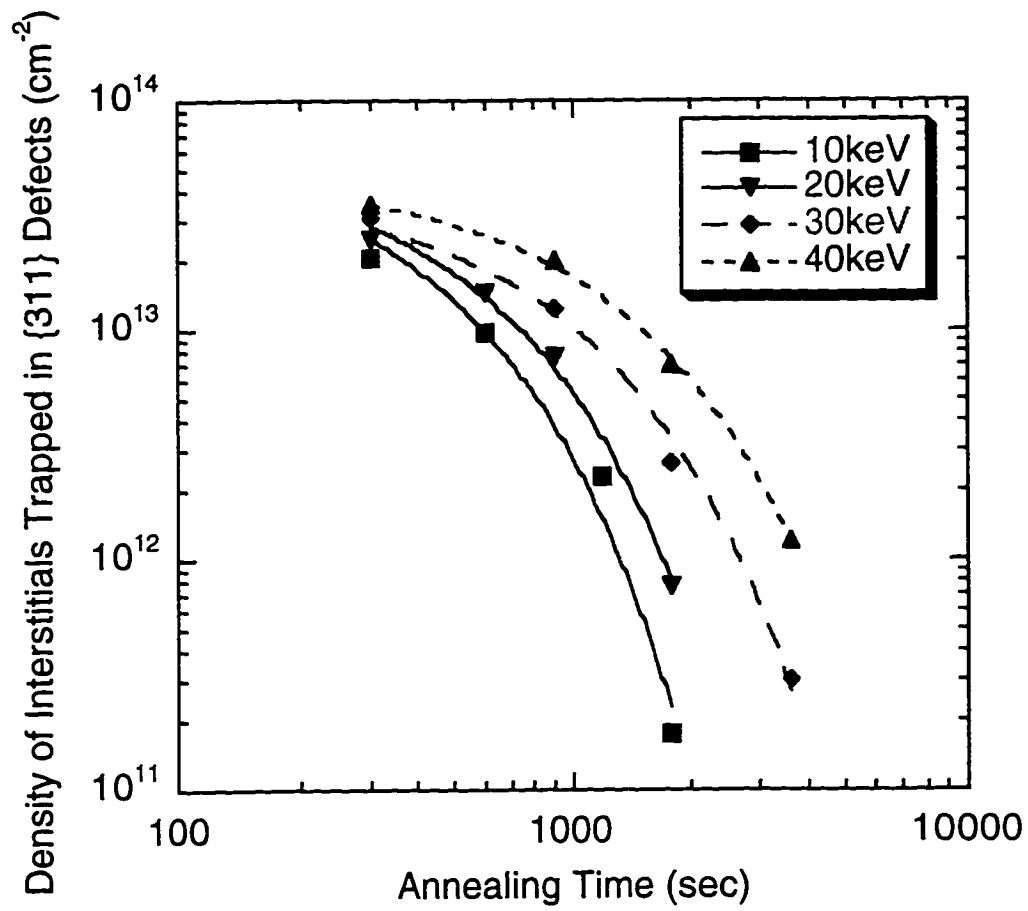


Figure 4.2. Density of interstitials trapped in {311} defects in 10keV~40keV B $^{+}$  implanted Si, annealed at 750°C.

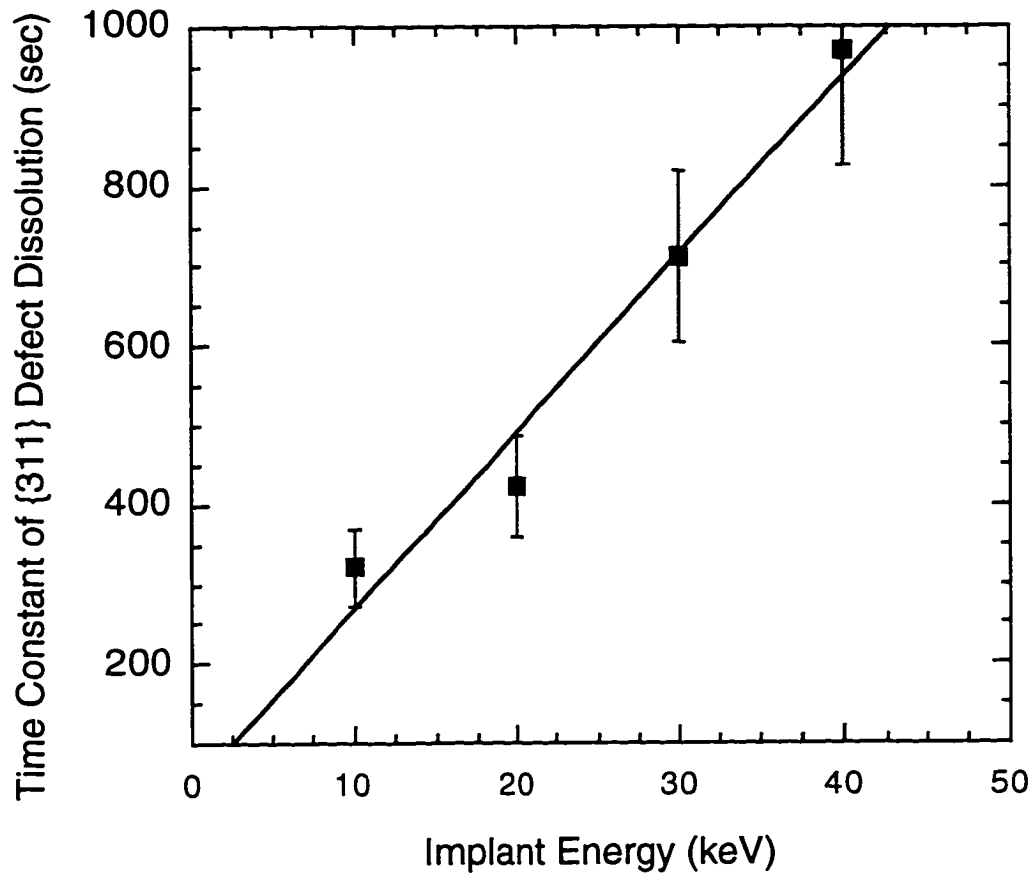


Figure 4.3. Time constant of the dissolution process of the interstitials trapped in {311} defects as a function of implant energy, annealed at 750°C.

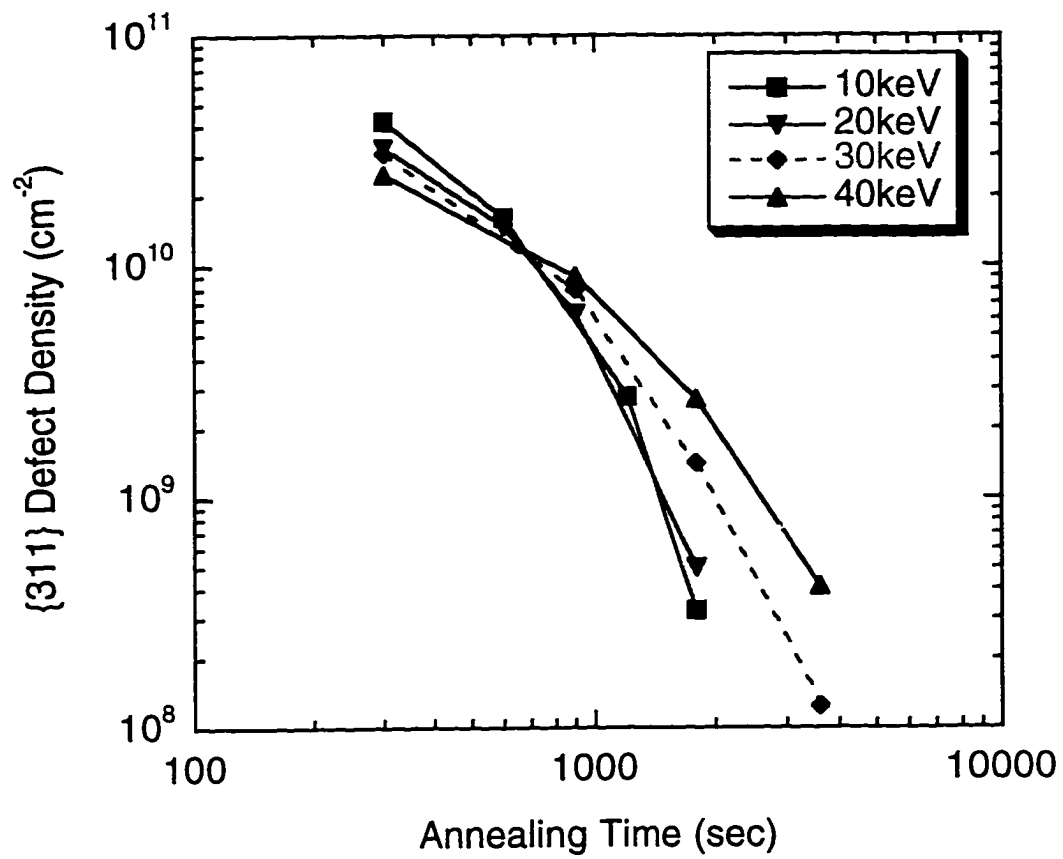


Figure 4.4. Density of {311} defects as a function of annealing time for different implant energies.

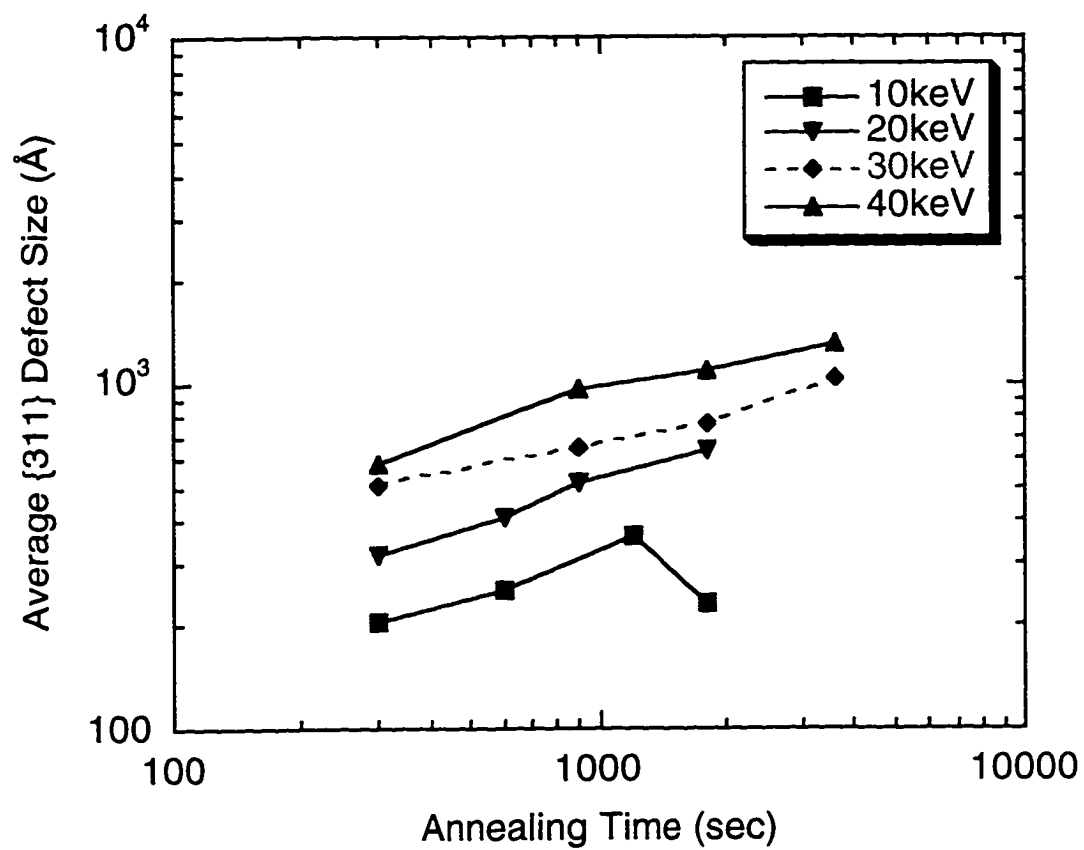
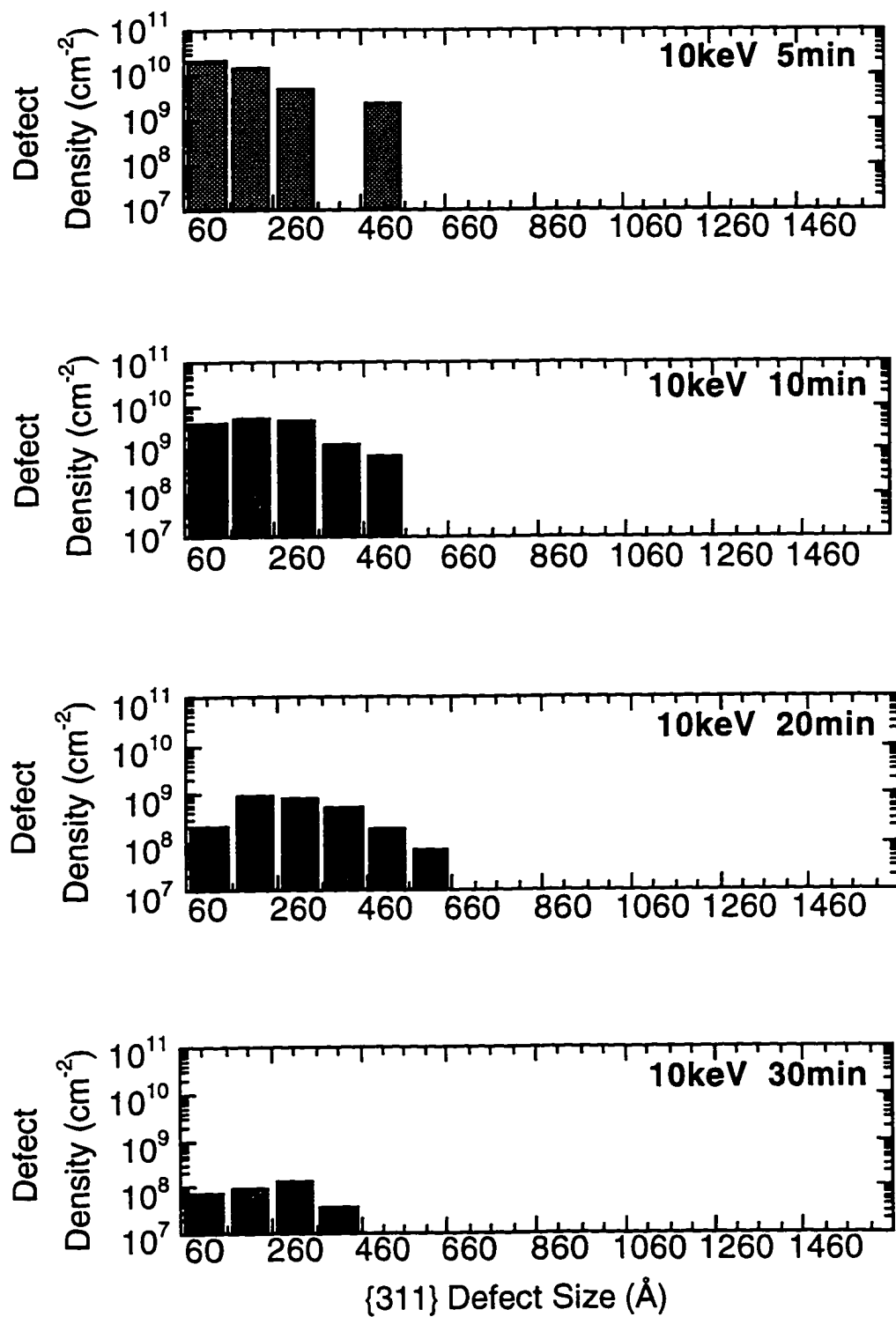


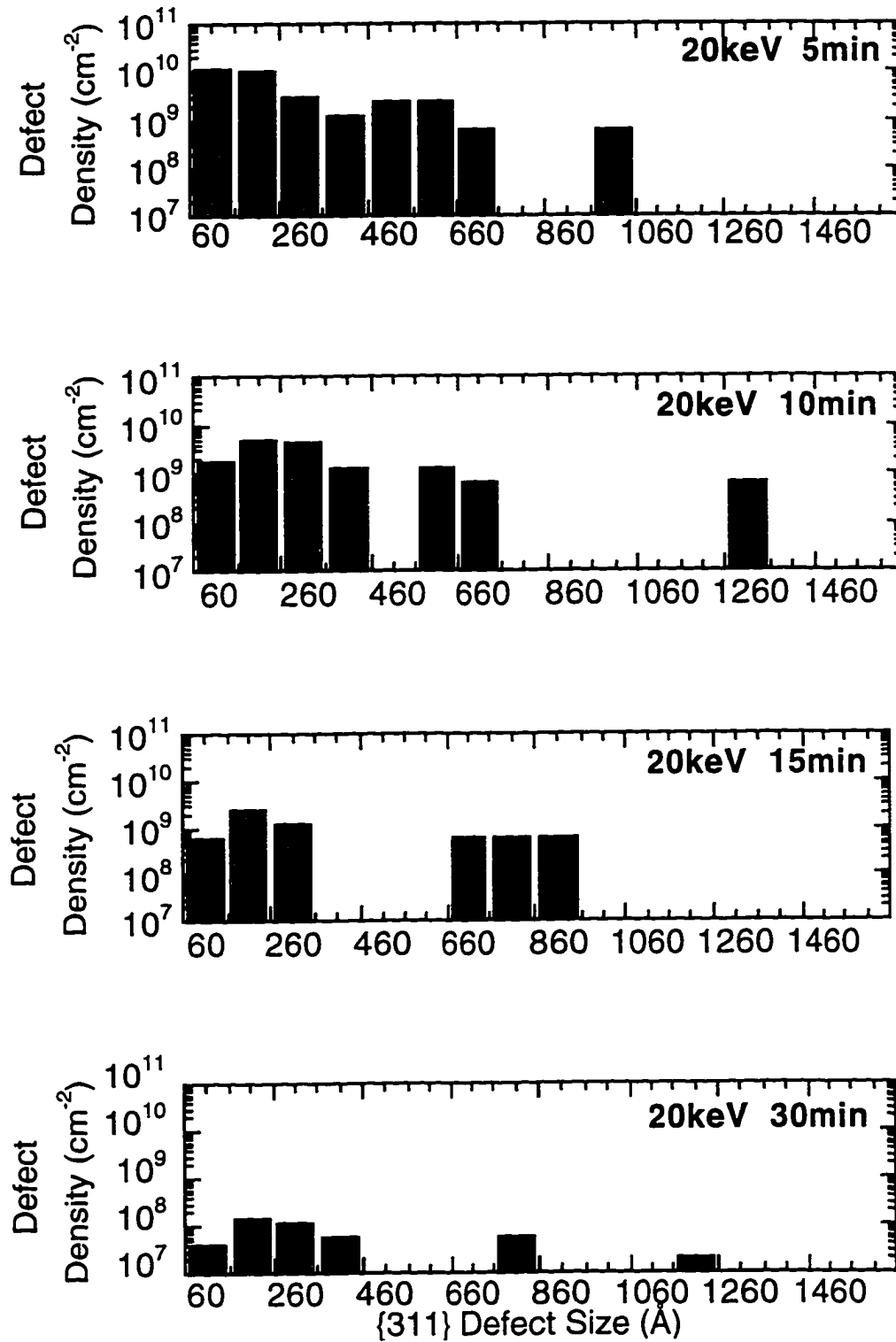
Figure 4.5. Average size of {311} defects as a function of annealing time for different implant energies.



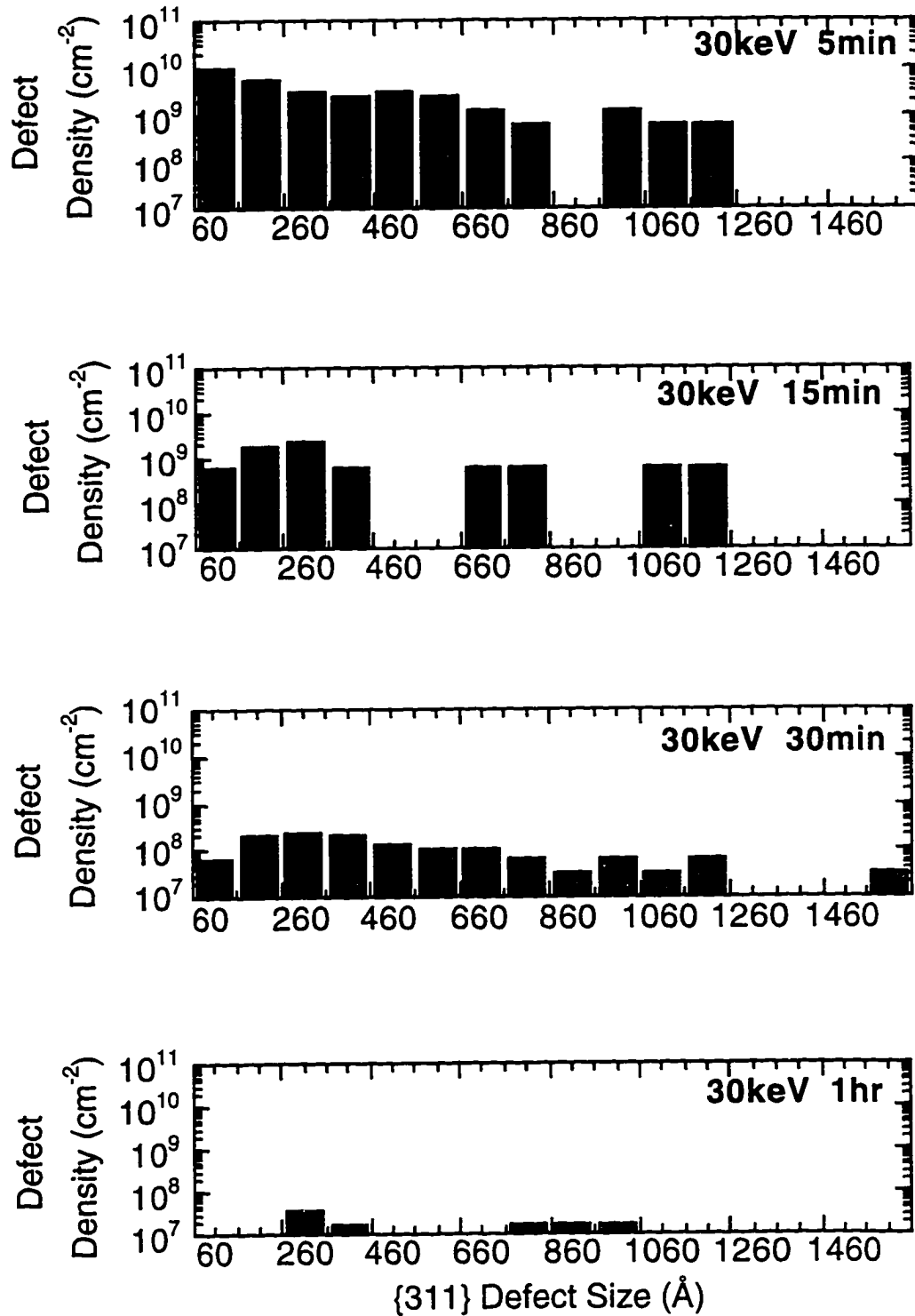
(a)

Figure 4.6. {311} defect size distribution for (a) 10keV (b) 20keV (c) 30keV and (d) 40keV implants, annealed at 750°C.

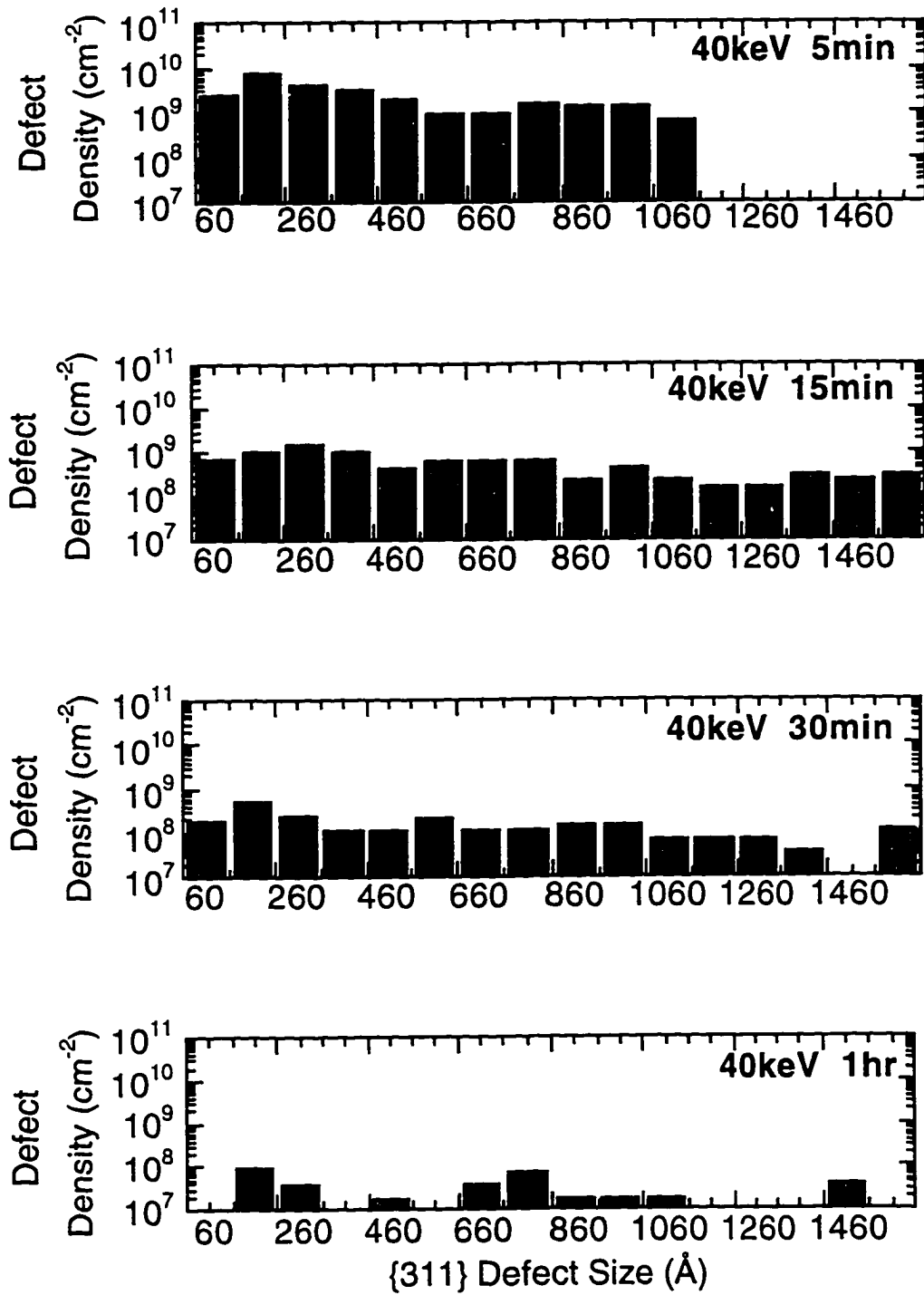




(b)  
Figure 4.6. (Continued)



(c)  
Figure 4.6. (Continued)



(d)

Figure 4.6. (Continued)

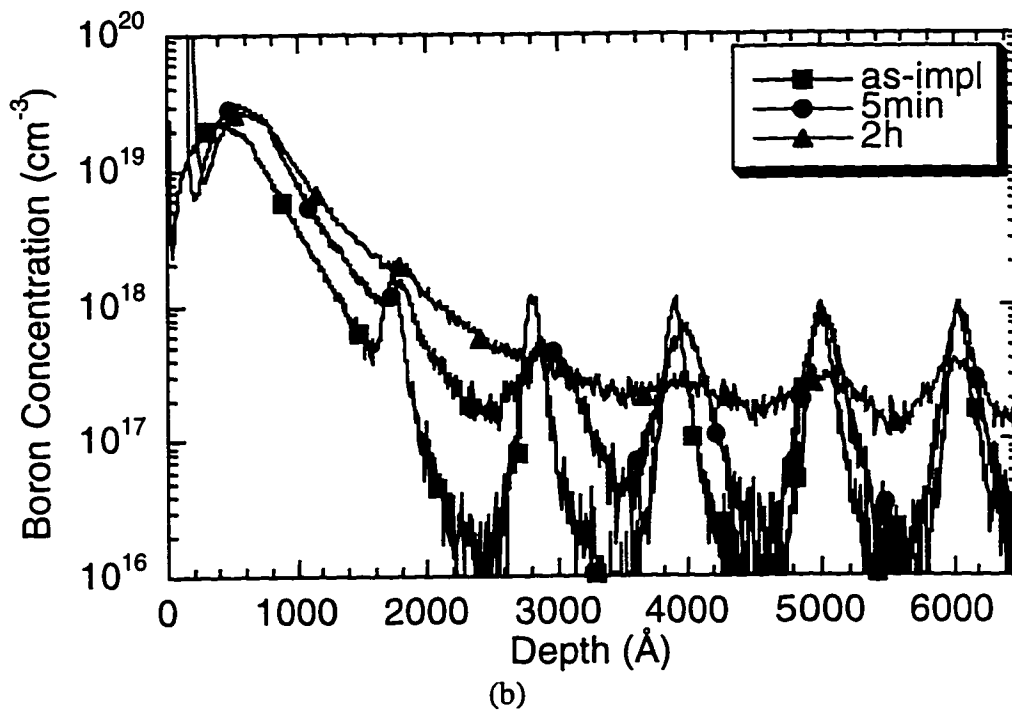
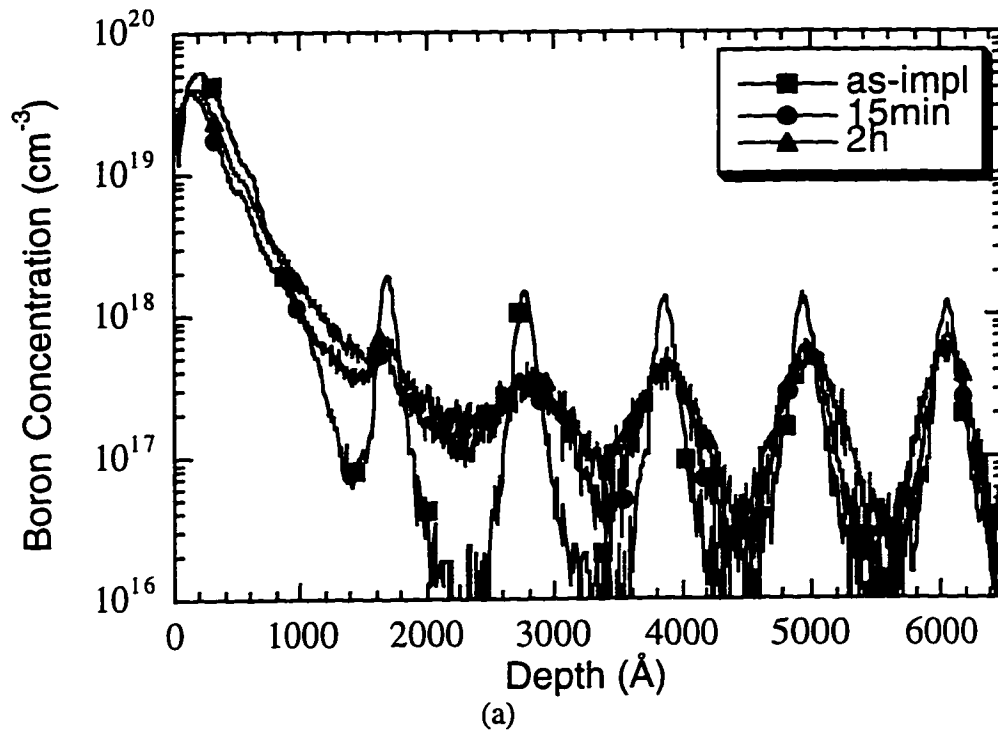


Figure 4.7. SIMS profiles of boron in  $2 \times 10^{14} \text{cm}^{-2} \text{B}^+$  Implanted Si superlattices at an energy of (a) 5keV, (b) 10keV, (c) 20keV and (d) 40keV, annealed at  $750^\circ\text{C}$ .

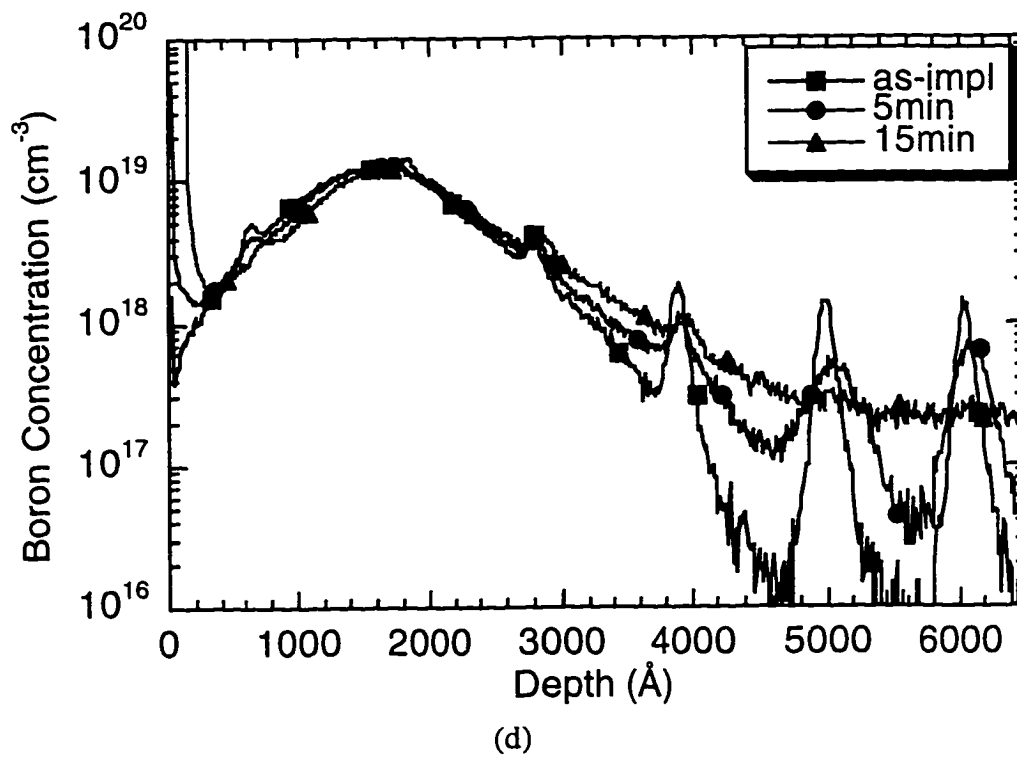
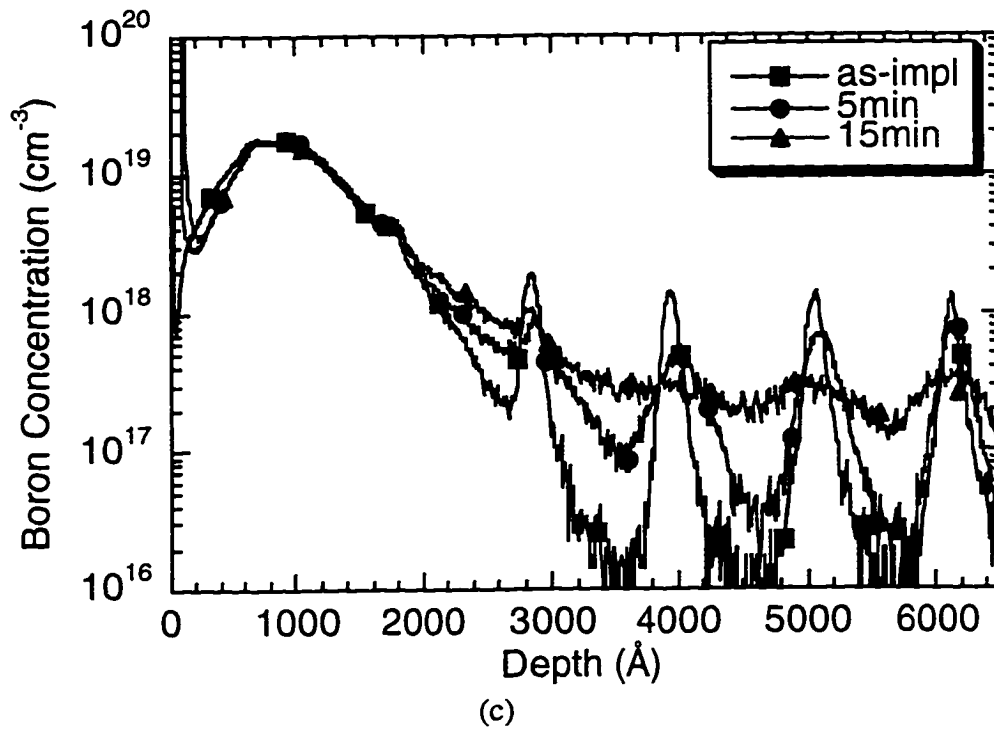


Figure 4.7. (continued)

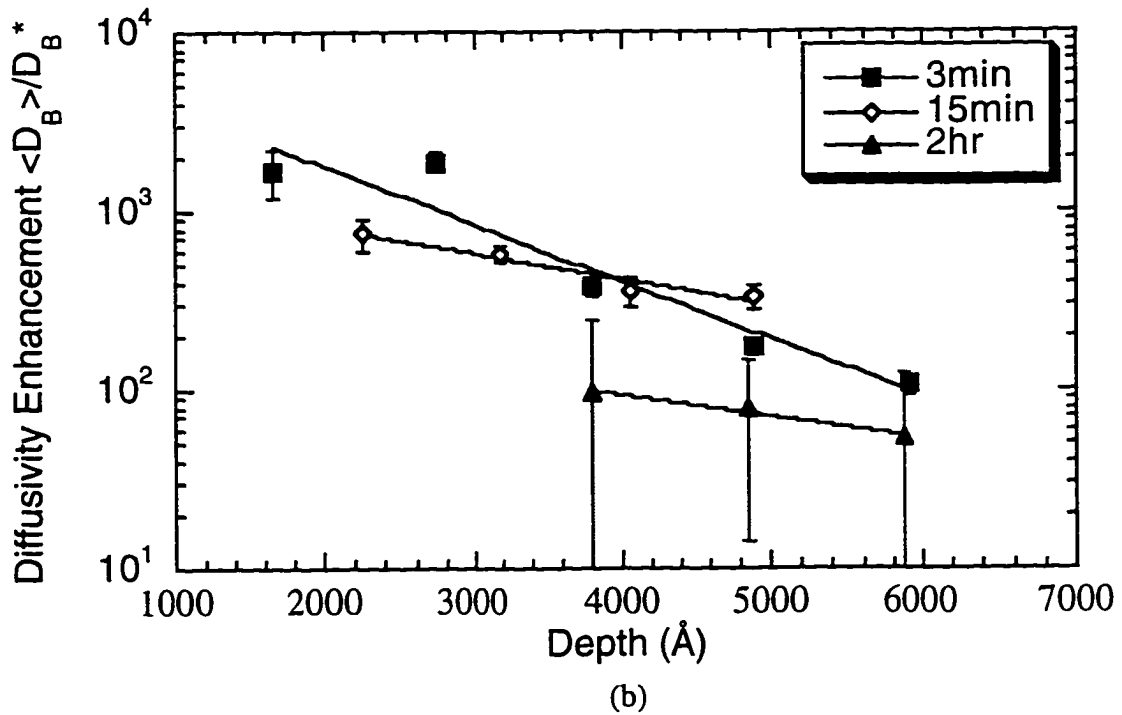
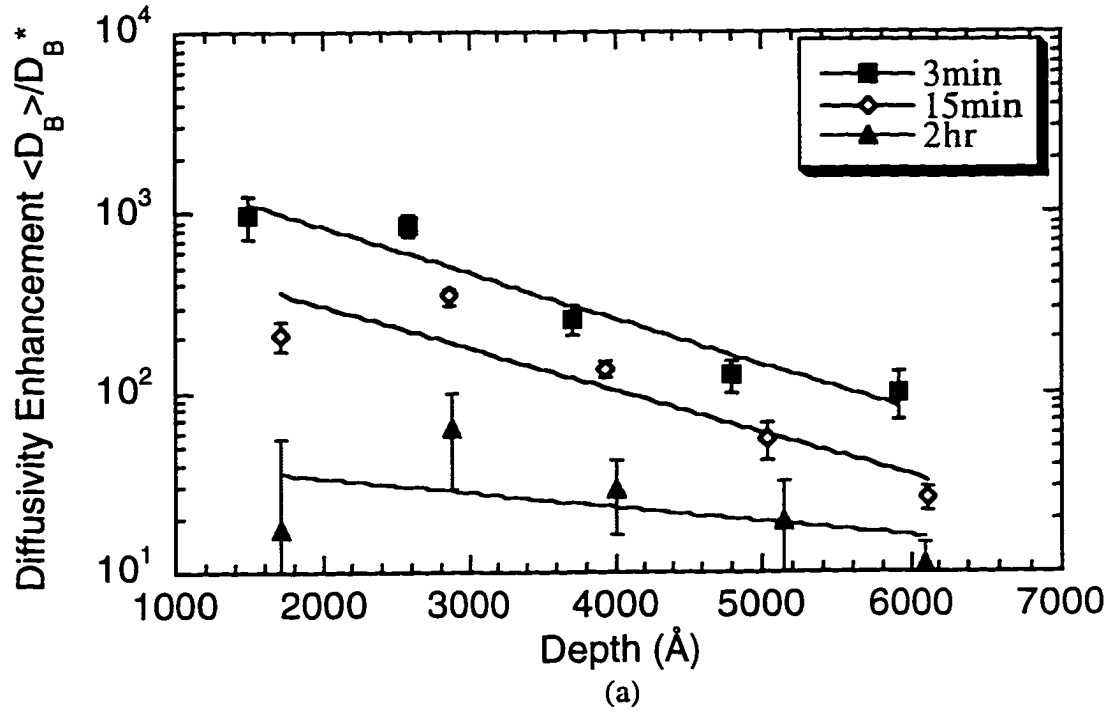


Figure 4.8. Enhancement of B diffusivity  $\langle D_B \rangle / D_B^*$  in  $B^+$  implanted Si superlattices at an energy of (a) 5keV, (b) 10keV, (c) 20keV and (d) 40keV, annealed at 750°C.

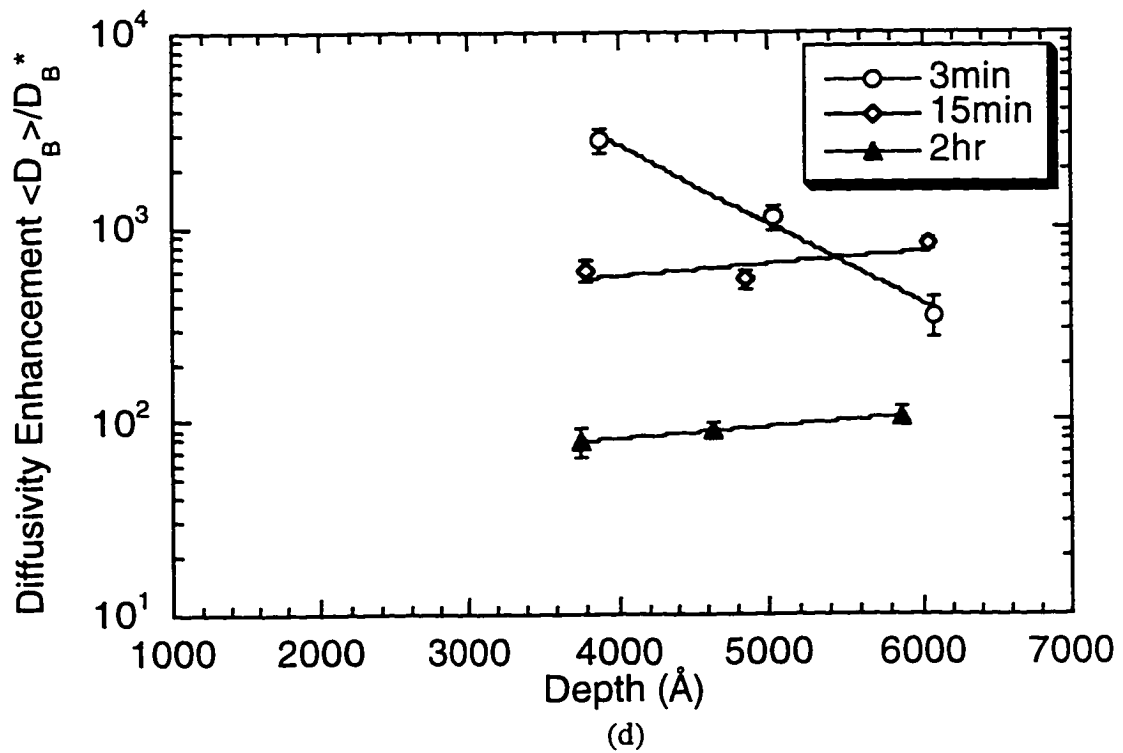
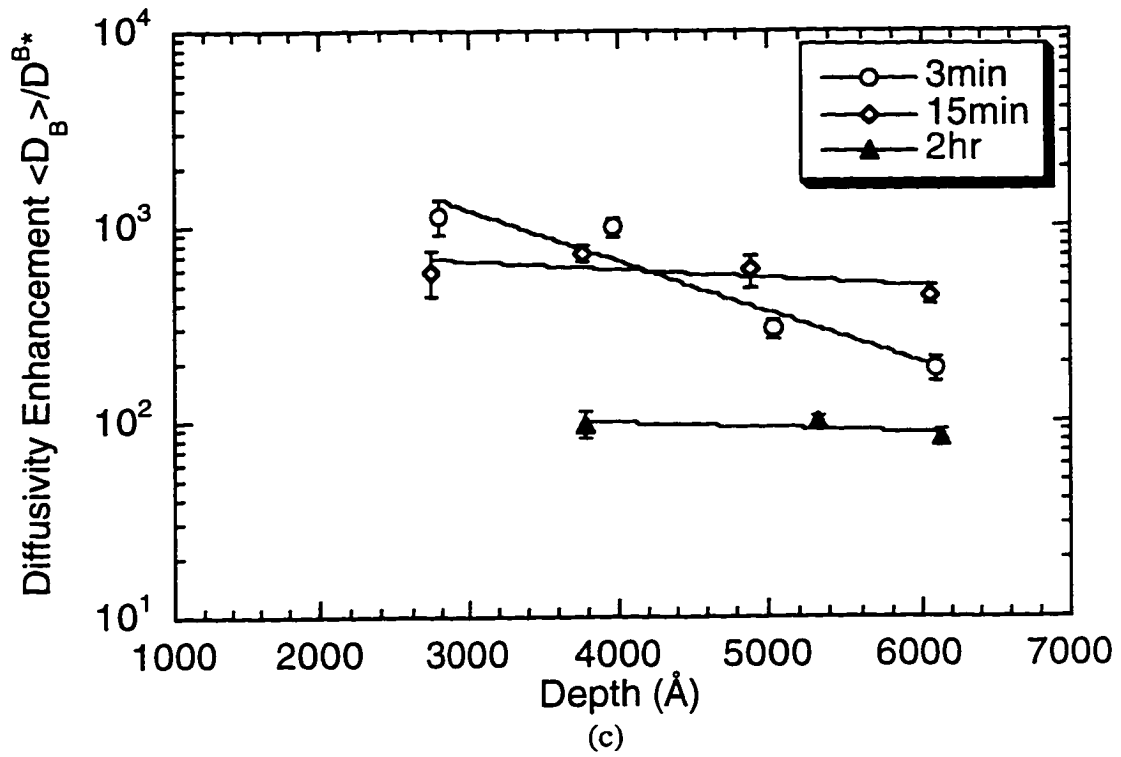


Figure 4.8. (Continued)

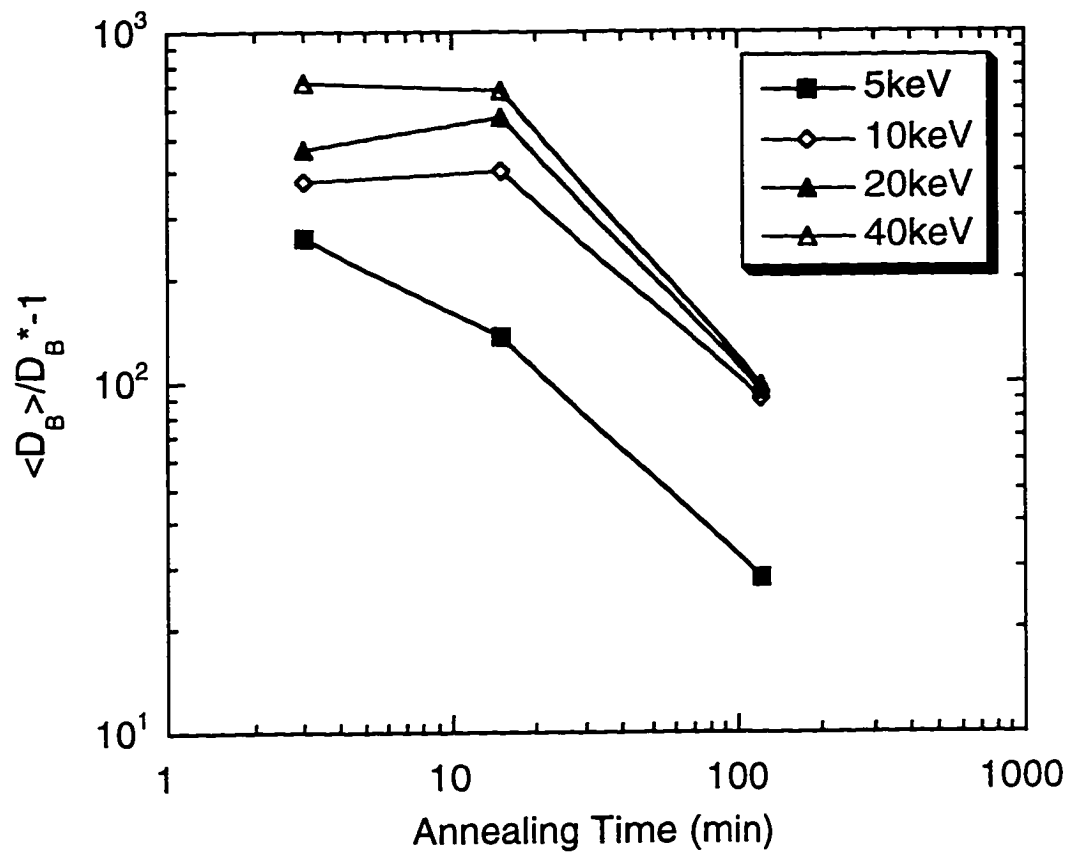


Figure 4.9. Enhancement of B diffusivity  $\langle D_B \rangle / D_B^*$  at a depth of 3600Å away from  $R_p$  as a function of annealing time for different implant energies.



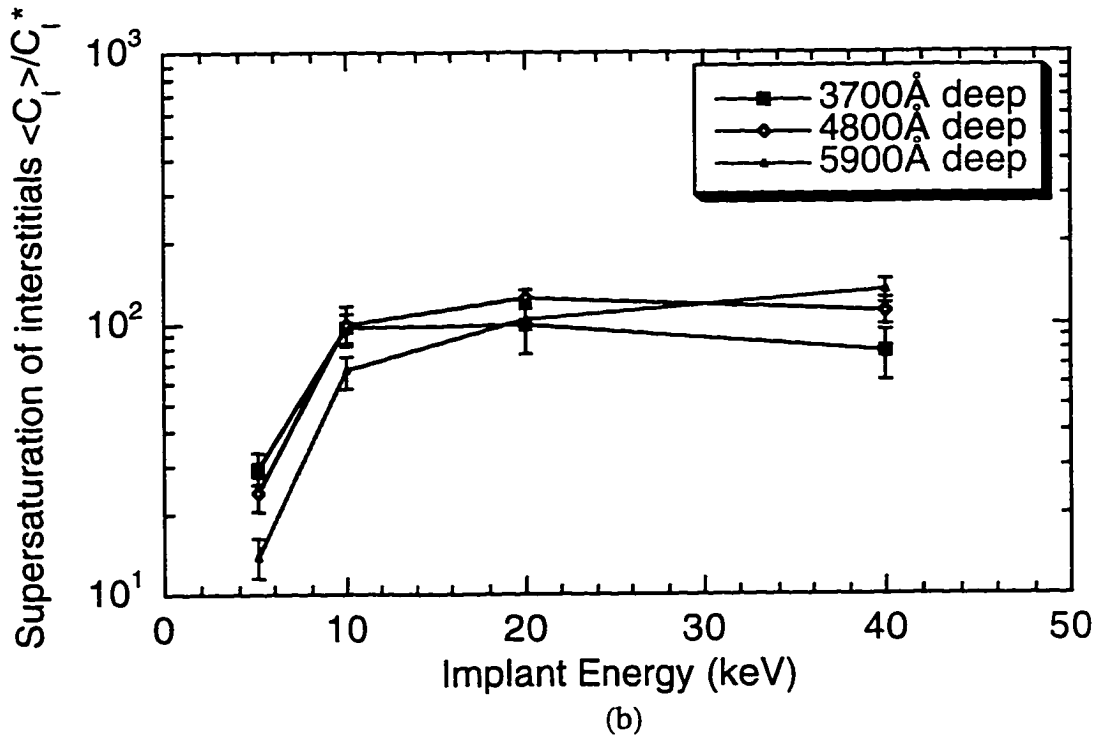
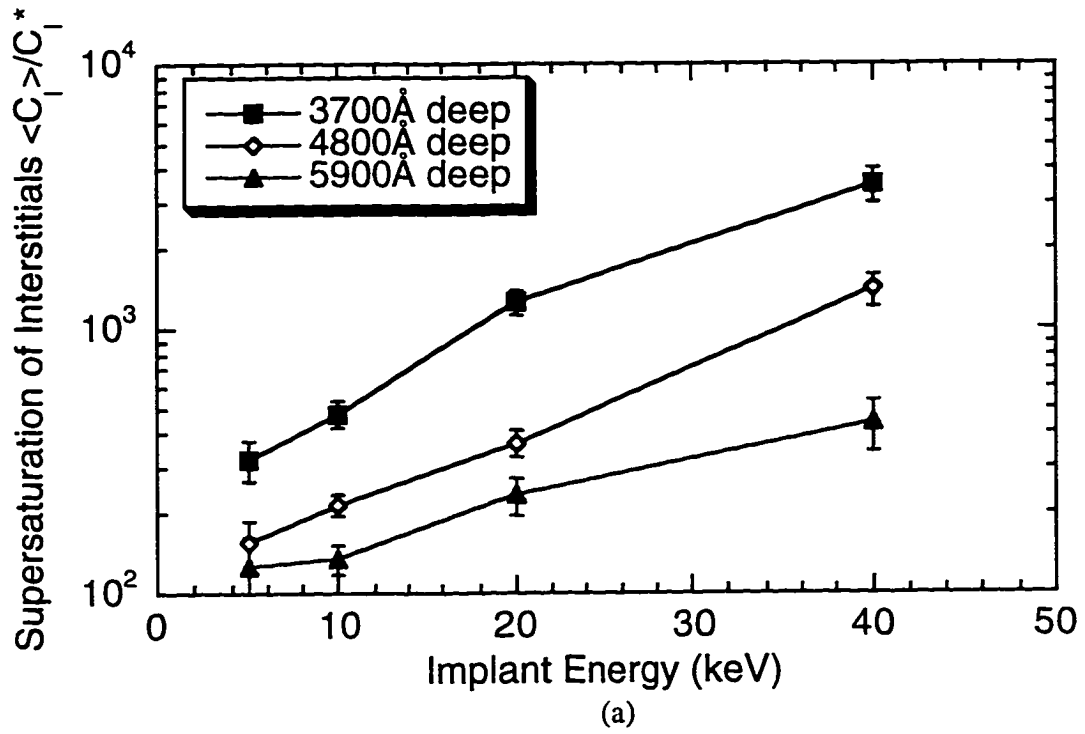


Figure 4.10. Supersaturation of interstitials as a function of implant energy after an anneal at 750°C for (a) 3min and (b) 2hrs.

## CHAPTER 5 THE INFLUENCE OF IMPLANT DOSE ON DEFECT BEHAVIOR AND TRANSIENT ENHANCED DIFFUSION

### 5.1 Overview

Implant dose is one of the most important parameters that strongly affect the form of implantation damage. Since transient enhanced diffusion is directly related to the damage created by the implantation, variation of implant dose is also expected to influence diffusion behavior.

For elements heavier than carbon, at low doses, the damage is in the form of point defects or small point defect clusters. At higher doses, extended defects begin to form. At very high doses, the surface of the substrate can be amorphized. The amorphization threshold depends on the implant condition and ion mass. Most of the experiments investigating TED due to implantation damage have used high dose amorphizing implants. In this case, the end-of-range damage can act as both a source and a sink of excess interstitials. For more information regarding the influence of implant damage on TED in amorphized sample, please refer to ref.17,111,131.

In the case of low dose non-amorphizing implants, Packan<sup>130</sup> studied boron diffusion in Si<sup>+</sup> implanted silicon with doses ranging from  $1 \times 10^{12} \text{ cm}^{-2}$  to  $2 \times 10^{14} \text{ cm}^{-2}$  at an

energy of 200 keV. Since the annealing temperatures were above 750°C and the annealing times were long enough to remove the {311} defects that would possibly be seen after low budget anneals, it was claimed that few extended defects were present in the sample. He studied the effect of varying Si implant dose on the diffusion behavior of a separately implanted deeper boron profile and found that the amount of diffusion increased with increasing dose but doubling the dose did not double the diffusion coefficient. This sub-linear dependence suggests a saturation of enhanced diffusion with increasing implant dose.

Solmi et al.<sup>132</sup> studied boron diffusion in 20 keV and 30 keV B<sup>+</sup> implanted silicon to doses from  $2 \times 10^{14} \text{ cm}^{-2}$  to  $5 \times 10^{15} \text{ cm}^{-2}$ . Thermal treatments were carried out at 800°C to 1000°C. They observed a reduced displacement of the profile for the higher dose associated with extended defect formation. The transient time for the enhanced diffusion was reduced by a factor of 2 for doses higher than  $5 \times 10^{14} \text{ cm}^{-2}$ . They attributed this reduction to the formation of extended defects at the projected range at these higher doses. The extended defects act as a sink for the interstitials, thus reducing the interstitial supersaturation level.

In this section we will discuss our study on boron diffusion after boron implantation at low and medium doses and anneals at a relatively low temperature (750°C). Different doses give rise to different types of extended defects, including {311} defects and sub-amorphization (type

I) dislocation loops. Our aim is to investigate the effect of varying dose on the defect behavior as well as on transient enhanced diffusion.

## 5.2 Implant Dose Effect on Defect Behavior

### 5.2.1 Experimental Procedure

To study the dose effect on defect evolution, we selected a single row from the implant matrix (see section 2.2). The implant energy was kept as 20 keV and the dose was varied from  $5 \times 10^{13} \text{ cm}^{-2}$  to  $1 \times 10^{15} \text{ cm}^{-2}$ . Subsequent furnace anneals were carried out in a nitrogen ambient for times between 5 min and 2 hr at 750°C. PTEM micrographs were taken under weak beam dark field imaging condition using g220 beam. The {311} defect density, average defect size, areal density of interstitials trapped by {311} defects and the defect distribution after annealing were measured from the TEM micrographs.

### 5.2.2 Defect Microstructure and Dissolution Process

PTEM micrographs of the defects after boron implantation at 20 keV to doses of  $1 \times 10^{14} \text{ cm}^{-2}$ ,  $5 \times 10^{14} \text{ cm}^{-2}$ , and  $1 \times 10^{15} \text{ cm}^{-2}$  and anneals at 750°C from 5 min to 2 hr are shown in Fig. 5.1 (a)~(c). No defects were observed for the lowest dose,  $5 \times 10^{13} \text{ cm}^{-2}$ , and therefore the pictures of these samples are not included. The  $1 \times 10^{14} \text{ cm}^{-2}$  implant contains only a small number of {311} defects after 5 min and 10 min

anneals and when annealing time is increased to 15 min, these defects completely dissolve. Defect behavior of the  $2 \times 10^{14} \text{ cm}^{-2}$  implant was shown in the last chapter (Fig. 4.1 (b)) and is left out here. A majority of  $\{311\}$  defects together with just a few dislocation loops are observed in the  $5 \times 10^{14} \text{ cm}^{-2}$  sample and the loop density increases for the  $1 \times 10^{15} \text{ cm}^{-2}$  implant. For each of the implants showing  $\{311\}$  defects, the number of the defects decreases with increasing annealing time. This dissolution process is much more rapid for a lower implant dose.

The areal density of interstitials trapped in  $\{311\}$  defects during the annealing process was quantified from the defect measurements and the results are shown in Fig. 5.2. Results for the  $1 \times 10^{14} \text{ cm}^{-2}$  implant are not included because the defect density is too low even after a 5min anneal. The emission of interstitials from  $\{311\}$  defects again shows an exponential time-dependence, which is much stronger for lower implant dose. After a 30 min anneal,  $\{311\}$  defects in the  $2 \times 10^{14} \text{ cm}^{-2}$  implant dissolved to a very low density. The number of remaining trapped interstitials is about  $7.7 \times 10^{11} \text{ cm}^{-2}$ . If the dose is increased to  $5 \times 10^{14} \text{ cm}^{-2}$ , after an anneal of 1hr, there is still an areal interstitial density of about  $1.7 \times 10^{13} \text{ cm}^{-2}$ . If we compare Fig. 5.2 with Fig. 4.2, we will find that doubling the dose decreased the dissolution rate much more than doubling the energy. Since the number of displaced atoms per implanted ion is proportional to the implant energy, such an observation might

support the idea of "plus 1" model over the idea of collision cascade as the source of the interstitials. However, this time constant increase with increasing dose seems to become less pronounced when the dose is increased further. From  $2 \times 10^{14} \text{ cm}^{-2}$  to  $5 \times 10^{14} \text{ cm}^{-2}$ , the time constant changes from 424 sec to 3029 sec. But from  $5 \times 10^{14} \text{ cm}^{-2}$  to  $1 \times 10^{15} \text{ cm}^{-2}$ , the time constant only changes from 3029 sec to 4604 sec. As we discussed in Chapter 2, the threshold dose for the formation of stable sub-amorphization (type I) dislocation loops lies somewhere between  $2 \times 10^{14} \text{ cm}^{-2}$  and  $5 \times 10^{14} \text{ cm}^{-2}$  at 20 keV (see Table 2.2). The presence of loops seems to expedite the dissolution process of  $\{311\}$  defects. Interstitials emitted from  $\{311\}$  defects will feed the dislocation loops and the sink effect of loops makes the  $\{311\}$  dissolution faster.

By measuring the loop size on the PTEM micrographs, the concentration of interstitials trapped by dislocation loops was obtained. By assuming a circular loop, the radius of each loop or partial loop was measured along its longest axis and the corresponding loop area was calculated. The concentration of atoms bound by loops could be estimated by multiplying the fraction of loop area by the atomic density of atoms on the  $\{111\}$  plane, which is  $1.6 \times 10^{15} \text{ cm}^{-2}$ .

The density of interstitials trapped in  $\{311\}$  defects and dislocation loops after anneals for 5 min and 2 hr at  $750^\circ\text{C}$  as a function of implant dose is shown in Fig. 5.4. We can see that the density of interstitial in  $\{311\}$  defects or

loops is much less than the implant dose. Assuming that the net number of excess interstitials is roughly equal to the dose (plus 1 model) and the missing interstitials are all trapped in sub-microscopic boron interstitial complexes, including mobile B-I pairs and immobile B-I clusters, then the percentage of the interstitials trapped in these boron interstitial complexes after a 5 min anneal at 750°C is 87.5%, 87.8% and 88.6% for the  $2 \times 10^{14} \text{ cm}^{-2}$ ,  $5 \times 10^{14} \text{ cm}^{-2}$  and  $1 \times 10^{15} \text{ cm}^{-2}$  implant respectively. Within the experimental error range we can say that this percentage does not change with implant dose. This is different from the energy dependence which we discussed in Chapter 4. The percentage of interstitials trapped in boron interstitial complexes decreases with increasing energy because of the lower boron peak concentration due to the spreading out of the dopant profile. Here, when implant dose is increased, both the boron peak concentration and the implant damage increase proportionally. As a result more boron interstitial complexes and more {311} defects/loops are formed and the percentage of interstitials trapped in B-I complexes versus {311}s/loops stays constant. This argument, however, cannot be used to predict the phenomenon in a sample without {311} defects or loops.

It is interesting to notice from Fig. 5.4 how interstitials re-distribute themselves during the annealing. The {311} defects for the  $2 \times 10^{14} \text{ cm}^{-2}$  implant dissolve almost completely after 2 hr anneal at 750°C. The trapped

interstitials either diffuse to the surface or into the bulk. For the  $5 \times 10^{14} \text{ cm}^{-2}$  implant, the number of interstitials released from {311} defects between 5 min to 2 hr is higher than that trapped in the loops. Because of the small density of the loops they do not act as a very strong interstitial sink. While for the  $1 \times 10^{15} \text{ cm}^{-2}$  implant, loops trap more interstitials than those released from {311} defects. Although the number of interstitials introduced into the bulk is the highest for this dose, there is no dramatic increase in transient diffusion compared with a lower dose (e.g.  $2 \times 10^{14} \text{ cm}^{-2}$ ) due to the presence of larger density of interstitial traps--dislocation loops. This will be discussed in detail later.

### 5.2.3 Defect Density, Size and Distribution during Annealing

The {311} defect density of different implants as a function of annealing time measured from PTEM images is shown in Fig. 5.5. For all annealing times, the defect density increases with increasing dose. After a 5 min anneal, the {311} defect density is about  $3.3 \times 10^{10} \text{ cm}^{-2}$  for the  $2 \times 10^{14} \text{ cm}^{-2}$  implant, and about  $1.1 \times 10^{11} \text{ cm}^{-2}$  for the  $1 \times 10^{15} \text{ cm}^{-2}$  implant. For each implant dose, the defect density decreases with increasing annealing time, with the decrease occurring faster for a lower dose. The reason for the strong dose dependence of defect density might be that in a sample implanted with higher dose, the interstitial supersaturation level is higher. As a result, the number of



small defect nuclei is much larger during the initial defect formation process. Subsequently more defects are grown from these nuclei and therefore more defects are observed in a higher dose implant.

The average {311} defect size as a function of annealing time for different implant doses is shown in Fig. 5.6. The average defect size increases with annealing time. For a particular time, the defect size is larger for a higher dose. After an anneal of 15 min, the  $2 \times 10^{14} \text{ cm}^{-2}$  implant shows an average defect size of about 517 Å, while for the  $1 \times 10^{15} \text{ cm}^{-2}$  implant, it is about 613 Å. Unlike the defect density dependence, the size dependence on dose is not very strong. This is not surprising because the total number of interstitials introduced into the substrate represents the product of the defect density and the defect size. Given a fixed amount of total interstitials, a strong dose dependence of the defect density must be accompanied by a weak dose dependence of the defect size.

The size distribution of {311} defects after anneals at 750°C for various times for  $5 \times 10^{14} \text{ cm}^{-2}$  and  $1 \times 10^{15} \text{ cm}^{-2}$  implants is shown in Fig. 5.7 (a) and (b). For each implant we can see the same trend as we observed in the previous chapters: a shift of the average {311} defect size to a larger value and a decrease of the defect density at a particular size with increasing annealing time. The decreasing defect density and the increasing defect size are the characteristics of the Ostwald ripening process. The

decreasing interstitial density (Fig. 5.2) and decreasing defect density are the characteristics of defect dissolution process. The two coupled processes give rise to the defect distribution shown in Fig. 5.7. If we compare Fig. 5.7(a) and (b) with Fig. 4.6(b) (the size distribution of  $2 \times 10^{14} \text{ cm}^{-2}$  implant), we see that the standard deviation of the size distribution increases as dose increases. This again might be due to the larger number of defect nuclei in the sample implanted with higher dose. Some nuclei might grow faster than the others which results in more possible defect sizes than the sample with fewer nuclei.

As a summary, the  $\{311\}$  defect microstructure and annealing behavior as a function of implant dose ( $5 \times 10^{13} \text{ cm}^{-2}$  ~  $1 \times 10^{15} \text{ cm}^{-2}$ ) have been studied using TEM. After anneals at  $750^\circ\text{C}$  for times ranging from 5 min to 2 hr, no  $\{311\}$  defects are observed in the  $5 \times 10^{13} \text{ cm}^{-2}$  implant, a few in the  $1 \times 10^{14} \text{ cm}^{-2}$  implant and more in the  $2 \times 10^{14} \text{ cm}^{-2}$  implant. A majority of  $\{311\}$  defects and a few dislocation loops are present at the higher doses. Assuming a valid "plus 1" model, the number of interstitials bound by boron interstitial complexes is estimated to be about 88% of the implant dose for  $2 \times 10^{14} \text{ cm}^{-2}$ ,  $5 \times 10^{14} \text{ cm}^{-2}$  and  $1 \times 10^{15} \text{ cm}^{-2}$  implants after an anneal for 5 min. The  $\{311\}$  defect dissolution process shows a smaller time constant for a lower dose. Dislocation loops expedite  $\{311\}$  defect dissolution at doses  $\geq 5 \times 10^{14} \text{ cm}^{-2}$  by acting as an effective interstitial sink and therefore reducing the time constant increase rate

of defect dissolution. The interstitial sink effect in the  $1 \times 10^{15} \text{ cm}^{-2}$  implant is more prominent than that in the  $5 \times 10^{14} \text{ cm}^{-2}$  implant due to the higher loop density resulted from the higher dose. Both defect density and average defect size increases when implant dose increases. The evolution of {311} defects indicates an Ostwald ripening process and a defect dissolution process. The standard deviation of defect size distribution is larger for higher doses.

### 5.3 Implant Dose Effect on Transient Enhanced Diffusion

#### 5.3.1 Experimental Procedure

It is critical to understand how all the defect evolutionary changes affect the transient enhanced diffusion process. In order to study this again we separated the implant profile from the diffusion marker layer. A thin  $\delta$ -doping boron marker layer was used to monitor boron diffusion behavior after ion implantation and annealing. The layer was grown via atmospheric pressure chemical vapor deposition (APCVD) on p-type (100) Czochralski-grown silicon substrate, followed by growth of an overlayer of approximately 7000 Å of undoped silicon. The full width at half maximum (FWHM) of the boron spike is about 500 Å and peak concentration is about  $2 \times 10^{18} \text{ cm}^{-3}$ . This low concentration allows dopant diffusion to remain in the intrinsic regime at our processing temperature and also reduces boron interstitial cluster formation in the doping spike. The as-grown wafers were pre-

annealed in a nitrogen ambient at 800°C for 1hr to remove the excess point defects introduced by the APCVD process. The wafers were then implanted with 20 keV boron ions to doses of  $5 \times 10^{13} \text{ cm}^{-2}$ ,  $2 \times 10^{14} \text{ cm}^{-2}$  and  $1 \times 10^{15} \text{ cm}^{-2}$ . Subsequent anneals were performed in nitrogen at 750°C for 15 min, 30 min, 1 hr, 2 hr and 4 hr. SIMS analysis was performed on the CAMECA IMS4f system. The parameters used during the SIMS analysis were the same as discussed in section 3.3.1. The dopant profiles were then imported into FLOOPS and the diffusivity enhancement was extracted for each anneal.

### 5.3.2 Dopant Diffusion Behavior

SIMS profiles of boron in the as-grown and pre-annealed samples as well as in the implanted and annealed samples are shown in Fig. 5.8(a)~(d). The small displacement of the profile of the pre-annealed sample with respect to that of the as-grown sample is believed to be due to boron intrinsic diffusion. The buried boron spike in the  $5 \times 10^{13} \text{ cm}^{-2}$  implanted sample shows an enhanced diffusion but the profile displacement is smaller compared with those at higher doses. The 30min annealed profile of the  $2 \times 10^{14} \text{ cm}^{-2}$  implanted sample shows an enhanced diffusion to a similar degree as that of the  $1 \times 10^{15} \text{ cm}^{-2}$  implant. But the profile after a 4hr anneal shows a smaller enhancement than that at  $1 \times 10^{15} \text{ cm}^{-2}$ . Besides the buried boron spike, the tail of implanted boron profile also shows an enhanced diffusion in each sample. The peak of this implanted profile, however, is clustered and

therefore stays immobile for the two higher doses. The breaking point between the mobile and immobile part is at a concentration of about  $3 \times 10^{18} \text{ cm}^{-3}$ , the same for both implants and for every anneal.

The SIMS data of the control and implanted samples were imported into FLOOPS. Diffusivity enhancement  $\langle D_B \rangle / D_B^*$  was obtained by matching the initial profile with the target profile assuming an intrinsic diffusivity with the form  $D_B^* = 0.757 \exp(-3.46 \text{ eV} / kT)$  (eq.(3.8)). We extracted the enhancement factor for control sample 1 (as-grown plus 800°C 1 hr anneal), control sample 2 (pre-anneal plus 750°C 1 hr anneal) and control sample 3 (pre-anneal plus 750°C 4 hr anneal). The purpose of control sample 1 was to examine how much enhancement would come from the excess interstitials induced by the APCVD growth process. The purpose of control samples 2 and 3 was to test whether the nitrogen ambient indeed functions as an inert ambient. The enhancement factor for these three samples was 4.1, 4.9 and 4.7 respectively. This small enhancement might be due to the residue oxygen in the nitrogen ambient. However, it might also just result from the experimental errors, including the SIMS depth error range of 5% and the annealing temperature accuracy of  $\pm 10^\circ\text{C}$ . The number of excess interstitials introduced by the APCVD process is obviously not high enough to cause much enhanced diffusion.

Fig.5.9 is a plot of the time-averaged diffusivity enhancement  $\langle D_B \rangle / D_B^*$  of the buried boron spike as a function

of annealing time for different implant doses after each anneal. Before the simulation, dose normalization was conducted on the spike for the as-implanted and annealed samples regardless of the small influx of boron from the surface implant into the spike region which actually violates the dose conservation. From Fig.5.9 we can see that the value of  $\langle D_B \rangle / D_B^*$  decreases with increasing annealing time for each implant. At all annealing times,  $\langle D_B \rangle / D_B^*$  is lower for the  $5 \times 10^{13} \text{ cm}^{-2}$  implant than the two higher doses. After an anneal at  $750^\circ\text{C}$  for 4 hr,  $\langle D_B \rangle / D_B^*$  increases from 409 for the  $5 \times 10^{13} \text{ cm}^{-2}$  implant to 854 for the  $2 \times 10^{14} \text{ cm}^{-2}$  implant. For B diffusion,  $\langle D_B \rangle / D_B^*$  is proportional to the interstitial supersaturation level  $\langle C_I \rangle / C_I^*$ . If the "plus 1" model is valid, the difference in  $\langle D_B \rangle / D_B^*$  simply should be four times. Since only a two times increase is seen yet all the  $\{311\}$  defects have dissolved, stable B-I cluster formation in the  $2 \times 10^{14} \text{ cm}^{-2}$  implant could account for the small increase in  $\langle D_B \rangle / D_B^*$ .

### 5.3.3 TED Saturation at Higher Dose

It is interesting to notice that  $\langle D_B \rangle / D_B^*$  is close for the two higher doses,  $2 \times 10^{14} \text{ cm}^{-2}$  and  $1 \times 10^{15} \text{ cm}^{-2}$ . As we discussed before, the formation threshold for the sub-amorphization dislocation loops lies between doses of  $2 \times 10^{14} \text{ cm}^{-2}$  and  $5 \times 10^{14} \text{ cm}^{-2}$ . When the dose reaches  $1 \times 10^{15} \text{ cm}^{-2}$ , quite a few loops form after annealing. These loops can act as a sink for interstitials released from

either {311} defects or invisible mobile boron interstitial pairs. Besides this trapping effect of interstitials by loops, more interstitials might be trapped in the boron interstitial clusters in the implant damage peak region because more clusters are formed in the higher dose implant. As a result of both trapping effects, the number of interstitials available for TED is reduced and so is the enhancement of diffusion. This can explain why we do not observe a decrease in  $\langle D_B \rangle / D_B^*$  for times  $\leq 1$  hr even though the dose is increased four times.

Another explanation of the TED saturation behavior with increasing dose was proposed by Griffin et al<sup>133</sup>. They claimed that this saturation can occur if most of the dopant atoms are already pushed into a mobile state so that more damage produces no increase in diffusivity. They used a simple chemical reaction model to explain the phenomena. The interaction of a substitutional dopant atom  $B_S$  with a free interstitial  $I$  to produce a mobile  $B_I$  can be described by



If this reaction is in equilibrium, then we have

$$B_I = K_{eq} B_S I \quad (5.1)$$

where  $K_{eq}$  is the equilibrium reaction constant. The substitutional  $B_S$  and mobile  $B_I$  are related to the total dopant by

$$B_T = B_S + B_I \quad (5.2)$$

Using eq.(5.1) and (5.2) we have

$$B_I = B_T K_{eq} I / (1 + K_{eq} I) \quad (5.3)$$

The above equation shows that for large damage dose,  $B_I$  approaches a maximum value of  $B_T$ . Further increase in the dose will not produce more  $B_I$ . Effectively all the B is paired and further increase in I do not enhance  $D_B$ .

At this time we do not know which mechanism, the loop/cluster trapping of interstitials or dopant interstitial pair saturation, is valid in our case. Quantification of the interstitials in the clustered region will shed light on this issue. If the extra interstitials due to the dose increase from  $2 \times 10^{14} \text{ cm}^{-2}$  to  $1 \times 10^{15} \text{ cm}^{-2}$  are all trapped in the loops/clusters, then the first mechanism might dominate. Otherwise, we should also consider the second mechanism. For our APCVD grown boron spike, the area integration under the spike shows a dose of  $1 \times 10^{13} \text{ cm}^{-2}$ . Because this is only 5% of the  $2 \times 10^{14} \text{ cm}^{-2}$  dose and 1% of the  $1 \times 10^{15} \text{ cm}^{-2}$  dose, it is quite possible that dopant interstitial pair saturation is reached. But we also observed more clustering for the higher dose in Fig. 5.7 and the trap of interstitials by loops in Fig. 5.4. Both mechanisms might function together and either one of them could give rise to the current diffusion behavior.

The diffusion length of the buried boron spike  $\sqrt{\langle D_B \rangle t}$  as a function of annealing time for each implant is shown in Fig. 5.10. The dots are the data points and the lines are the fits in the form of  $a\sqrt{1 - \exp(-t/\tau)}$ , where  $a$  and  $\tau$  are constants and  $t$  is the annealing time (please refer to



Chapter 3 for the derivation). Another data point ( $t=0$ ,  $\sqrt{\langle D_B \rangle t}=0$ ) is added on each set of data for the convenience of fitting. It is obvious that TED saturates after a shorter time (around 16 min) at the low dose of  $5 \times 10^{13} \text{ cm}^{-2}$  than at higher doses (37 min at  $2 \times 10^{14} \text{ cm}^{-2}$  and 4 min at  $1 \times 10^{15} \text{ cm}^{-2}$ ). The diffusion length at  $2 \times 10^{14} \text{ cm}^{-2}$  dose is very close to that at  $1 \times 10^{15} \text{ cm}^{-2}$  dose due to the factors we discussed above.

A similar dose dependent diffusion behavior was observed by Packan<sup>130</sup>. As was mentioned in the overview section in this chapter, the diffusion of a buried implanted boron profile was studied by using  $\text{Si}^+$  implanted silicon with doses ranging from  $1 \times 10^{12} \text{ cm}^{-2}$  to  $2 \times 10^{14} \text{ cm}^{-2}$  at an energy of 200 keV. He presented the diffusion length versus annealing time plots for doses of  $5 \times 10^{13} \text{ cm}^{-2}$ ,  $1 \times 10^{14} \text{ cm}^{-2}$  and  $2 \times 10^{14} \text{ cm}^{-2}$  after anneals at  $750^\circ\text{C}$ ,  $800^\circ\text{C}$  and  $850^\circ\text{C}$  for various times. The diffusion length for the  $5 \times 10^{13} \text{ cm}^{-2}$  implant is the lowest for all the anneals. The diffusion lengths for the  $1 \times 10^{14} \text{ cm}^{-2}$  and the  $2 \times 10^{14} \text{ cm}^{-2}$  implants stay about the same for  $t \leq 330 \text{ min}$  at  $750^\circ\text{C}$ ,  $t \leq 60 \text{ min}$  at  $800^\circ\text{C}$  and  $t \leq 10 \text{ min}$  at  $850^\circ\text{C}$ . After these times higher dose gives rise to larger diffusion length. Comparing our results with Packan's, it is reasonable to believe that for 200 keV  $\text{Si}^+$  implantation, the threshold dose for the formation of sub-amorphization dislocation loops is between  $1 \times 10^{14} \text{ cm}^{-2}$  and  $2 \times 10^{14} \text{ cm}^{-2}$ . During the early stage of annealing these loops absorb interstitials and reduce the enhancement of boron diffusion.

Later on these trapped interstitials are released from the loops and make contribution to boron diffusion.

Interstitials are easier to escape the trap of dislocation loops at higher temperatures and therefore it takes shorter time to observe a larger diffusion at a higher dose.

Our results are also comparable with those of Solmi et al.<sup>132</sup>. They used 20 keV to 30 keV B<sup>+</sup> implantations to doses from  $2 \times 10^{14} \text{ cm}^{-2}$  to  $5 \times 10^{15} \text{ cm}^{-2}$  to study the diffusion of the B implant itself. They observed a less displacement in the profile tail region for the higher doses ( $> 5 \times 10^{14} \text{ cm}^{-2}$  compared with  $< 5 \times 10^{14} \text{ cm}^{-2}$ ) within a time range of 5min to 2hrs at 800°C. The displacements of the  $2 \times 10^{15} \text{ cm}^{-2}$  and the  $5 \times 10^{15} \text{ cm}^{-2}$  implants are very close. They attributed the reduction of diffusion to the extended defects which might act as a sink of the free interstitials.

In summary,  $\delta$ -doping boron marker layer was used to study dopant diffusion behavior after B<sup>+</sup> implantation at 20 keV to various doses. This APCVD grown layer acted as a sensitive diffusion monitor for diffusion because of the steep dopant gradient. The doses chosen cover the transition regions from sample with no {311} defects ( $5 \times 10^{13} \text{ cm}^{-2}$ ), to that with {311} defects ( $2 \times 10^{14} \text{ cm}^{-2}$ ), then to that with both dislocation loops and {311} defects ( $1 \times 10^{15} \text{ cm}^{-2}$ ). The lowest dose shows the lowest diffusion enhancement and the smallest diffusion length for all the anneals. The diffusion enhancement and the diffusion length saturate for doses above  $2 \times 10^{14} \text{ cm}^{-2}$ . There are two mechanisms which can both explain

this saturation effect. One is that dislocation loops and more B-I clusters form at the highest dose, which act as a sink of interstitials for a limited period of time, during which dopant diffusion is reduced, and after which interstitials are emitted again and give rise to more diffusion. The other is that all the boron atoms are paired with interstitials and more interstitials would not cause any further diffusion. Our results are comparable to those reported by Packan, where lower dose  $\text{Si}^+$  implantation was used to examine the dose dependence of dopant diffusion, and to those of Solmi et al., where higher dose  $\text{B}^+$  implantation was used and the formation of dislocation loops was claimed to result in a reduction in TED.

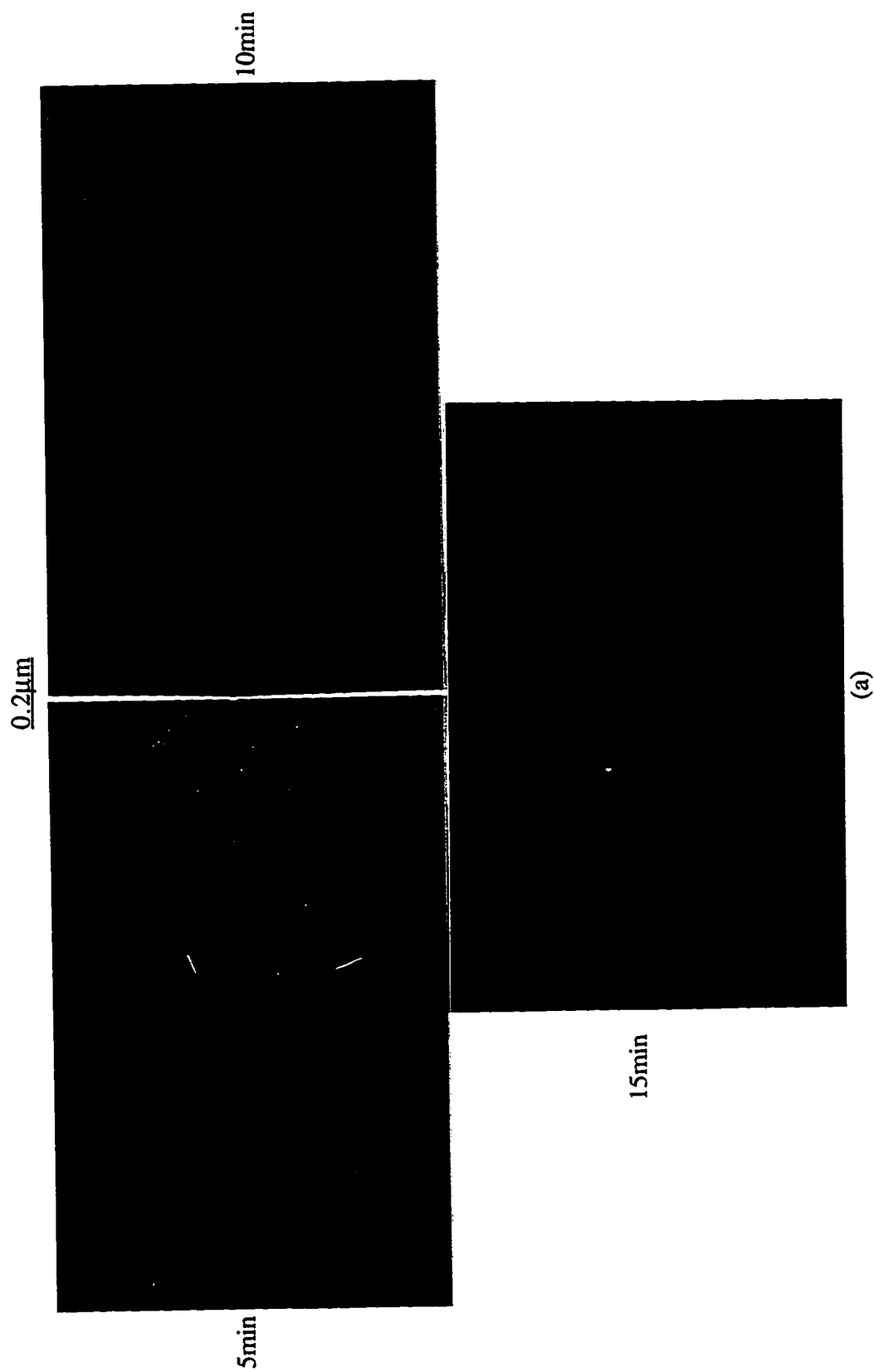


Figure 5.1. Weak beam dark field PTM ( $g_{220}$ ) micrographs of  $20\text{keVcm}^2$   $\text{B}^+$  implanted Si to a dose of (a)  $1 \times 10^{14}\text{cm}^{-2}$ , (b)  $5 \times 10^{14}\text{cm}^{-2}$  and (c)  $1 \times 10^{15}\text{cm}^{-2}$ .

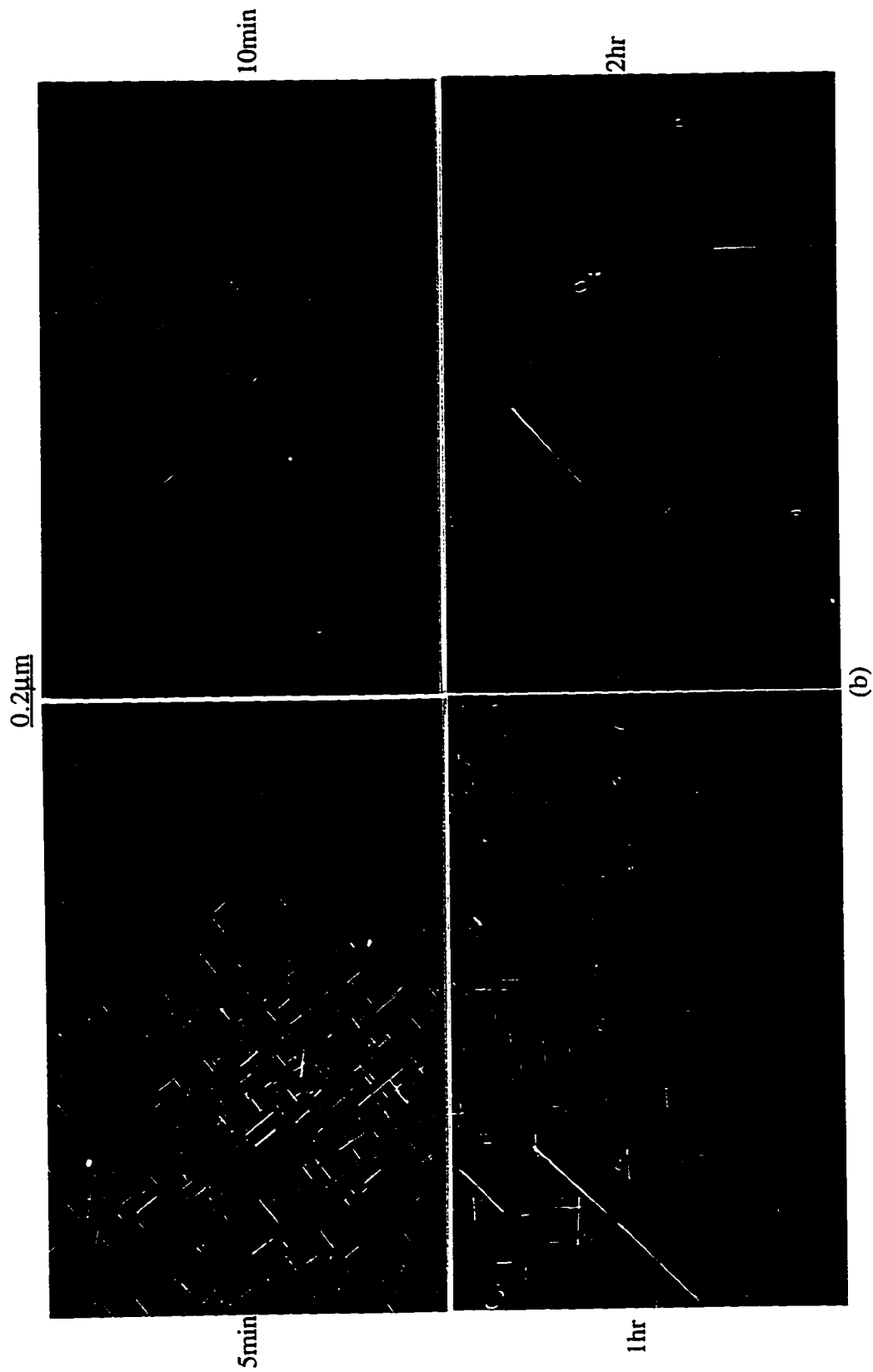
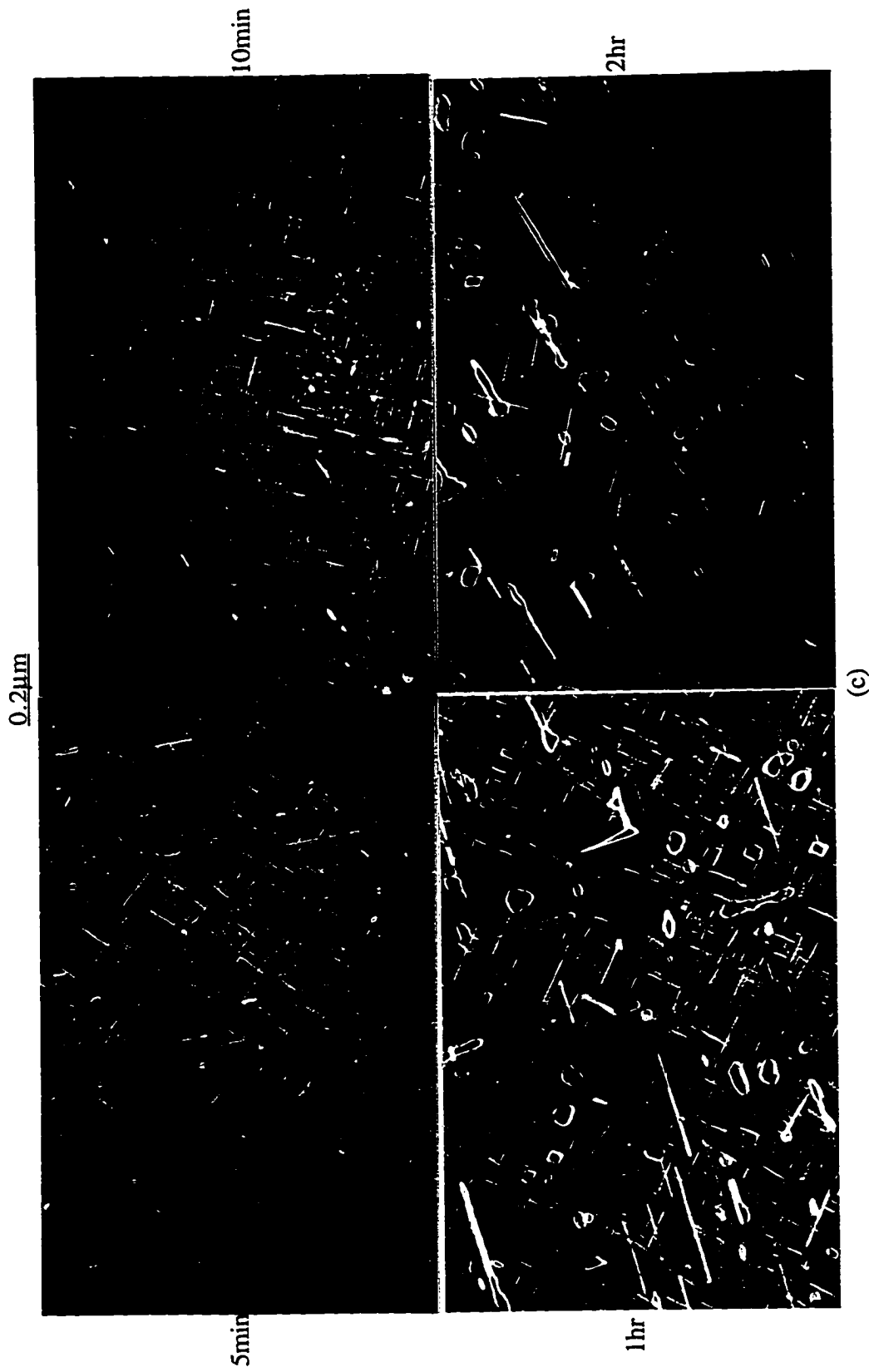


Figure 5.1 (Continued)



(c)

Figure 5.1 (Continued)

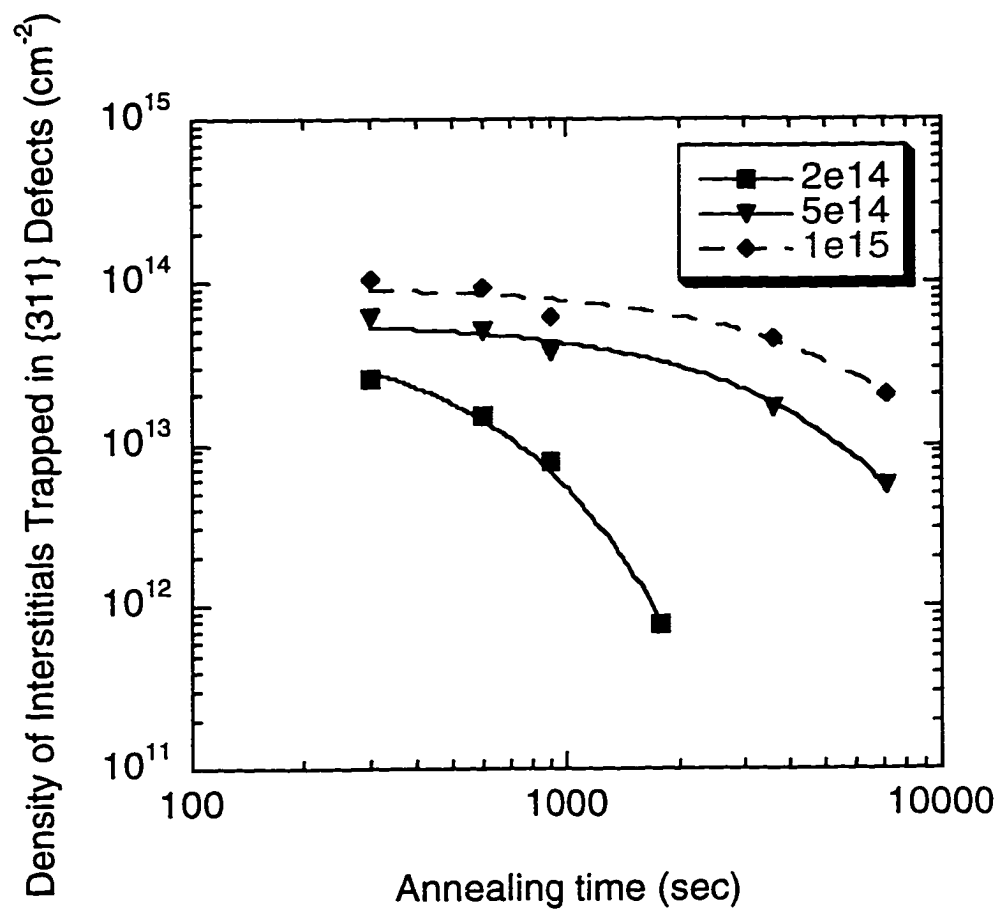


Figure 5.2. The exponential decay of interstitials trapped in {311} defects in 20keV B<sup>+</sup> implanted Si to various doses.

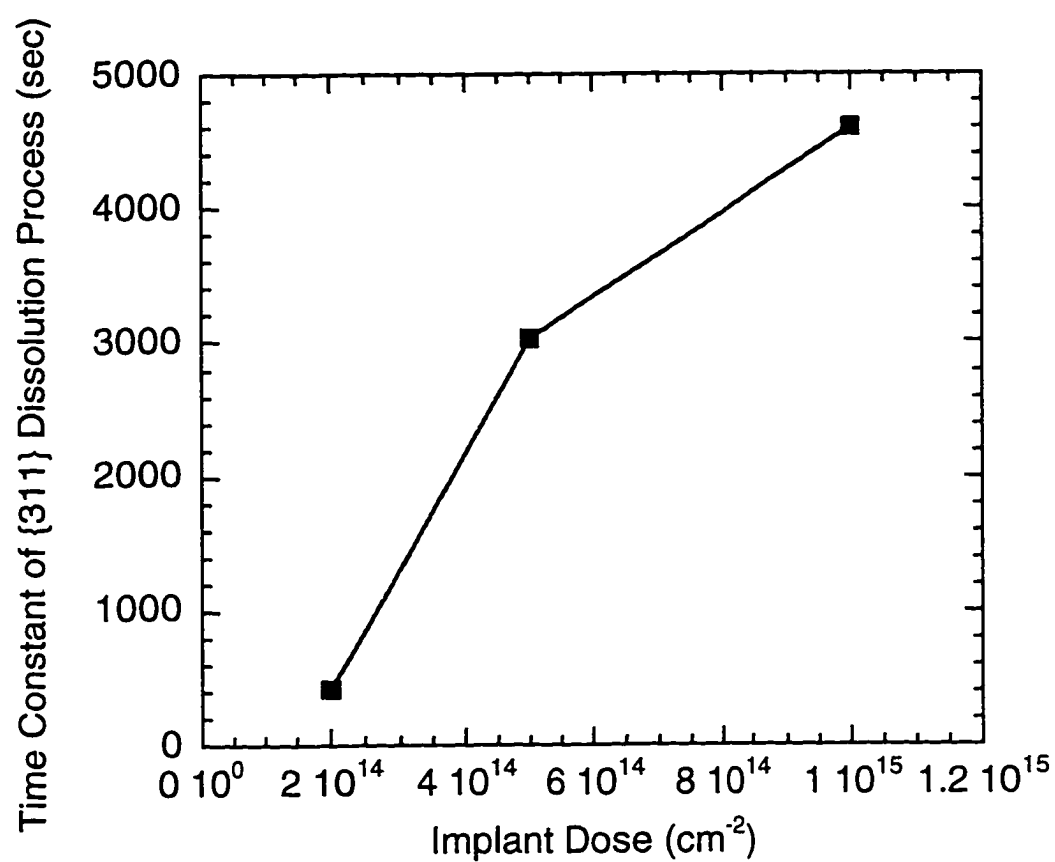


Figure 5.3. Time constant of {311} dissolution process as a function of implant dose, annealed at 750°C.



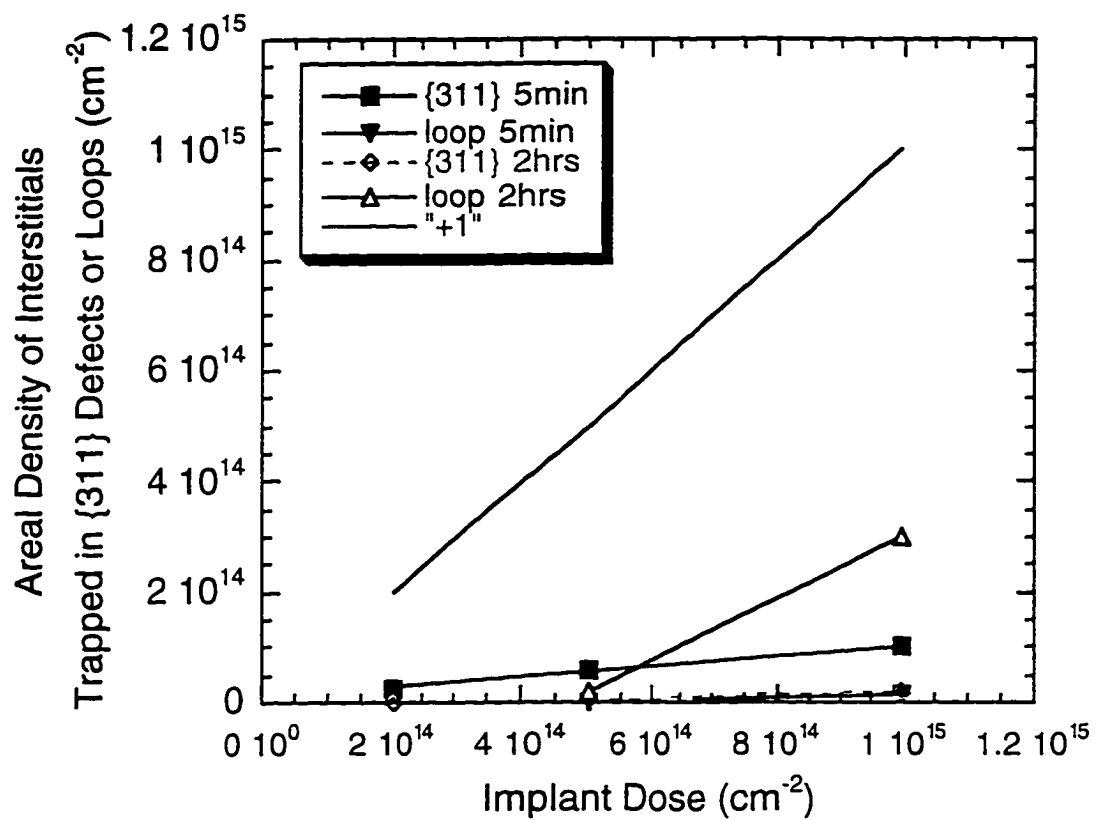


Figure 5.4. Areal density of interstitials trapped in {311} defects and dislocation loops as a function of dose.

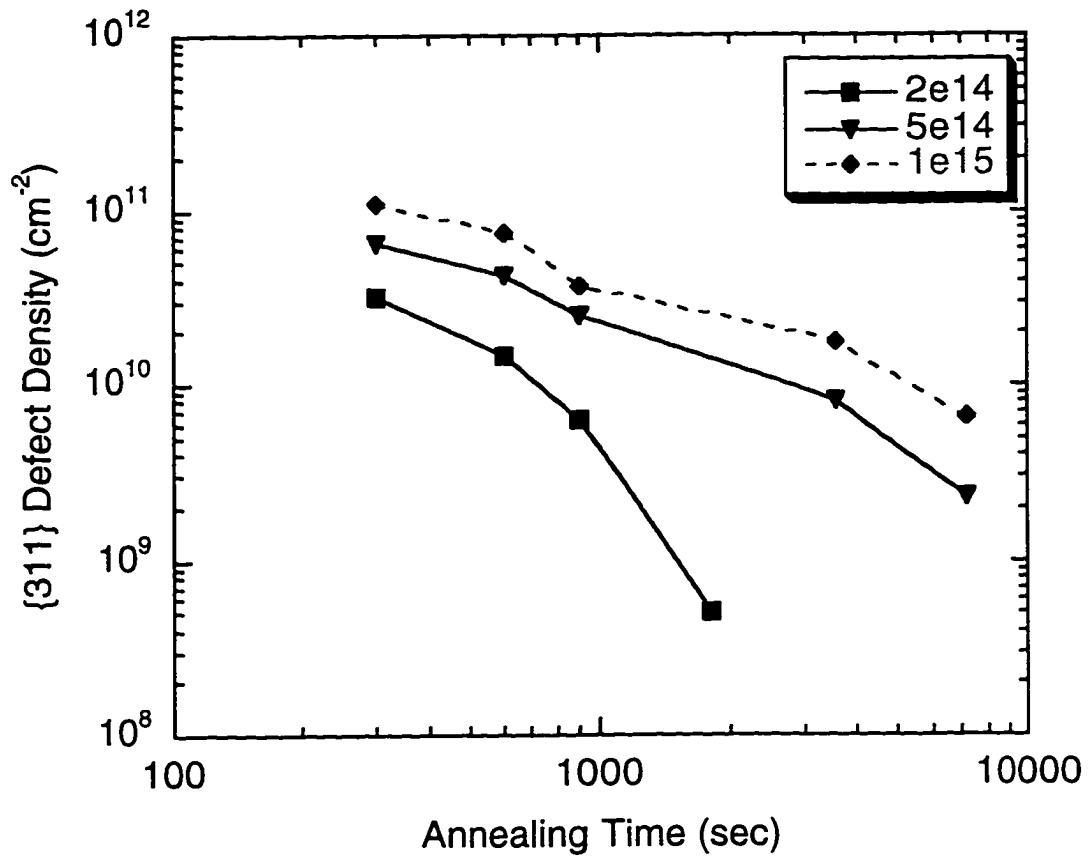


Figure 5.5. {311} defect density as a function of annealing time in 20keV B<sup>+</sup> implanted Si for different doses.

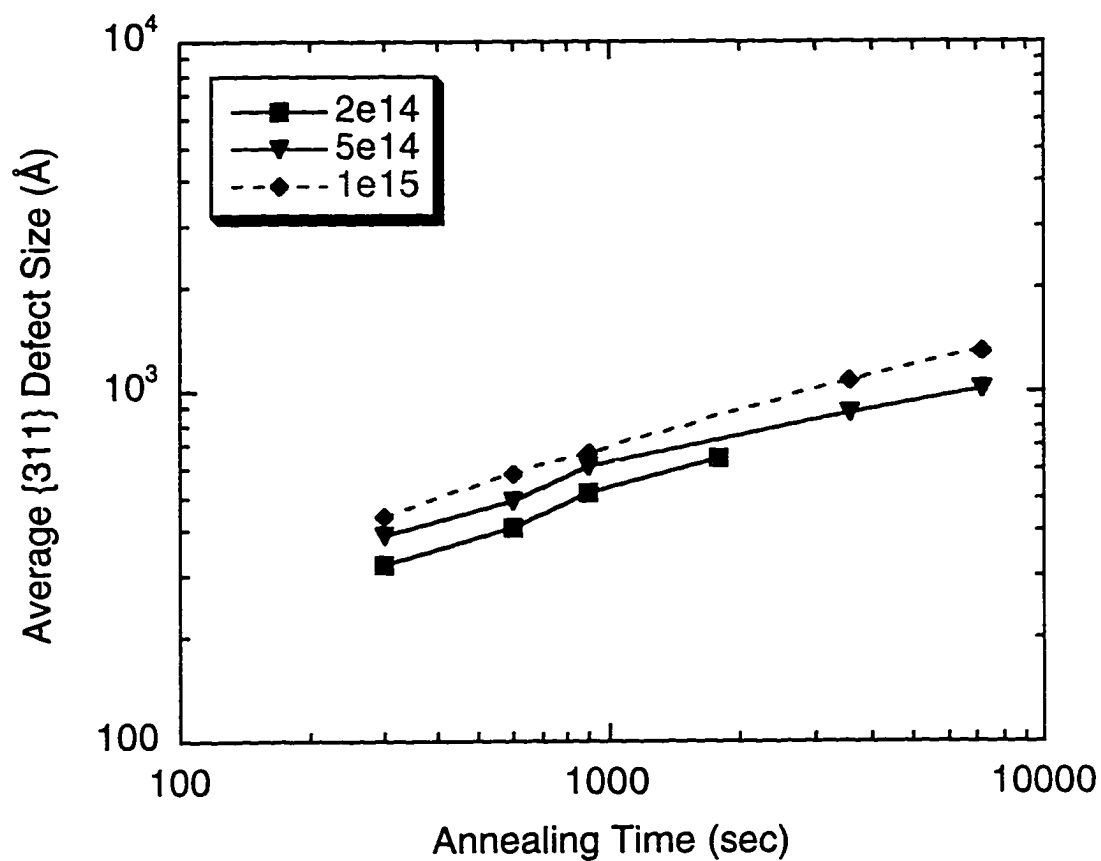
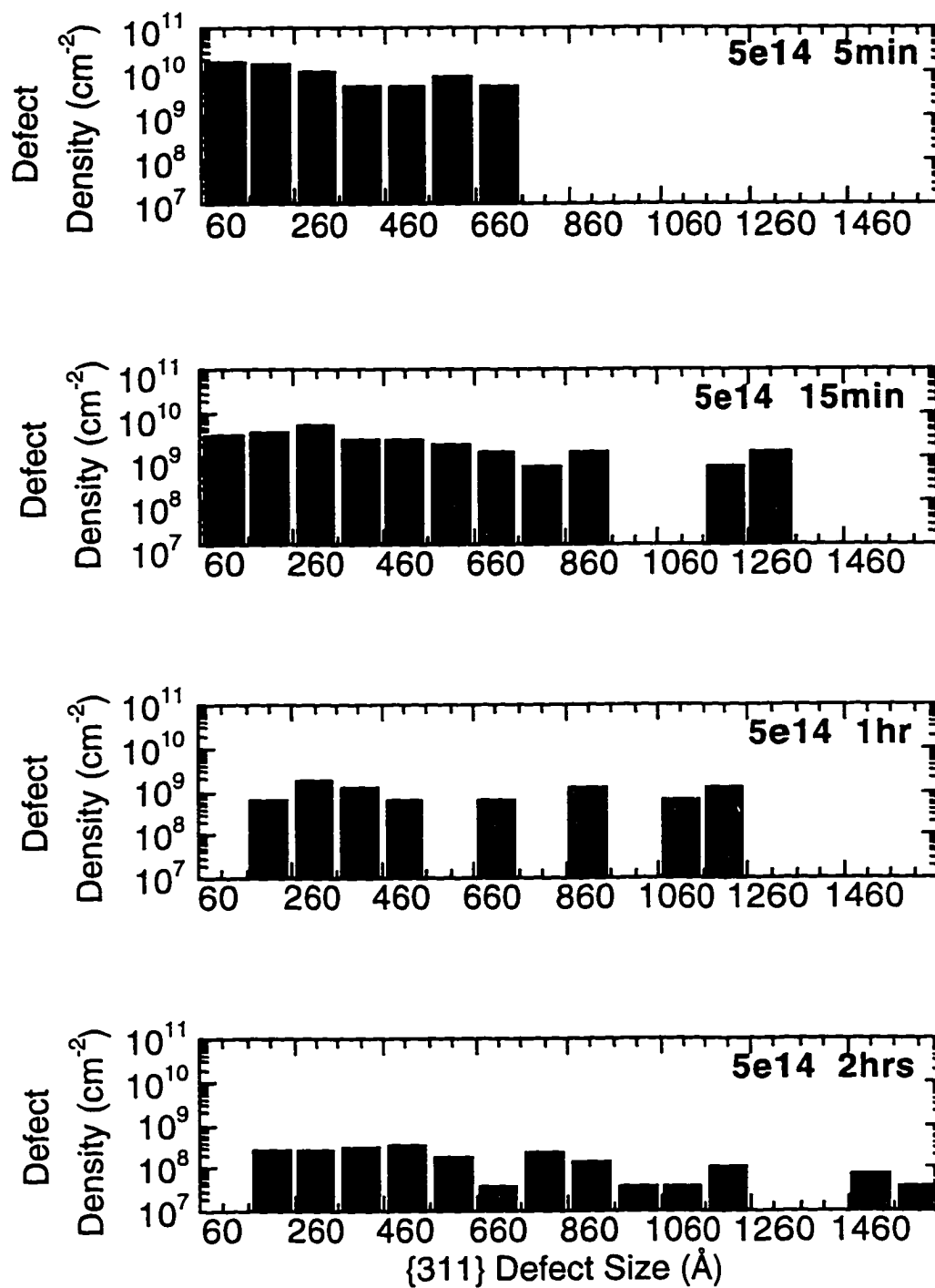
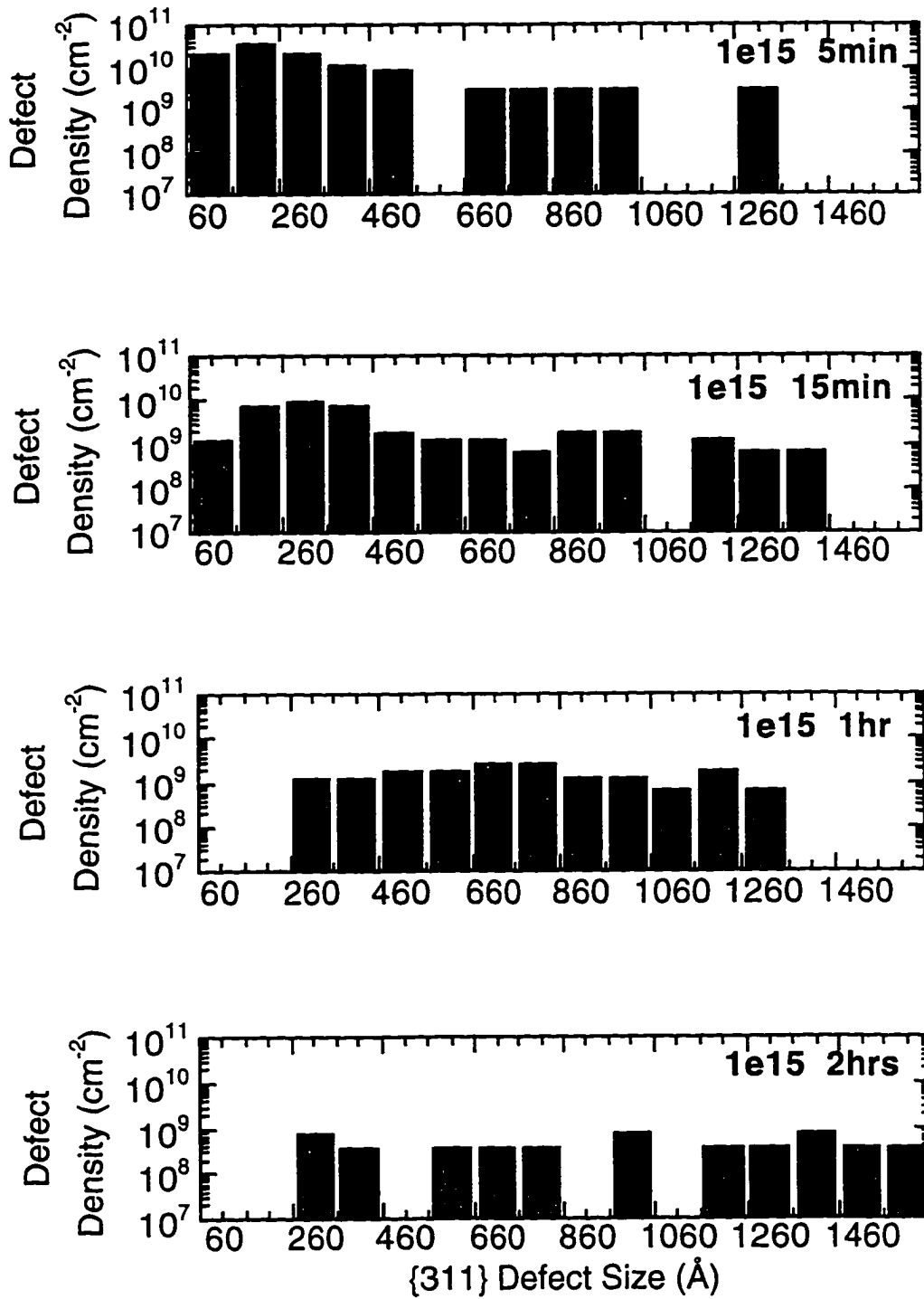


Figure 5.6. Average {311} defect size as a function of annealing time in 20keV B<sup>+</sup> implanted Si for different doses.



(a)

Figure 5.7. {311} defect size distribution for (a)  $5 \times 10^{14} \text{ cm}^{-2}$  and (b)  $1 \times 10^{15} \text{ cm}^{-2}$  implants, annealed at  $750^\circ\text{C}$ .



(b)

Figure 5.7. (Continued)

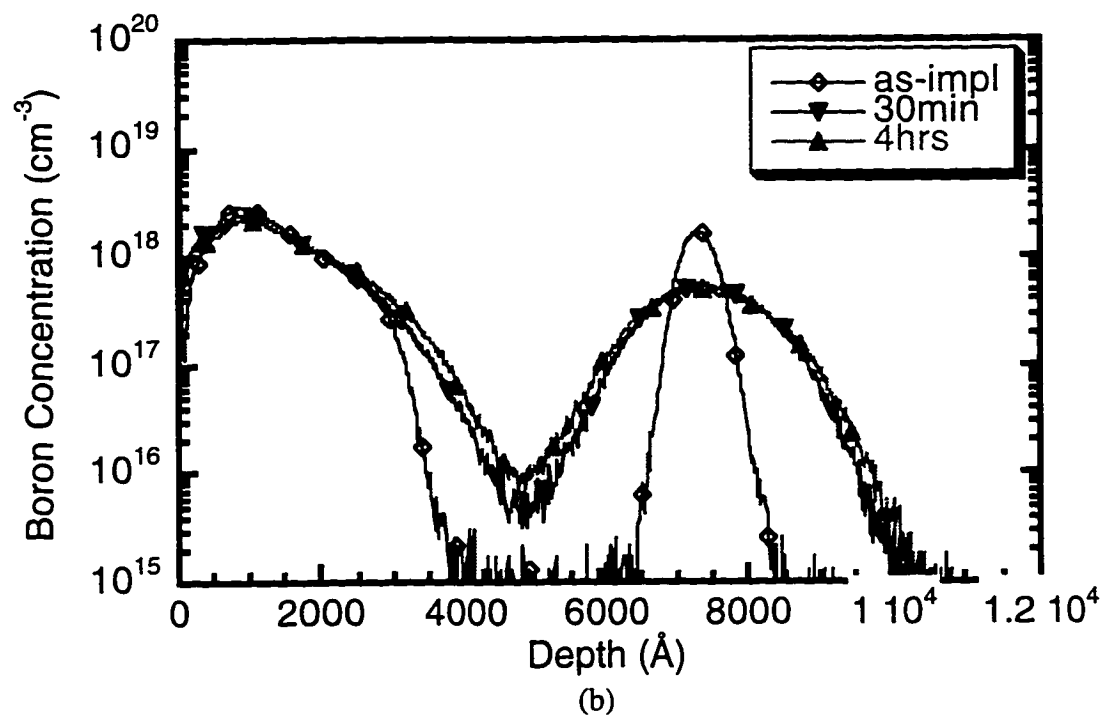
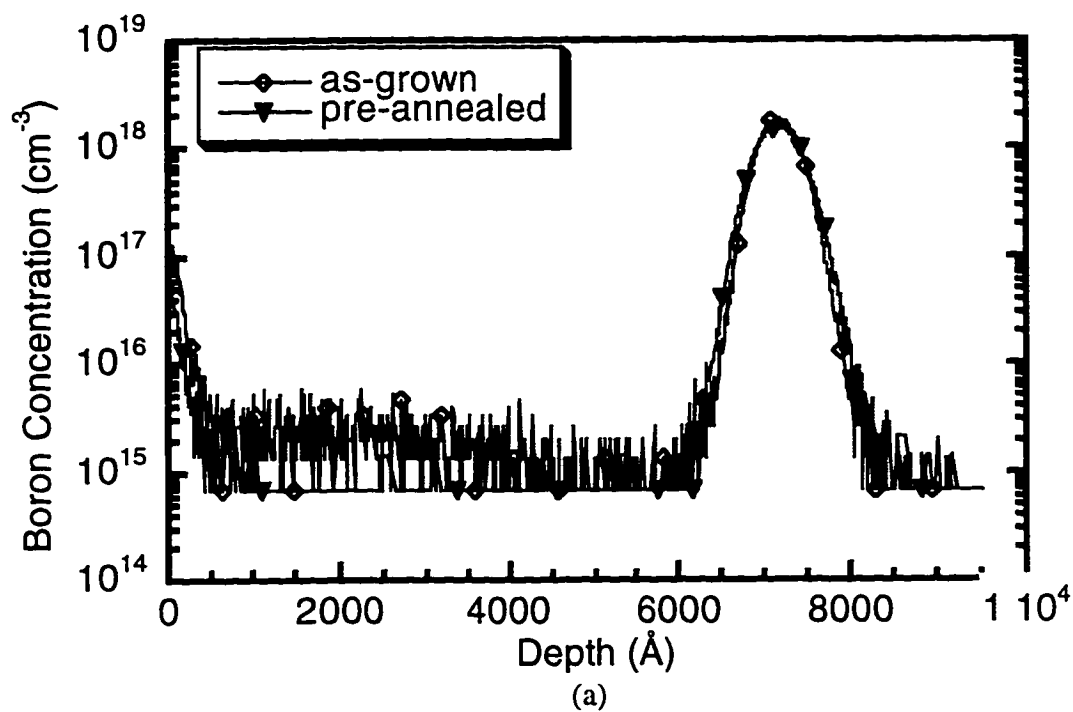


Figure 5.8. SIMS profiles of boron in 20keV  $\text{B}^+$  implanted Si superlattice at a dose of (b)  $5 \times 10^{13} \text{cm}^{-2}$ , (c)  $2 \times 10^{14} \text{cm}^{-2}$ , (d)  $1 \times 10^{15} \text{cm}^{-2}$ . (a) shows the control sample profiles.

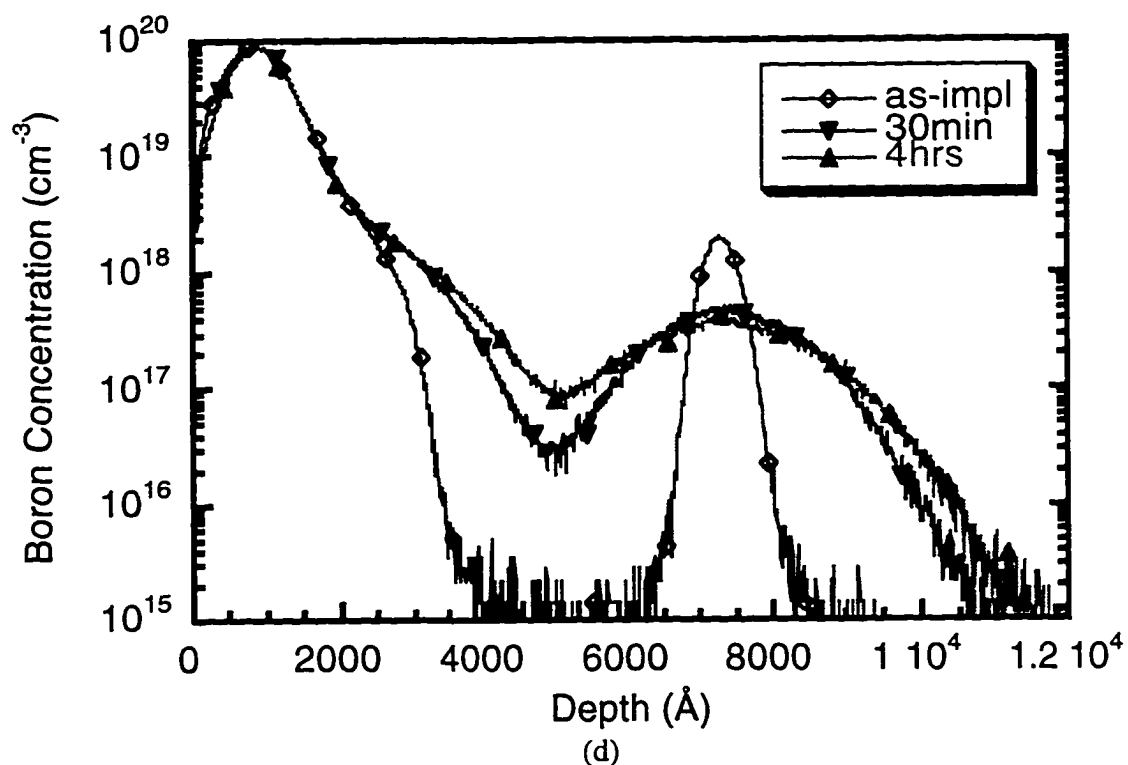
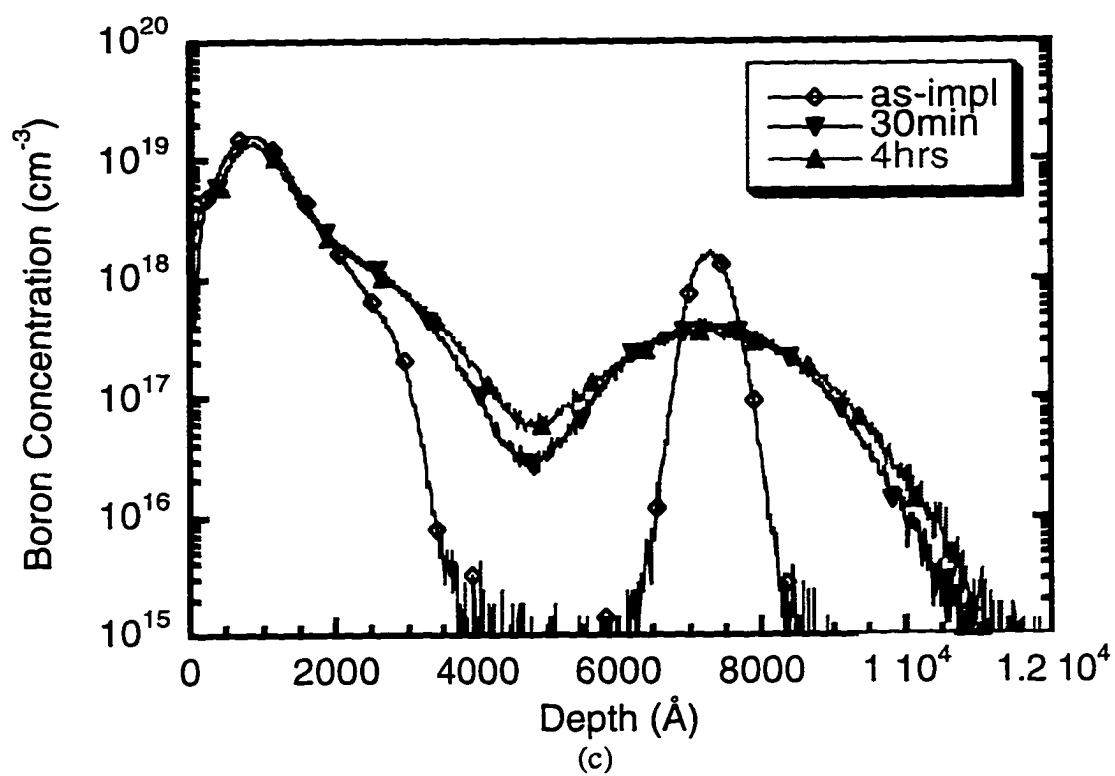


Figure 5.8. (Continued)

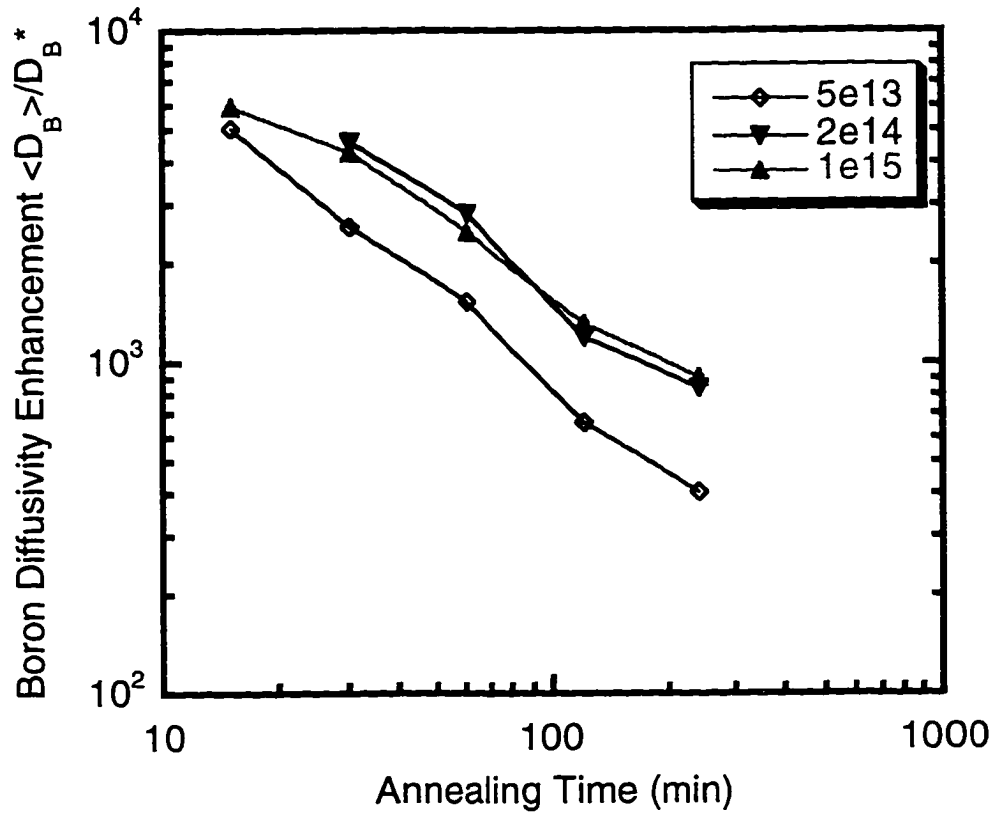


Figure 5.9. Time-averaged boron diffusivity enhancement  $\langle D_B \rangle / D_B^*$  as a function of annealing time for different implant doses.



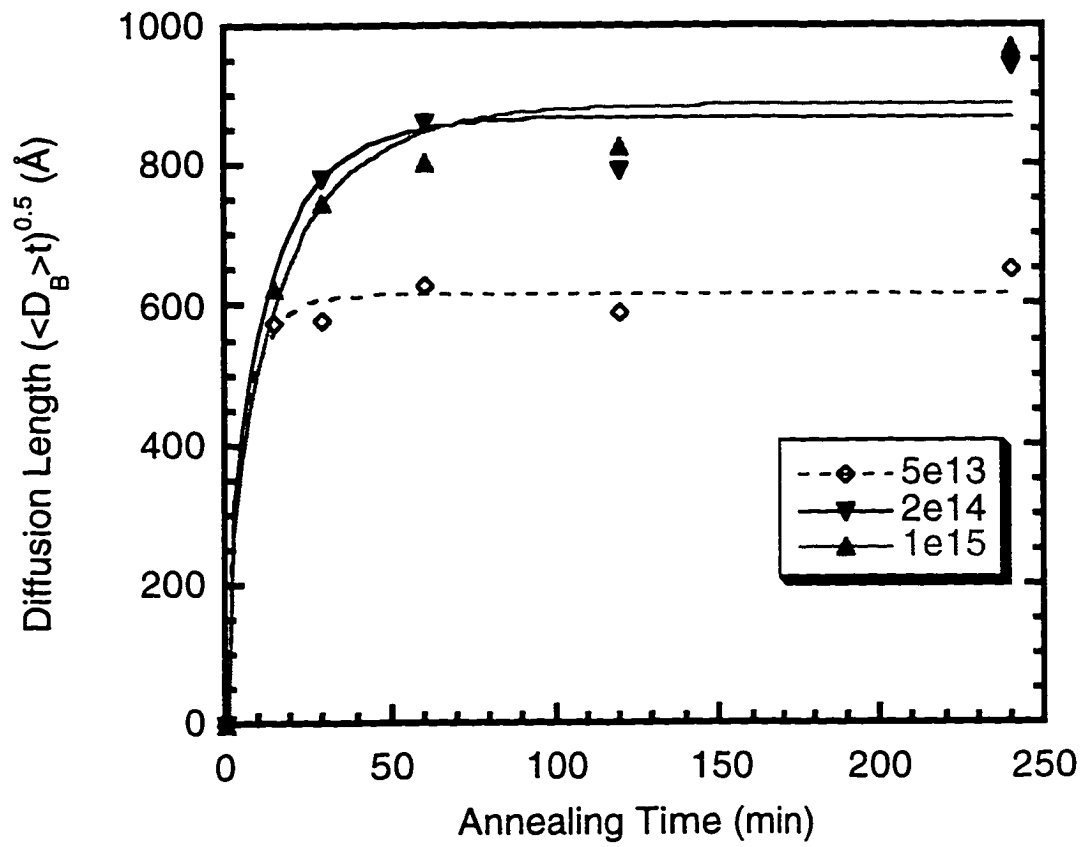


Figure 5.10. Boron diffusion length vs. annealing time for different implant doses.

## CHAPTER 6 SUMMARY AND FUTURE WORK

### 6.1 Summary

Transient enhanced diffusion presents a major obstacle for the optimization of shallow junction devices. The excess interstitials introduced by an ion implantation process are the driving force for TED. In order to gain better control of dopant diffusion, it is crucial to understand the behavior of ion implantation induced defects and their correlation with dopant diffusion. This work represents an effort towards meeting this goal. A brief summary of this work is given below.

A low energy B implant matrix has been employed in this study. The formation threshold doses of both {311} rod-like defects and [110] sub-amorphization loops were examined using TEM. Both threshold doses increase with decreasing implant energy and the one for {311} defect formation is lower than that for loop formation. Displaced atom density calculated from TRIM seems to be able to predict the formation threshold very well.

One particular sample in the matrix was used to study the effect of annealing on {311} defect evolution and TED behavior. {311} defects dissolve rapidly during annealing.

The interstitials trapped in {311} defects decay exponentially with annealing time with a characteristic time constant smaller at higher temperature. The activation energy of {311} defect dissolution process was determined to be 3.8eV. The defect density and the average defect size were also quantified. The size distribution of {311} defects demonstrates an Ostwald ripening process along with a defect dissolution process. Boron diffusion was measured through SIMS and the diffusivity enhancement  $\langle D_B \rangle / D_B^*$  was extracted from FLOOPS simulations.  $\langle D_B \rangle / D_B^*$  decreases with increasing annealing time. The diffusion length increases initially during the annealing and then reaches a saturation point when it starts to plateau out. The time constant decreases dramatically when annealing temperature increases. The activation energy for the TED saturation process was determined to be 1.6eV. Both mobile boron interstitial pair complexes and {311} defects are believed to be the source of interstitials driving TED. The static implant profile peak is believed to be due to the  $B_S$ - $B_I$ -I clustering effect. The breaking point between the mobile tail region and the immobile peak region  $C_{enh}$  moves to higher concentration when temperature increases due to a decreasing interstitial supersaturation level and thus less cluster formation.

The influence of implant energy on {311} defect evolution was investigated by studying samples implanted to a single dose ( $2 \times 10^{14} \text{ cm}^{-2}$ ) at various energies (5~40 keV). {311} defects were observed at energies greater than 5 keV.

The lack of {311} defects in the 5 keV implant might be due to a combination of factors including surface recombination effect, large density of boron interstitial clusters and less implant damage and high I-V recombination. The time constant for the {311} dissolution process is larger for higher energy. Boron  $\delta$ -doping superlattices were used to monitor the diffusion behavior for each implant energy.  $\langle D_B \rangle / D_B^*$  decays exponentially with depth with a decay length larger at shorter annealing time before equilibrium is reached. TED lasts longer and the amount of TED is larger for  $E > 5$  keV than the 5keV implant.

The influence of implant dose on {311} defect evolution was studied by using samples implanted at the same energy (20keV) to various doses ( $5 \times 10^{13} \sim 1 \times 10^{15} \text{ cm}^{-2}$ ). {311} defects dissolve much slower at higher dose. The ratio of the interstitials trapped in {311} defects and loops to the implant dose stays about the same (12%) after a 5min anneal at 750°C regardless of the dose change. Both defect density and average defect size increase with increasing dose. Wafers with a buried boron  $\delta$ -doping layer were implanted to the same doses at the same energy to study the diffusion behavior. The amount of diffusion increases with increasing dose before dislocation loops are formed. Further increase in the dose showed no additional increase in TED presumably due to the trap of interstitials by the loops or the saturation of dopant atoms paired with interstitials.

This work supports the following models for {311} defect evolution and for interstitial storage and release during annealing in B<sup>+</sup> implanted silicon.

Rafferty et al.<sup>134</sup> proposed the following theory to explain the {311} defect formation and dissolution. The model can be represented by

$$\frac{\partial C}{\partial t} = 4\pi\alpha a D_I I(x,t) C(x,t) - C \frac{D_I}{a^2} \exp\left(-\frac{E_b}{kT}\right) \quad (6.1)$$

where  $\alpha$  is the capture radius of an interstitial by a {311} defect expressed in units of the average interatomic spacing  $a$ .  $D_I = D_0 \exp(-E_m/kT)$  is the interstitial diffusivity.  $I(x,t)$  is the concentration of free interstitials and  $C(x,t)$  is the concentration of interstitials trapped in {311} defects. The first term on the right side of eq.(6.1) is the {311} defect formation term. A defect grows whenever diffusing interstitials are trapped by it. The second term is the dissolution term. An interstitial in a {311} defect may escape at a rate given by the interstitial hopping frequency and the binding energy to the defect. At steady state, the first term is balanced by the second. The interstitial supersaturation  $I_e/I^*$  is given by

$$\frac{I_e}{I^*} = \frac{1}{4\pi\alpha\Gamma} \exp\left(-\frac{E_b - E_f}{kT}\right) \quad (6.2)$$

where  $\Gamma$  is a dimensionless prefactor that arises from the entropy of formation of an interstitial and  $E_f$  is the formation energy of an interstitial. The time to dissolve the {311} defects is given by

$$\tau = \frac{4\pi\alpha R_p Q}{D_0 N_s} \exp\left(\frac{E_m + E_b}{kT}\right) \quad (6.3)$$

where  $R_p$  is the projected range,  $Q$  is the implant dose,  $N_s = a^{-3}$  is the number of lattice sites and  $E_m$  is the migration energy of an interstitial. This model predicts that the dissolution time of {311} defects is proportional to the projected range, and therefore to the implant energy (see Fig.2.4), and is proportional to the same degree to the implant dose. A strong temperature dependence is shown by the exponential term. This agrees with our results, which show an increase in  $\tau$  with increasing energy and dose and with decreasing temperature. However, we observed that doubling the dose increases  $\tau$  more than doubling the energy. This can not be explained by the current model.

In Chapter 3, we used the variation of the energy of an interstitial trapped in {311} defects to explain the Ostwald ripening process. In fact the experimentally observed Ostwald ripening process is also in agreement with the model discussed above. Since larger {311} defects are more stable than smaller ones,  $E_b$  must be larger for a larger defect. From eq.(6.2) we can see that  $I_e/I^*$  is lower for larger  $E_b$ . This lower interstitial supersaturation is the driving force for the interstitial flow from smaller defects to larger ones, i.e., the Ostwald ripening process.

Recently a homogeneous nucleation mechanism for the {311} defects was proposed by Chao et al.<sup>135</sup>. They claimed that the diffusion enhancement, which is proportional to the

interstitial supersaturation level  $I_e/I^*$  in eq. (6.2), is related to the defect size (due to the fact that larger defects have larger  $E_b$ ), and they observed that various doses and energies all show similar enhancement within  $t \leq 2$  min. It thus appears that the defect size is independent of the implant conditions, only their number being different. This suggests a homogeneous nucleation mechanism, rather than a mechanism which is limited by the number of available nucleation sites. Our results on {311} defect size variation with implant energy and dose can not directly prove this model since we used furnace anneals with thermal budgets large enough to pass the nucleation stage of the {311} defects.

Regarding the interstitial storage and release during annealing, the following model is suggested based on our observations. At very low energies and doses where no {311} defects or dislocation loops are formed, interstitials are stored in the immobile boron clusters if the implant profile peak concentration is above a critical value ( $C_{enh} > n_i$ ), or in the mobile boron interstitial pairs. During annealing, the clustered peak with B concentration greater than  $C_{enh}$  is static and electrically inactive, while the B atoms paired with interstitials show enhanced diffusion in the profile tail region with concentration less than  $C_{enh}$ . Interstitials are released from the B-I pairs once the B atoms return to substitutional sites. The first saturation of TED occurs when the interstitial supersaturation level reaches

equilibrium. When the annealing temperature is high enough and the time is long enough to break up the immobile B clusters (e.g. 800°C >4hrs), more interstitials are released from these clusters and a second burst of TED will be observed. Only this time the breaking point between the mobile and immobile regions moves up from  $C_{enh}$  to  $C_s$ , the solid solubility limit of B in silicon.

When the implant dose and/or energy increase so that {311} defects form during annealing, interstitials are not only trapped in the B-I clusters and mobile B-I pairs as discussed above, but also trapped in {311} defects. {311} defects dissolve rapidly during annealing and emit interstitials. These interstitials together with those emitted by the B-I pairs are available to drive dopant diffusion. Because of the co-existence of the two sources of interstitials, the activation energy of TED saturation process is lower than that in  $Si^+$  implanted samples with only {311} defects and higher than that in low energy low dose  $B^+$  implanted sample without {311} defects but presumably with B-I pairs.

When the implant dose and/or energy increase further, stable dislocation loops form in addition to {311} defects. Unlike the {311} defects, the loops dissolve relatively slow. They may trap a small or a large amount of interstitials, depending on the density of the loops. As a result of the interstitial sink effect the loops present, the total number of interstitials available to drive TED is reduced. When the



annealing temperature is high enough or the time is long enough (e.g.  $800^{\circ}\text{C} > 1 \text{ hr}$ ), the loops start to dissolve, release interstitials and give rise to more diffusion. The dissolution of loops occurs earlier than the de-clustering of the immobile profile peak, but later than the first saturation of TED.

Assuming the presence of immobile B-I clusters and mobile B-I pairs, a summary of different types of defects formed in samples implanted with various energies and doses based on our implant matrix is shown in Fig.6.1. and a schematic of different sources of TED during an annealing sequence is shown in Fig.6.2. Quantification of how the interstitials partition themselves into B-I clusters or B-I pairs will allow us to gain better understanding on dopant diffusion.

## 6.2 Future Work

There is still a significant amount of research to be done in the area of defect and diffusion behavior after ion implantation. The following are some suggestions.

### 1. High annealing temperature regime

An activation energy of 1.6eV for the TED saturation process was obtained through the diffusion study of 20keV  $2 \times 10^{14} \text{cm}^{-2}$  B<sup>+</sup> implanted silicon after furnace anneals at  $650\sim 800^{\circ}\text{C}$  for various times (see Chapter 3). The sample contains {311} defects only. A much higher activation energy of 4.3eV has been reported by Michel for 60keV  $2 \times 10^{14} \text{cm}^{-2}$  B<sup>+</sup>

implant after furnace and rapid thermal anneals at 800~1000°C. His sample, according to our defect formation threshold study, should contain both {311} defects and dislocation loops. It would be interesting to anneal our samples in that high temperature regime to investigate possible difference in diffusion mechanism and the effect of loops on TED.

## 2. Electrical activity measurements

Through spreading resistance profiling (SRP) measurements we can determine the electrically active portion of the implanted boron atoms. This can help us gain information regarding the clustering/de-clustering motion of the boron peak region and its effect on TED in the tail region.

## 3. Effect of implant species, dose rate and implant temperature

Our group's preliminary results show that P implants have higher formation threshold than Si and B implant. Implant dose rate, if changing within one order of magnitude, does not affect TED behavior in crystalline silicon, however, higher dose rate does result in faster {311} defect dissolution under the same annealing conditions. Implantation temperature, if changing between 5~40°C, does not affect TED behavior either. Further studies would be necessary to investigate the effects of these variables on defect evolution and dopant diffusion.

## 4. Effect of background doping

Boron doped silicon has been found to show less {311} defects when the doping level is increased. The doping of other species, such as P, may also influence the defect behavior.

#### 5. Surface recombination effect

We have discussed that the effect of surface recombination coupled with other factors which altogether result in the lack of {311} defects in the 5keV implant and a smaller enhanced diffusion than higher energy implants. It would be interesting if the surface recombination effect can be quantified and sorted out from the others.

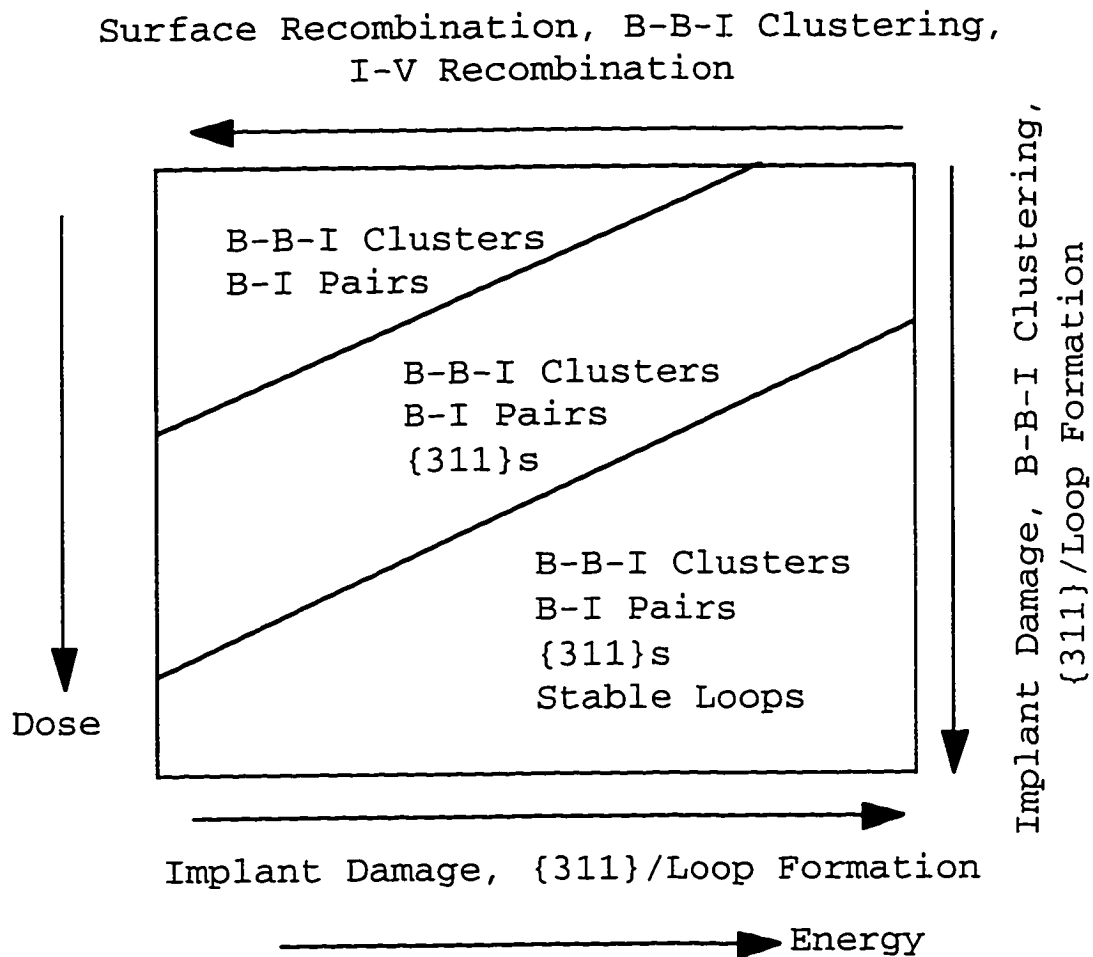


Figure 6.1. A summary of different types of defects that presumably exist in  $B^+$  implanted Si, effects of implant energies and doses.

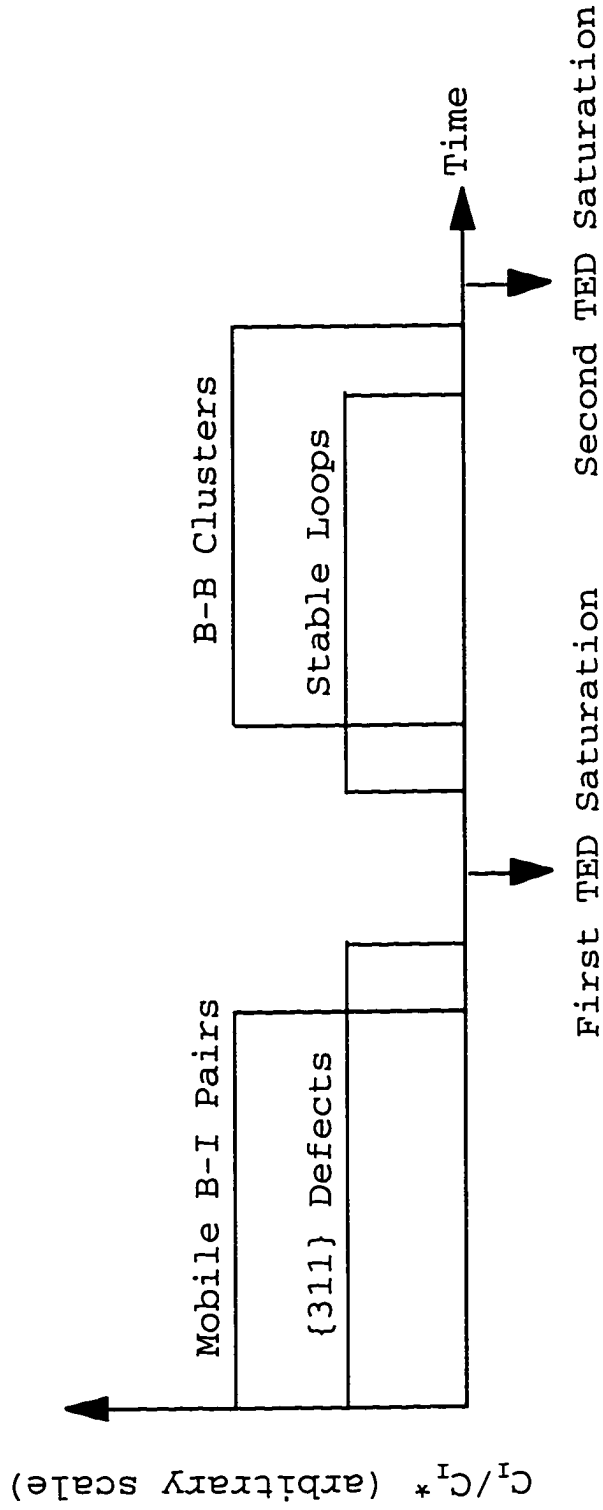


Figure 6.2. A schematic of different sources of interstitials for TED that presumably exist in  $B^+$  implanted Si.

# LIST OF REFERENCES

- 1 C. M. Osburn, J. Electron. Mater. **19**, 67 (1980).
- 2 H. Jiang, C. M. Osburn, P. Smith, Z.-G. Xiao, D. Griffis, G. McGuire, and G. A. Rozgonyi, J. Electrochem. Soc. **139**, 196 (1992).
- 3 S. N. Hong, G. A. Ruggles, J. J. Wortman, and M. C. Ozturk, IEEE Trans. Electron Devices **ED-38**, 476 (1991).
- 4 R. H. Dennard, F. H. Gaensslen, N. H. Yu, V. L. Rideout, E. Bassous, and A. R. LeBlanc, IEEE J. Solid-State Circuits **SC-9**, 256 (1974).
- 5 J. R. Brews, W. Fichtner, E. H. Nicollian, and S. M. Sze, IEEE Electron Device Lett. **EDL-1**, 2 (1980).
- 6 S. N. Hong, G. A. Ruggles, J. J. Paulos, J. J. Wortman, and M. C. Ozturk, Appl. Phys. Lett. **53**, 1741 (1988).
- 7 E. Ling, P. D. Maguire, H. S. Gamble, and B. M. Armstrong, IEEE Electron Device Lett. **EDL-8**, 96 (1987).
- 8 K. T. Kim and C. K. Kim, IEEE Electron Device Lett. **EDL-8**, 569 (1987).
- 9 H. J. Bohm, H. Wendt, H. Oppolzer, K. Masseli, and R. Kassing, J. Appl. Phys. **62**, 2784 (1987).
- 10 M. Horiuchi and K. Yamaguchi, IEEE Trans. Electron Devices **ED-33**, 260 (1986).
- 11 P. G. Carey, T. W. Sigmon, R. L. Press, and T. S. Fahlen, IEEE Electron Device Lett. **EDL-6**, 291 (1985).
- 12 Y. El-Mansy, IEEE Trans. Electron Devices **ED-29**, 567 (1982).
- 13 Y. Kim, H. Z. Massoud, and R. B. Fair, Appl. Phys. Lett. **53**, 2197 (1988).
- 14 S. Guimaraes, E. Landi, and S. Solmi, Phys. Stat. Sol. (a) **95**, 589 (1986).

- 15 F. F. Morehead and R. T. Hodgson, Mat. Res. Soc. Symp. Proc. **35**, 341 (1985).
- 16 J. F. Marchiando and J. Albers, J. Appl. Phys. **61**, 1380 (1987).
- 17 T. O. Sedgwick, A. E. Michel, V. R. Deline, S. A. Cohen, and J. B. Lasky, J. Appl. Phys. **63**, 1452 (1988).
- 18 S. Solmi, R. Angelucci, F. Cembali, M. Servidori, and M. Anderle, Appl. Phys. Lett. **51**, 331 (1987).
- 19 S. Nishikawa, A. Tanaka, and T. Yamaji, Appl. Phys. Lett. **60**, 2270 (1992).
- 20 Q. Guo, X. Bao, J. Hong, Y. Yan, and D. Feng, Appl. Phys. Lett. **54**, 1433 (1989).
- 21 C. S. Rafferty, H.-H. Vuong, S. A. Eshragi, M. D. Giles, M. R. Pinto, and S. J. Hillenius, IEDM Technical Digest, 311 (1993).
- 22 M. C. Ozturk and J. J. Wortman, Appl. Phys. Lett. **52**, 963 (1988).
- 23 M. Kase, M. Kimura, H. Mori, and T. Ogawa, Appl. Phys. Lett. **56**, 1231 (1990).
- 24 A. Bousetta, J. A. van den Berg, D. G. Amour, and P. C. Zalm, Appl. Phys. Lett. **58**, 1626 (1991).
- 25 O. M. Holland and J. Narayan, Nucl. Inst. Meth. B **40/41**, 537 (1989).
- 26 R. G. Wilson, J. Appl. Phys. **54**, 6879 (1983).
- 27 E. Ganin and A. Marwick, Mat. Res. Soc. **147**, 13 (1989).
- 28 A. C. Ajmera and G. A. Rozgonyi, Appl. Phys. Lett. **49**, 1269 (1986).
- 29 L. Laanab, C. Bergaud, C. Bonafos, A. Martinez, and A. Claverie, Nucl. Inst. Meth. B **96**, 236 (1995).
- 30 R. G. Taylor, C. Andre, T. Salama, and P. Ratnam, IEDM Tech. Dig., p.644 (1988).
- 31 D. C. Chen, T. R. Cass, J. E. Turner, P. P. Merchant, and K. Y. Chiu, IEEE Trans. Electron Devices **ED-33**, 1463 (1986).

- 32 E. K. Broadbent, R. F. Inrani, A. E. Morgan, and P. Maillot, IEEE Trans. Electron Devices ED-36, 2440 (1989).
- 33 J. Lin, S. Barnerjee, J. Lee, and C. Teng, IEEE Electron Device EDL-11, 191 (1990).
- 34 V. Ilderem and R. Reif, J. Electrochem. Soc. 136, 2989 (1989).
- 35 R. Liu, D. S. Williams, and W. T. Lynch, J. Appl. Phys. 63, 1990 (1988).
- 36 V. Probst, H. Schaber, A. Mitwalski, H. Kabza, L. Van den hove, and K. Maex, J. Appl. Phys. 70, 708 (1991).
- 37 M. H. Juang and H. C. Cheng, J. Appl. Phys. 71, 1271 (1992).
- 38 S. B. Herner, K. S. Jones, H.-J. Gossman, R. T. Tung, J. M. Poate, and H. S. Luftman, in The effect of TiSi<sub>2</sub> film thickness and growth on the point defect perturbation in Si, 1996 (Electrochemical Society), p.337-347.
- 39 D.-S. Wen, P. Smith, C. M. Osburn, and G. A. Rozgonyi, J. Electrochem. Soc. 136, 466 (1989).
- 40 K. H. Weiner, P. G. Garey, A. M. McCarthy, and T. W. Sigmon, IEEE Electron Device Lett. EDL-13, 369 (1991).
- 41 J. F. Gibbons, Proc. of the IEEE 60, 1062-1096 (1972).
- 42 K. S. Jones, S. Prussin, and E. R. Weber, Appl. Phys. A 45, 1 (1988).
- 43 K. S. Jones and J. Gyulai, Ion Implantation Science and Technology (Ion Implantation Technology Co., Yorktown, NY, 1996).
- 44 J. Liu, M. E. Law, and K. S. Jones, Solid-State Electronics 38, 1305 (1995).
- 45 D. Venables and K. S. Jones, Nucl. Inst. Meth. Phys. Res. B59/60, 1019 (1991).
- 46 L. Laanab, C. Bergaud, M. M. Faye, J. Faure, A. Martinez, and A. Claverie, Mat. Res. Soc. Symp. Proc. 279, 381 (1993).
- 47 O. Dokumaci, P. Rousseau, S. Luning, V. Krishnamoorthy, K. S. Jones, and M. E. Law, J. Appl. Phys. 78, 828 (1995).



- 48 K. Krishnamoorthy, D. Venables, and K. S. Jones, in Proc. Ion Implantation Technology, Austin, TX, 1996.
- 49 R. G. Elliman, J. S. Williams, D. M. Maher, and W. L. Brown, Mat. Res. Soc. Symp. Proc. 51 (1986).
- 50 F. F. Komarov, A. P. Novikov, T. T. Samoilyuk, V. S. Solov'yev, and S. U. Shiryaev, Rad. Eff. 90, 307 (1985).
- 51 J. Linnros and G. Holmes, Mat. Res. Soc. Symp. Proc. 51 (1986).
- 52 I. G. Salisbury and M. H. Loretto, Phil. Mag. 39, 317 (1979).
- 53 I. G. Salisbury and M. H. Loretto, Rad. Eff. 59, 59 (1981).
- 54 Y. Tsubokawa, M. Kuwabara, H. Endoh, and H. Hashimoto, J. Electron Microscopy 35 Suppl, 953 (1986).
- 55 M. Pasemann, D. Hoehl, A. L. Aseev, and O. P. Pchelyakov, Phys. Status Solidi a80, 135 (1983).
- 56 T. Y. Tan, Phil. Mag. 44, 101 (1981).
- 57 P. K. Madden and S. M. Davidson, Radiation Effects 14, 271 (1972).
- 58 K. Seshan and J. Washburn, Phys. Stat. Sol. 26, 345-352 (1974).
- 59 C. A. Ferreira Lima and A. Howie, Phil. Mag. 34, 1057 (1976).
- 60 S. Takeda, Jpn. J. Appl. Phys. 30, L639 (1991).
- 61 K. S. Jones, J. Liu, L. Zhang, V. Krishnamoorthy, and R. T. DeHoff, Nucl. Inst. Meth. B 106, 227 (1995).
- 62 J. A. Lambert and P. S. Dodson, Phil. Mag. 44, 1043 (1981).
- 63 W. Wu and J. Washburn, J. Appl. Phys. 48, 3742 (1977).
- 64 J. J. Comer, Radiation Effects 36, 57 (1978).
- 65 H. Foell, T. Y. Tan, and W. Krakow, Mat. Res. Soc. Symp. Proc. 2, 173 (1981).

- 66 F. Cembali, L. Dori, R. Galloni, M. Servidori, and F. Zignani, Radiation Effects 36, 111 (1978).
- 67 K. Seshan and J. Washburn, Rad. Eff. 26, 31 (1975).
- 68 K. Seshan and J. Washburn, Radiation Effects 14, 267 (1972).
- 69 I. W. Wu and L. J. Chen, J. Appl. Phys. 58, 3032 (1985).
- 70 E. Nes and J. Washburn, J. Appl. Phys. 42, 3559 (1971).
- 71 J. Narayan and J. Fletcher, MRS Symp. Proc. 2, 191 (1981).
- 72 M. D. Matthews and S. J. Ashby, Phil. Mag. 27, 1313 (1973).
- 73 S. M. Davidson and G. R. Booker, Rad. Effects 6, 33 (1970).
- 74 M. Tamura, Appl. Phys. Lett. 23, 651 (1973).
- 75 L. T. Chadderton and F. H. Eisen, Radiation Effects 7, 129 (1971).
- 76 A. Parisini and A. Bourret, Phil. Mag. A 67, 605 (1992).
- 77 T. Y. Tan and U. Gösele, J. Appl. Phys. 37, 1 (1985).
- 78 S. Wolf and R. N. Tauber, Silicon Processing for the VLSI Era, Vol. 1 (Proc. Tech. Latt. Press, Sunset Beach, FL, 1983).
- 79 W. Frank, U. Gosele, H. Maher, and A. Seeger, Diffusion in Si and Ge (Academic Press, Orlando, FL, 1983).
- 80 S. K. Ghandhi, VLSI Fabrication Principles, John Wiley & Sons, Inc. (1982).
- 81 C. M. Hsieh and D. M. Maher, J. Appl. Phys. 44, 1302 (1973).
- 82 S. M. Hu, J. Appl. Phys. 45, 1567 (1974).
- 83 T. Y. Tan and U. Gosele, Appl. Phys. Lett. 39, 86 (1981).
- 84 D. A. Antoniadis and I. Moskowitz, J. Appl. Phys. 53, 6788 (1982).
- 85 P. A. Packan and J. D. Plummer, J. Appl. Phys. 68, 4327 (1990).

- 86 D. J. Roth, Y. S. Huang, J. D. Plummer, and R. W. Dutton, Appl. Phys. Lett. **62**, 2498 (1993).
- 87 S. Mizuo, T. Kusaka, A. Shintani, M. Nanba, and H. Higuchi, J. Appl. Phys. **54**, 3860 (1983).
- 88 S. Mizuo and H. Higuchi, Japan. J. Appl. Phys. **21**, 281 (1982).
- 89 P. Fahey, R. W. Dutton, and M. Moslehi, Appl. Phys. Lett. **43**, 683 (1983).
- 90 P. Fahey, G. Barbuscia, M. Moslehi, and R. W. Dutton, Appl. Phys. Lett. **46**, 784 (1985).
- 91 M. Witter and K. N. Tu, Phys. Rev. B **29**, 2010 (1984).
- 92 P. Fahey and M. Wittmer, Mat. Res. Soc. Symp. Proc. **163**, 529 (1990).
- 93 D. S. Wen, P. L. Smith, C. M. Osburn, and G. A. Rozgonyi, Appl. Phys. Lett. **51**, 1182 (1987).
- 94 F. M. d'Heurle and P. Gas, J. Mater. Res. **1**, 205 (1986).
- 95 C. M. Osburn, J. Electrochem. Soc. **19**, 67 (1990).
- 96 H. Jiang, C. M. Osburn, P. Smith, Z.-G. Xiao, G. McGuire, and G. A. Rozgonyi, J. Electrochem. Soc. **139**, 211 (1992).
- 97 N. R. Wu, D. K. Sadana, and J. Washburn, Appl. Phys. Lett. **44**, 782 (1984).
- 98 P. A. Stolk, H. J. Gossmann, D. J. Eaglesham, D. C. Jacobson, J. M. Poate, and H. S. Luftman, Appl. Phys. Lett. **66**, 568 (1995).
- 99 R. Angelucci, G. Celotti, D. Nobili, and S. Solmi, J. Electrochem. Soc. **132**, 2726 (1985).
- 100 C. van Opdorp, L. J. van IJzendoorn, C. W. Fredriksz, and D. J. Gravesteijn, J. Appl. Phys. **72**, 4047 (1992).
- 101 R. Angelucci, P. Negrini, and S. Solmi, Appl. Phys. Lett. **49**, 1468 (1986).
- 102 M. D. Giles, Appl. Phys. Lett. **62**, 1940 (1993).
- 103 N. E. B. Covern, G. F. A. van de Walle, P. C. Zalm, and D. W. E. Vandenhoudt, Appl. Phys. Lett. **65**, 2981 (1994).

- 104 G. Hobler and S. Selberherr, IEEE Trans. on Comp. Aid. Des. 7, 174 (1988).
- 105 J. K. Listebarger, K. S. Jones, and J. A. Slinkman, J. Appl. Phys. 73, 4815 (1993).
- 106 S. Prussin, J. Appl. Phys. 43, 2850 (1972).
- 107 C. M. Drum and W. van Gelder, J. Appl. Phys. 43, 4465 (1972).
- 108 O. L. Krivanek and D. M. Maher, Appl. Phys. Lett. 32, 451 (1978).
- 109 H. L. Meng, S. Prussin, M. E. Law, and K. S. Jones, J. Appl. Phys. 73, 955 (1993).
- 110 M. Servidori, Z. Sourek, and S. Solmi, J. Appl. Phys. 62, 1723 (1987).
- 111 H. Chao, P. Griffin, and J. Plummer, Appl. Phys. Lett. 68, 3570 (1996).
- 112 D. J. Eaglesham, P. A. Stolk, H.-J. Gossman, and J. M. Poate, Appl. Phys. Lett. 65, 2305 (1994).
- 113 P. A. Stolk, H.-J. Gossmann, D. J. Eaglesham, D. C. Jacobson, H. S. Luftman, and J. M. Poate, Mat. Res. Soc. Symp. Proc. 354 (1995).
- 114 L. H. Zhang, K. S. Jones, P. H. Chi, and D. S. Simons, Appl. Phys. Lett. 67, 2025 (1995).
- 115 Encyclopedia of Materials Characterization (Butterworth-Heinemann, Stoneham, MA 02180, 1992).
- 116 Y. M. Kim, G. Q. Lo, H. Kinoshita, D. L. Kwong, H. H. Tseng, and R. Hance, J. Electrochem. Soc. 138, 1122 (1991).
- 117 H. Kinoshita, G. Q. Lo, and D. L. Kwong, J. Electrochem. Soc. 140(1), 248 (1993).
- 118 H. U. Jager, J. Appl. Phys. 78, 176 (1995).
- 119 M. Tamura, N. Natsuaki, Y. Wada, and E. Mitani, Nucl. Inst. Meth. B 21, 438 (1987).
- 120 J. F. Gibbons, Proc. IEEE 60, 1062 (1972).

- 121 V. Raineri, R. J. Schreutelkamp, F. W. Saris, R. E. Kaim, and K. T. F. Janssen, NIMPR B59/60, 1056 (1991).
- 122 R. J. Schreutelkamp, J. S. Custer, J. R. Liefiting, W. X. Lu, and F. W. Saris, Mat. Sci. Reports 6, 275 (1991).
- 123 N. E. B. Cowern, A. Cacciato, J. S. Custer, F. W. Saris, and W. Vandervorst, Appl. Phys. Lett. 68, 1150 (1996).
- 124 M. D. Giles, J. Electrochem. Soc. 138, 1160-1165 (1991).
- 125 D. J. Eaglesham, P. A. Stolk, H. J. Gossmann, T. E. Haynes, and J. M. Poate, Nucl. Inst. Meth. B 106, 191 (1995).
- 126 A. E. Michel, W. Rausch, P. A. Ronsheim, and R. H. Kastl, Appl. Phys. Lett. 50, 416 (1987).
- 127 R. B. Fair, J. of Electrochem. Soc. 137, 667 (1990).
- 128 N. E. B. Cowern, K. T. F. Janssen, and H. F. F. Jos, J. Appl. Phys. 68, 6191 (1990).
- 129 R. B. Fair, in Impurity Doping Processes in Silicon, edited by F. F. Y. Wang (North Holland, New York, 1981), p.968, 315.
- 130 P. Packan, Ph.D. Dissertation, Stanford University (1989).
- 131 K. S. Jones, V. Krishnamoorthy, L. H. Zhang, M. Law, D. S. Simons, P. H. Chi, L. Rubin, and R. G. Elliman, Appl. Phys. Lett. 68, 2672 (1996).
- 132 S. Solmi, F. Baruffaldi, and R. Canteri, J. Appl. Phys. 69, 2135 (1991).
- 133 P. B. Griffin, R. F. Lever, P. A. Packan, and J. D. Plummer, Appl. Phys. Lett. 64, 1242 (1994).
- 134 C. S. Rafferty, G. H. Gilmer, M. Jaraiz, D. Eaglesham, and H.-J. Gossmann, Appl. Phys. Lett. 68, 2395 (1996).
- 135 H. S. Chao, C. S. Rafferty, P. B. Griffin, and J. D. Plummer, unpublished paper.

## BIOGRAPHICAL SKETCH

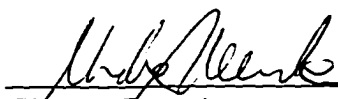
The author was born on September 30, 1968, in Shenyang, China. She entered Wuhan University in China at the age of 17 and obtained a BS in Physics degree with honors in July 1989. She came to the United States in August 1991 as a graduate student in the Physics Department at Tulane University, New Orleans. In July 1992 she transferred to the Department of Materials Science and Engineering at the University of Florida, specializing in electronic materials under the supervision of Dr. Kevin Jones. She received her MS degree in August 1994 and will complete her Ph.D. study in August 1996.

I certify that I have read this study and that in my opinion it conforms to acceptable standards of scholarly presentation and is fully adequate, in scope and quality, as a dissertation for the degree of Doctor of Philosophy.



Kevin Jones, Chair  
Associate Professor of  
Materials Science and  
Engineering

I certify that I have read this study and that in my opinion it conforms to acceptable standards of scholarly presentation and is fully adequate, in scope and quality, as a dissertation for the degree of Doctor of Philosophy.



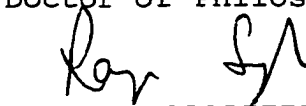
Steve Pearson  
Professor of Materials  
Science and Engineering

I certify that I have read this study and that in my opinion it conforms to acceptable standards of scholarly presentation and is fully adequate, in scope and quality, as a dissertation for the degree of Doctor of Philosophy.



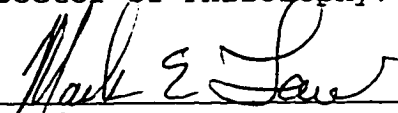
Cammy Abernathy  
Professor of Materials  
Science and Engineering

I certify that I have read this study and that in my opinion it conforms to acceptable standards of scholarly presentation and is fully adequate, in scope and quality, as a dissertation for the degree of Doctor of Philosophy.




Rajiv Singh  
Associate Professor of  
Materials Science and  
Engineering

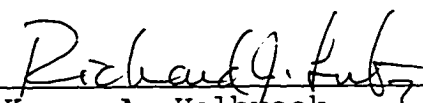
I certify that I have read this study and that in my opinion it conforms to acceptable standards of scholarly presentation and is fully adequate, in scope and quality, as a dissertation for the degree of Doctor of Philosophy.

  
\_\_\_\_\_  
Mark Law  
Associate Professor of  
Electrical Engineering

This dissertation was submitted to the Graduate Faculty of the College of Engineering and to the Graduate School and was accepted as partial fulfillment of the requirements for the degree of Doctor of Philosophy.

December, 1996

  
\_\_\_\_\_  
Winfred M. Phillips  
Dean, College of Engineering

  
\_\_\_\_\_  
Karen A. Holbrook  
Dean, Graduate School